ABSTRACT

THE FEASIBILITY STUDY OF MICROMACHINED DYNAMIC RESONANT BEAM CORIOLIS TRUE MASS FLOW METER

by
Sang Hwui Lee

The technological advances of micro-electro-mechanical systems (MEMS) in the past two decades have been remarkable for innovations in microfluidic systems as well as automotive applications such as pressure sensors and accelerometers. MEMS flow sensing has emerged as a field of interest in microfluidics, with a variety of sensing methods being miniaturized, such as thermal anemometry, ultrasonic sensing and flow measurement based on the Coriolis effect. Coriolis sensing is particularly attractive since, unlike most other methods which provide volumetric flow information, Coriolis sensing is capable of providing a direct, true mass flow measurement. Because of this advantage, Coriolis flow sensing has engendered strong interest in developing miniature device designs, fabrication techniques, and sensitive Coriolis detection methods. Research and development efforts have been undertaken both in academia and industry to make inexpensive, highly sensitive, reliable, and appropriately packaged Coriolis solutions. One research focus has been on detection and read-out methods for Coriolis-induced signals. Piezoresistive, optical and capacitive methods have all been tried. This dissertation introduces the resonant beam as a detecting method for Coriolis mass flow sensing. Because resonant beams measure frequency changes, they can be highly sensitive, much more so than the previously tried methods. Resonant beams have been successfully demonstrated in MEMS pressure sensors and accelerometers. This work extends their application to Coriolis mass flow devices.

THE FEASIBILITY STUDY OF MICROMACHINED DYNAMIC RESONANT BEAM CORIOLIS TRUE MASS FLOW METER

by
Sang Hwui Lee

A Dissertation
Submitted to the Faculty of
New Jersey Institute of Technology
In Partial Fulfillment of Requirements for the Degree of
Doctor of Philosophy in Materials Science and Engineering

Interdisciplines Program in Materials Science and Engineering

January 2005

APPROVAL PAGE

THE FEASIBILITY STUDY OF MICROMACHINED DYNAMIC RESONANT BEAM CORIOLIS TRUE MASS FLOW METER

Sang Hwui Lee

Dr. Ken K. Chin, Dissertation Advisor — Date
Professor of Physics, NJIT
Director of Materials Science and Engineering M.S./ Ph.D Program, NJIT

Dr. Boris Khusid, Committee Member — Date
Associate Professor of Mechanical Engineering, NJIT

Dr. William Carr, Committee Member — Date
Professor of Electrical and Computer Engineering, NJIT
Professor of Physics, NJIT

Dr. Zhixiong Xiao, Committee Member — Date
Assistant Research Professor of Physics, NJIT

Dr. Baoqing Li, Committee Member — Date
Research Associate of Physics, NJIT

BIOGRAPHICAL SKETCH

Author: Sang Hwui Lee

Degree: Doctor of Philosophy

Date: January, 2005

Undergraduate and Graduate Education:

- Doctor of Philosophy in Materials Science and Engineering
  New Jersey Institute of Technology, Newark, New Jersey, 2004

- Bachelor of Science in Electronic Materials Engineering,
  Gyeong Sang National University, Chinju, South Korea, 1995

Major: Materials Science and Engineering

Presentations and Publications:

Sang Hwui Lee, Zhixiong Xiao, Xiaodong Wang, Ken K. Chin and K.R. Farmer, "The pseudo-dynamic resonant beam method for micromachined Coriolis true mass flow meter", to be submitted to Journal of Micromechanics and Microengineering.

Sang Hwui Lee, Xiaodong Wang, Zhixiong Xiao, Woochoel Shin, Ken K. Chin and K. R. Farmer, "Simulation and modeling of a bridge-type resonant beam for Coriolis true mass flow sensor", Technology proceedings of 2004 NSTI nanotechnology conference and trade show, vol. 2, pp. 351-354.

Yan Sun, ZhiXiong Xiao, Xiaodong Wang, Sang Hwui Lee, Ken Chin and K.R. Farmer, "Resonant frequency shift of torsion actuators due to electrostatic force," submitted to Journal of Micromechanics and Microengineering.

Xiaodong Wang, Baoqing Li, Zhixion Xiao, Sang Hwui Lee, Harry T. Romman, Onofrio L. Russo, Ken K. Chin, and K. R. Farmer, "An ultrasensitive optical MEMS sensor for partial discharge detection", accepted by Journal of Micromechanics and Microengineering.

Zhixiong Xiao, Yan Sun, Baoqing Li, Sang Hwui Lee, Ken K. Chin and K. R. Farmer, "Resonant frequency shift of torsion actuators due to electrostatic force," Technology proceedings of 2004 NSIT nanotechnology conference and trade show, vol.1, pp. 426-429.

Xiaodong Wang, Baoqing Li, Sang Hwui Lee, Ken K. Chin and K. R. Farmer, "A new method to design pressure sensor diaphragm," Technology proceedings of 2004 NSTI nanotechnology conference and trade show, vol.1, pp. 324-327.

To my beloved family:

Kyeoung Hee Kim, 김경희(金京姬), wife

Joshua Chanhee Lee, 이찬희(李讚熙), son

Myung Nam Lee, 이명남(李明男), father

Hae Suk Kim, 김해숙(金海淑), mother

"A pilgrim's another departure"

"순례자의 또다른 시작"

ACKNOWLEDGMENT

I wish to express my deepest appreciation to my advisor, Professor Ken K. Chin and my former advisor, Professor Kenneth R. Farmer, for their guidance throughout the whole research. Without their support, I could never complete this research topic.

Special thanks to the other members of the committee: Professor Boris Khusid, Professor Bill Carr, Professor Zhixiong Xiao and Dr. Baoqing Li for their careful review of the dissertation and helpful comments.

I would like to thank Professor Dencho Ivanov and Dr. Rajesh Jarwal for their help with the device fabrication in the clean room.

I am very grateful to the staff of the Microelectronics Research Center of NJIT for their administrative work during the research, especially Ms. Lynn Stover and Ms. Sonia Henderson. This work was supported partially by the NJMEMS Initiative by the New Jersey Commission on Science and Technology (NJCST). I would also like to thank Xiaodong Wang, Yuki Imura and other fellow students for their helpful discussions during the study.

Finally, I would like to thank my parents and my family for their continuous support, encouragement and best wishes that were very important while I pursued my doctoral studies. I dedicate this thesis to my wife, Kyeoung Hee Kim.

TABLE OF CONTENTS

TABLE OF CONTENTS
(Continued)

Chapter **Page**

TABLE OF CONTENTS
(Continued)

Chapter **Page**

TABLE OF CONTENTS
(Continued)

LIST OF TABLES
(Continued)

LIST OF TABLES
(Continued)

Table **Page**

LIST OF FIGURES

LIST OF FIGURES
(Continued)

LIST OF FIGURES
(Continued)

Figure **Page**

LIST OF FIGURES
(Continued)

CHAPTER 1

INTRODUCTION

1.1 Motivation

Micro electro mechanical systems (MEMS) technology has been developed extensively over the last 50 years. The field has given rise to numerous important applications such as acceleration [35] and pressure sensing [7]. An emerging innovative use of MEMS technology involves applications in the microfluidic systems. For example, there are numerous potential applications of microfluidic systems in biomedical research [17].

A thermal mass flow sensor [16] measures the amount of fluid flowing through a pipe. The sensor output not only depends on the flow but also on particular gas properties, for instance density, viscosity, thermal conductivity, specific heat and also on ambient temperature. Therefore, thermal mass flow meters require different calibrations depending on the fluid being measured. Coriolis sensing offers the possibility for true mass sensing to be scalable, highly sensitive, without the need for calibration for different fluids, and without interfering with the flow. The performance of Coriolis mass flow sensors is independent of flow profiles and properties such as composition, pressure, temperature, flow density, viscosity and homogeneity. A Coriolis mass flow meter is one of the true mass flow meters using Coriolis Effect [16]. Conventional Coriolis mass flow sensors have been developed for liquid and gas applications but they are expensive and deficient in manipulating microfluids due to their large volumes. Peter Enoksson reported the first micromachined Coriolis mass flow sensor with integrated vibration detection with optical sensing [19]. A goal of micromachined Coriolis mass flow sensor research is

to commercially realize high sensitivity, high stability true mass flow measurement with an on-chip integrated signal conditioning circuit, so that such a meter does not require conversion tables. The measurement is based on mechanical forces. A tube with the flowing fluid is forced to vibrate around a defined axis. Due to Coriolis forces, which are proportional to the mass flow and in a direction perpendicular to both the flow vector and the rotation vector, the vibrations become slightly different. These changes in amplitude or in phase can be measured using sensitive displacement sensors. Ongoing research aims at applications for lower mass flow ranges, such as those required for gas flow measurement in the semiconductor industry [17, 20].

To date, three detection methods have been used to detect the Coriolis induced motion of miniature Coriolis flow sensors: piezoresistive [16, 24], capacitive [33], and optical [19]. This dissertation introduces the resonant beam as a detecting method for Coriolis mass flow sensing. Because resonant beams measure frequency changes, they can be highly sensitive, much more so than the previously tried methods. Resonant beams have been successfully demonstrated in MEMS pressure sensors and accelerometers. This work extends their application to Coriolis mass flow devices.

1.2 Contributions of the Dissertation

This dissertation has two main aims: first, to design a high-sensitivity Coriolis mass flow sensor for gas and liquid mass flow applications; second, to develop the resonant beam detection method in particular. An innovative aspect of this thesis work lies in the novel use of a resonant beam as the vibration pick-up for the Coriolis force, and hence the mass flow rate measurement. Dynamic resonant measurement has been used for other force

sensing applications such as resonant accelerometers and resonant gyroscopes. A comparison of the resonant beam method against piezoresistive, capacitive and optical methods is shown in Table 1.1. Frequency sensing provides high sensitivity at the expense of increased complexity.

Table 1.1 Comparison of Read-out Methods for Coriolis Mass Flow Meter

Method	Piezoresistive[16, 24]	Capacitive[33]	Optical[19]	Resonant beam[31]
Parameter sensed	Displacement	Capacitance	Displacement	Frequency
Sensitivity	Low	High	Medium	High
System size	Small	Medium	Large	Medium
Power consumption	High	Low	Low	Low
Vacuum system	Low	Medium	Low	High
Linearity	Good	Poor	Good	Good
Temperature Dependence	High	Low	Low	Low
Issues	Easy to integrate	Low SNR	Needed big space	Complexity

1.3 Overview of Investigated Coriolis Mass Flow Sensor

Figure 1.1 illustrates the theoretical concept of Coriolis mass flow sensing using the resonant beam mechanism. Fluid flows through a tubular loop structure that is induced to vibrate (first vibration), for example in a torsion mode. The flow induces a second vibration in the loop whose amplitude is a measure of the true mass flow. If the first

vibration is a torsion mode, then the second vibration is an orthogonal bending mode. This second vibration is detected using a resonant beam structure, whose electrostatically driven resonant frequency (third vibration) changes with the amplitude of the second vibration. Thus the resonant beam frequency shift is a linear measure of the true mass flow. Further details of the Coriolis flow sensing principle will be presented in Chapter 3. To summarize the sensor behavior: Mass flow in a vibration tube → the amplitude of Coriolis vibration → the strain change of a resonant beam → the resonant frequency shift. Frequency shift detection has the advantages of ease of digitalization and high sensitivity.

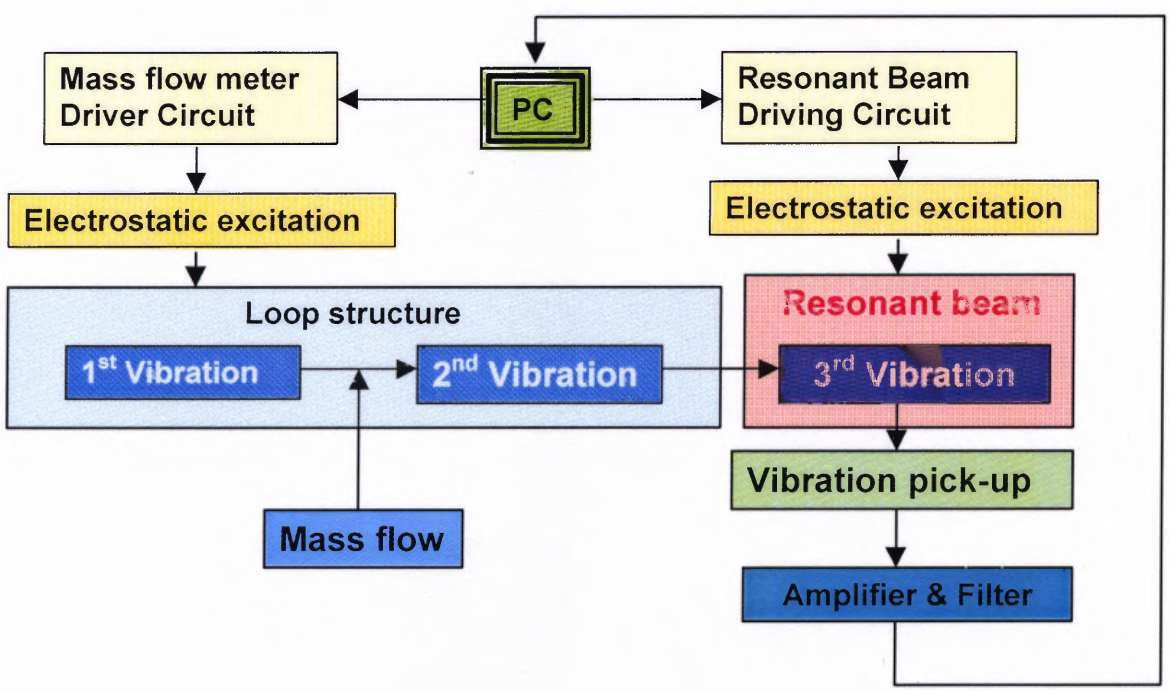

Figure 1.1 Schematic of resonant beam measurement for the Coriolis mass flow sensor.

1.4 Advantages and Disadvantages of Resonant Beam Measurement

This measurement technique has the potential for high dynamic range [31], good linearity, as well as quasi-digital output [15, 40] due to its high sensitivity. High dynamic range: frequency shift is consistent with wide dynamic range for large mass flow change. Good linearity: Based on FEA simulations, frequency shift is linear in response to the mass flow changes. The advantages of resonant measurement are the ability to detect very small forces with good output linearity. Quasi-digital output: The output is in the form of a sinusoidal signal whose frequency changes with flow. The output is quasi-digital in the sense that it can be converted to digital form using a high-frequency clock [31]. Another advantage of the resonant measurement is the intrinsic nature of the output being a frequency rather than the common physical variable of analog voltage. For higher bandwidth applications such as in a Coriolis mass flow sensor, the complexity of demodulation does increase but relatively simple implementations can be found.

The disadvantage is the high vacuum packaging affecting quality factor, requiring the hermetic sealing and the bonding technique [10]. And, for a resonant sensor operated open-loop, the measurement bandwidth is limited by the high quality factor mechanical response. However, when the resonant sensor is operated in the feedback loop of an oscillator circuit, the bandwidth is limited not by the mechanical response but the dynamics of the supporting amplifier. The bandwidth of the demodulation setup may limit the overall sensor bandwidth [31].

1.5 Organization of the Dissertation

This dissertation addresses resonant beam Coriolis mass flow sensing by presenting 1) an analytical study of the resonant beam, 2) the theory and design of a prototype MEMS Coriolis-based flow sensing device, including a proposed fabrication approach that includes provision for resonant beam detection, and 3) microfabrication results including the use of wafer bonding and deep reactive etching technologies to experimentally verify the resonant beam approach to Coriolis sensing. Chapter 2 describes the resonant beam sensing method, providing a simulation study of both static and dynamic resonant beam behavior for a MEMS Coriolis device. In Chapter 3, the function of Coriolis-type mass flow meters is presented along with a study of the relationship between the fundamental mechanical modes of a proposed device structure. Governing equations are developed to represent the modal frequency and stiffness-frequency relationship. Also, stress analysis is performed to elucidate the stress-frequency shift relationship in the resonant beam. In addition, the previous detection methods are discussed in Chapter 3 in comparison with the resonant beam method. In Chapter 4, the process design and fabrication is developed, including the use of wafer bonding and deep reactive ion etching (DRIE) technologies. Experimental verification studies are discussed with unresolved issues in Chapter 5.

CHAPTER 2

RESONANT BEAM MEASUREMENT

2.1 Resonant Measurement

Resonance in mechanical systems and its application to sensing and actuation will be studied in this chapter. In the case of mechanical systems near resonance, low-power driving at a specific input frequency results in large amplitude vibrations. In an application such as a gyroscope [31] where large amplitude motion is necessary, resonance is desirable. Resonance is valuable for micromechanical actuation and sensing [31]. In the case of sensing, the sensor has elements that function at their characteristic resonance frequency, and a change in the resonant characteristic of these elements may comprise the results of a measurement. For example, a measurement may be detected as a shift in the resonant frequency of the sensing element. Resonant sensing has been carried out in numerous devices for the measurement of pressure, acceleration, mass flow, specific gas, biological detection, and force. The resonator sensor element is often fabricated into a system-on-a chip device that delivers a variation of resonant sensor element characteristics as the measurand. A cantilever, a double-ended beam and a one-side clamped beam are examples of the resonant sensing factor. Resonant sensing is commonly used to detect changes in spring constant [7] or mass [31] of the resonating system. The change in either of these parameters can be examined as a shift in the resonant frequency of the system. A number of different techniques (such as capacitive, optical, piezoresistive) measure the displacement of the resonant device, observing the characteristics of the resonant system.

2.2 Mechanical Resonant Beam Measurement

A resonant beam responding to an external static axial load or static mass loading effect has been studied by many research groups [37]. The one-dimensional Euler-Bernoulli equation and the Rayleigh-Ritz energy method have been used. If a tensile force S is applied to a resonant beam, the differential equation of the beam under transverse loading in Figure 2.1 is [37]

$$\frac{\partial^2}{\partial x^2}\left(EI\frac{\partial^2 y}{\partial x^2}\right)-S\frac{\partial^2 y}{\partial x^2}=-\rho A\frac{\partial^2 y}{\partial t^2} \tag{2.1}$$

In the case of a beam, it is given by:

$$EI\frac{\partial^4 y}{\partial x^4}-S\frac{\partial^2 y}{\partial x^2}=-\rho A\frac{\partial^2 y}{\partial t^2} \tag{2.2}$$

Assuming that the beam executes one of its natural modes of vibration, the solution of equation is given by:

$$y=X\left(A\cos pt+B\sin pt\right) \tag{2.3}$$

where X is a normal function. Substituting equation (2.3) into equation (2.2), we have:

$$EI\frac{\partial^4 y}{\partial x^4}-S\frac{\partial^2 y}{\partial x^2}=\rho Ap^2X \tag{2.4}$$

The solution of this equation, satisfying the given end conditions, provides the matching normal functions. For example, both ends of the beam may be clamped. This condition is fulfilled by taking

$$X_i=\sin\frac{i\pi x}{l} \qquad \left(i=1,2,3,...,\infty\right) \tag{2.5}$$

Substituting this expression into equation (2.4), the equivalent angular frequency of vibration is given by [37]:

$$p_i = \frac{i^2 \pi^2 a}{l^2} \sqrt{1 + \frac{Sl^2}{i^2 EI\pi^2}} \tag{2.6}$$

where $a = \sqrt{EI/\rho A}$. This frequency is larger than that obtained after the axial force S is applied. In the lowest mode, the frequency can be given by:

$$f = \frac{\pi \cdot a}{2l^2} \sqrt{1 + \frac{Sl^2}{EI\pi^2}} \tag{2.7}$$

It can be simplified by:

$$f = f_0 \sqrt{1 + S\alpha} \tag{2.8}$$

Where $f = p/2\pi$, $i = 1$, and $\alpha = l^2 / EI\pi^2$ in the lowest mode. Axial force, S affects natural frequency shift. The frequency shift is theoretically proportional to the square root of axial force. Actually, this application is valid only when this beam is regarded as a string (length>>width).

In an example application, a resonant pressure sensor, the pressure-induced deflection is converted to strain in the resonating beam through the beam-diaphragm attachment point. This strain change causes a shift of the resonance frequency of the resonant beam.

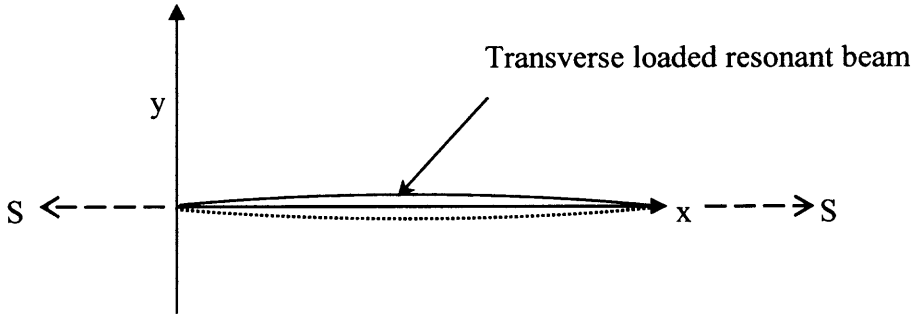

Figure 2.1 Schematic of axial stress applied resonant beam.

2.3 Dynamic Resonant Beam Measurement

Dynamic resonant vibration [8, 31] is a kind of nonlinear vibration. However, it can be approximated as a linear vibration with the parametric variation. The term 'parametric' means that an outside excitation action is accounted for as a time varying modification of a system parameter [8]. This is in marked contrast to the forced vibration problem where energy is simply fed into the system and the system responds, or not, dependent on the resonance condition in operation. Forced vibration problems do not show parametric variation as a result of an imposed forcing. On the other hand a parametrically excited system will show variation of a parameter with the excitation as long as an appropriate resonance is in place. Parametric systems respond when the frequency of excitation is coupled to the natural frequency by a resonance condition [31]. The characteristic differential equation that describes the development of the displacement of a resonating beam subjected to a drive force (F_d) is

$$m\ddot{x} + c\dot{x} + kx = F_d \tag{2.9}$$

In the case of a time-varying axial force, the spring constant of the system is modulated by the desired value (coupled as an axial force) and the time progress of the spring constant has to be clearly written out.

$$m\ddot{x} + c\dot{x} + (k_0 + k_1 \sin(\omega_e t))x = F_d \tag{2.10}$$

Where ω_e is the data frequency and k_0, k_1 are the spring stiffness constant and the changed spring stiffness value of a resonant beam. This equation (2.10) is called the Mathieu equation [8]. Under the assumptions that $k_0 >> k_1$, the solution can rewritten as[31]:

$$x = x_0(1 + \beta \sin(\omega_e t))\sin(\omega_0 - \beta \cos((\omega_e t) + \theta)) \tag{2.11}$$

where θ is an arbitrary phase term and $\beta = (\delta f_0 / f_e)$ is the modulation index.

The output spectrum is that of a typical frequency modulation. Under the assumptions of amplitude control, and the fact that the perturbation in the natural frequency due to the applied force is small relative to the modulating resonant frequency, and the excitation frequency of the "tuning fork" ($\delta f_0 << f_e, f_0$), the displacement can be written as [31]:

$$x = x_0 \sin(\omega_0 - \beta \cos((\omega_e t) + \theta)) \tag{2.12}$$

The direct frequency can be written as [31]:

$$f = f_0 + \beta f_e \sin(\omega_e t) \tag{2.13}$$

In terms of the applied axial force, the modulation index can be expressed as [31]:

$$\beta = \frac{\delta f_0}{f_e} = \frac{1}{f_e} \cdot \frac{S \alpha f_0}{2} \tag{2.14}$$

The modulation index varies inversely as the modulation frequency and is proportional to the amplitude of the applied axial force. The output frequency shift in response to the applied force is given as [31]:

$$\delta f_0 = \beta f_e = \frac{S \alpha f_0}{2} \tag{2.15}$$

This small value of frequency shift is a linear response to the applied force and strain change in the mechanical structure.

2.4 Summary

This chapter described the principle of mechanical resonance and its application to force sensing for a micromechanical device. The principle of resonant sensing modulates the effects of the measurand about the resonant characteristics of a simple micromechanical structure. Sensing Coriolis force that illustrates this measurement principle will be discussed in Chapter 3. The discussion of the key design issues for a micromachined Coriolis mass flow sensor required for optimizing resonant vibration in the sensor structure also in presented next in Chapter 3.

CHAPTER 3

SAMPLE STUDY FOR PSEUDO DYNAMIC RESONANT BEAM METHOD

3.1 Introduction

Knowing the mass flow rate is more valuable than the volume flow rate in many applications of flow measurement [16]. As an example, the mass of fuel, not the volume determines the range of an airplane. Thus, flow meters should show mass, not volume in this sort of application. Two common approaches are used to measure mass flow rate. The first approach is indirect: measure the volume flow rate and covert to a mass flow rate if the material density is known [16]. The second approach is to measure mass flow rate directly [16]. Both methods are currently possible and used in various applications. A number of angular-momentum concepts have been addressed for the gyroscope, the Coriolis meter, the twin-turbine meter, and etc. In fact, these meters have been commercialized [16]. These sensors are not constrained by flow profiles and fluid properties such as composition, pressure, temperature, flow density, and viscosity. Conventional Coriolis mass flow sensors have been built for liquid and gas applications but they are costly, and not designed for micro fluids. The first micromachined Coriolis mass flow sensor has been designed and fabricated [19]. The goal of MEMS Coriolis mass flow sensor research would be to commercially realize high sensitivity and high stability of true mass flow measurement in a miniature device [17, 19].

3.2 The Operation of the Coriolis True Mass Flow Meter

The actual operation of a Coriolis mass flow device is explained in this Section. Fluid flowing at mass flow rate (ϕ kg/s) passes through a Ω-shape pipe that is undergoing sinusoidal torsion vibration. Coriolis-type devices call for the fluid to be excited with an angular velocity whose vector is orthogonal to the fluid velocity V. The angular excitation is a rigid-body twisting about a fixed axis, and fluid flow is expressed not by a velocity profile, but by a single velocity V. The absolute acceleration $\ddot{r}$ of a point is given by [21]:

$$\ddot{r} = \ddot{R} + \omega \times (\omega \times \rho) + \dot{\omega} \times \rho + \ddot{\rho}_r + 2\omega \times \dot{\rho}_r \tag{3.1}$$

In this example, $R \equiv 0$, so $\ddot{R} = 0$, and $\dot{\rho}_r = V$. The flow meter sense and pick-off is through the bending angle θ. In equation (3.1), the only term of the Coriolis acceleration $2\omega \times V$ is interesting for the device concept. A Coriolis force of magnitude $(dM)(2\omega \times V)$ and direction opposite to $\omega \times V$ is provided by a factor of fluid mass dM at location ρ since a velocity changes sign from the right to the left of the Ω-type tube. The mass elements provide a Coriolis bending dF [16]:

$$dF = (2\omega \times V)(dM)L = (2\omega \times V)(\frac{\phi}{V} d\rho)L \tag{3.2}$$

$$F = \int_{-L_x/2}^{L_x/2} dF = 2\omega\phi L \int_{-L_x/2}^{L_x/2} d\rho = 2\omega\phi L_y L_x \tag{3.3}$$

The angular velocity is excited sinusoidally, so the Coriolis force is the form of sinusoidal function too. It performs as a driving torque, tending to bend the Ω-type tube; and since the Ω-tube bending frequency is well matched to this driving frequency in an ideal structure, the bending spring/mass system acts fundamentally as a spring of stiffness K_s, calculating the bending angle by [19];

$$\theta_B = \frac{2\omega L_x L_y}{K_s}\phi \tag{3.4}$$

In Figure 3.1, this torsion motion directs to an alternating angular motion around the fixed axis. The Coriolis force is not induced until a mass flow passes through the tube. This force is expressed along the cross product of the mass flow and the angular motion. The amplitude of this motion is proportional to the angle in between two vectors. The following relation for a ratio between the Coriolis angle and the excitation angle amplitude was derived [19]:

$$\frac{\theta_B}{\theta_T} = \frac{4\pi f_0 L_x L_y}{K_s}\phi \tag{3.5}$$

L_x is the loop length and L_y is the loop width. K_s is the bending spring constant of the structure. In other words, the torsion vibration is actuated externally with the lowest torsion resonant frequency.

The bending vibration, introduced by the Coriolis force is an induced bending mode, and the Coriolis force is given by $F_c = -2mV \times \omega$ where mV is the mass flow momentum and ω is the angular frequency of the 1st torsion vibration [16, 19]. The angular frequency of the 1st vibration leads to a periodic Coriolis force imposed orthogonal to the 1st vibration, causing the elastic structure to experience a 2nd bending vibration which is working in the bending mode of the tube structure. The frequency of the first vibration governs that of the second vibration. Of course, the amplitude of the second vibration is proportional to mass flow, but the main working frequency for bending is not much changed since the angular – 1st torsion vibration – frequency affects the frequency and amplitude of the 2nd vibration. While the density of flow affects the frequency of the 2nd vibration, the mass flow affects the amplitude of the 2nd vibration.

The maximum amplitude of the Coriolis motion occurs when the excitation is at resonance. Thus, the best signal to noise ratio is achieved at resonance excitation vibration. If the natural frequencies of torsion and bending modes are close to each other in an ideal structure, the amplitude of the bending mode due to the Coriolis force can be maximized – as will be discussed in Section 3.3 in detail.

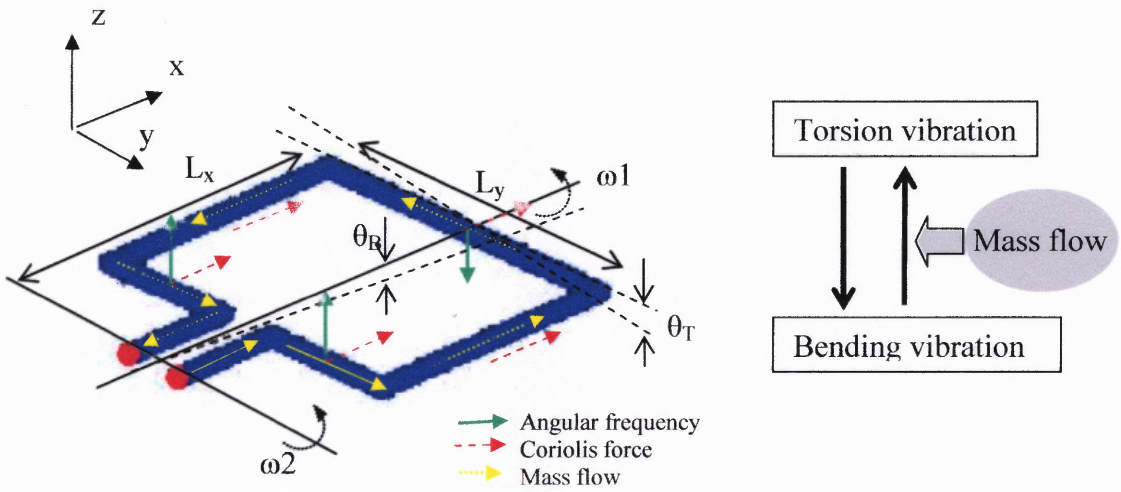

Figure 3.1 Bending and torsion vibration by Coriolis force; (a) Ω-shape structure, (b) schematic of system.

3.3 Structural Design Methodology

MEMS Coriolis-type mass flow devices have been studied for use in measuring small fluid flows [19,33]. Coriolis force in this kind of flow meter utilizes the mode change of the mechanical structure such as bending mode and torsion mode, respectively. The major advantage of a Coriolis mass flow measuring device is its sensitivity, and this sensitivity depends upon the relationship between the torsion and bending vibrations of the sensor. For maximum sensitivity, the mechanical energy of the torsion vibration should be fully transferred to that of the bending vibration. It is necessary to understand the coupling of these modes of vibration. Conventional 'Ω' shape Coriolis-type mass flow meters utilize two mechanical modes; bending and torsion. When the 'Ω' shaped tube is excited in the torsion mode of mechanical vibration, this tube structure adjusts its mode to the bending mode due to the Coriolis force of the flowing fluid. Conversely, when it is excited in the bending mode, it changes from bending to torsion. Because of this reason, the first bending and first torsion modes of mechanical vibration are important to Coriolis mass flow meters. Any mechanical structure has certain natural vibration modes. For example, suppose there is a cantilever. A cantilever beam has a bending mode in the lowest natural frequency of vibration. As the natural frequency increases, the vibration modes of the cantilever become their typical modes as shown in Figure 3.2, offered by the COVENTOR simulation software. Each structure has its own stable spring stiffness affecting its natural vibration. In order to maximize the Coriolis force, the natural frequencies at each modes of a mechanical structure should be close to each other since the frequency of torsion excitation is the same as the frequency of Coriolis bending vibration if the density of flowing fluids is constant even when the mass

flow is coming through the structure. Regardless of flowing fluids, the exciting torsion frequency dominates the detecting bending frequency. Thus, if these natural frequencies of torsion and bending modes are quite different, the torsion excitation vibration does not stay any more on the natural frequency of the Coriolis frequency and the amplitude of bending vibration becomes a small ration to the torsion excitation vibration.

As summarized, the device is operated in close complementary vibrations (mode1 and mode3) in the view of an energy conversion in order to get maximized amplitude ratio. The information of mass flow is enclosed in the peak amplitude of the 2^{nd} vibration and its effective actuation demands the frequency matching between the two complementary modes.

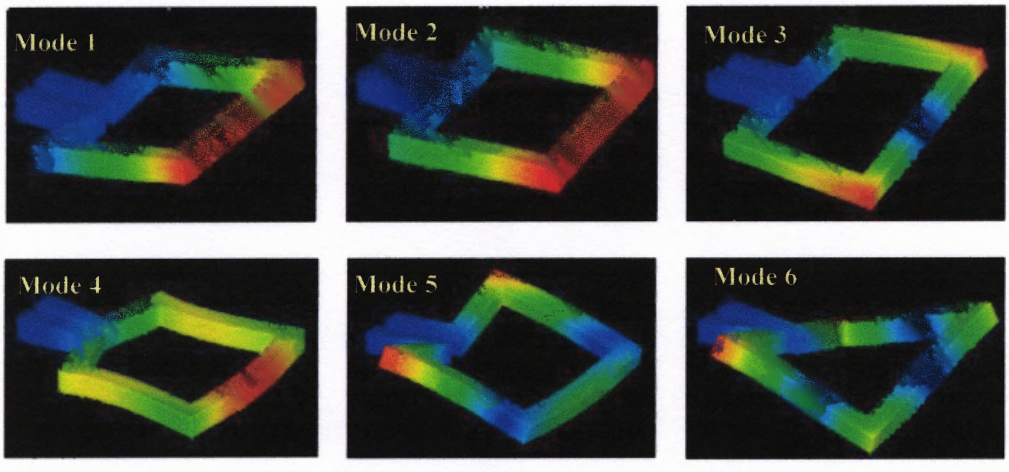

Figure 3.2 The vibrating modes of the cantilever-type tube loop structure.

Specific modeling and design of the structure is required to satisfy this requirement, the mode shapes of the 6 lowest orthogonal vibrations with natural frequencies are shown in Figure 3.2. The modeling is approached by Rayleigh's energy method. The spring stiffness of each mode determines its natural frequency given a constant mass of the structure in the equation (3.6). According to the requirement, the spring stiffness of the bending and torsion modes should be close to each other as per the ratio below in the equation (3.8). Based on Rayleigh's method, the natural frequencies are expressed as follows [34];

$$\omega_i = \sqrt{\frac{k_i}{m}} \qquad (i = 1, 2, 3, \ldots) \tag{3.6}$$

In each bending and torsion mode, the natural frequencies are given by:

$$\omega_B = \sqrt{\frac{k_B}{m}}, \quad \omega_T = \sqrt{\frac{k_T}{m}} \tag{3.7a, b}$$

The ratio of the frequencies mentioned earlier is as follows,

$$\frac{\omega_B}{\omega_T} = \sqrt{\frac{k_B}{k_T}} \tag{3.8}$$

Total spring constant is the sum of the spring constants of each prismatic part. In bending mode, the total spring constant of bending is composed of k_1, k_2, k_3, k_4, k_5, k_6, and k_7. More specifically, k_1, k_3, k_5, and k_7 are the bending spring constants, and k_2 and k_6 are the torsion spring constants. k_4 can be ignored since it is not displaced much.

$$k_B = k_1 \parallel k_2 \parallel k_3 + k_5 \parallel k_6 \parallel k_7 \tag{3.9}$$

$$k_B = 2(k_{b1} \parallel k_{t1} \parallel k_{b2}) \tag{3.10}$$

In torsion mode the situation is different; k_2 and k_6 are the bending spring constant, and k_1, and k_7 are the torsion spring constant. $k_3$and k_5 are both bending and torsion spring

constants. Furthermore as loop length increases, they become equivalent to bending spring constants and as loop length is short, k_3 and k_5 become equivalent to torsion spring constants. Therefore they do not have any bearing on the measurement.

$$k_T = k_1 \parallel k_2 \parallel k_3 + k_5 \parallel k_6 \parallel k_7 \tag{3.11}$$

$$k_T = 2(k_{t2} \parallel k_{b3} \parallel (k_{t3} + k_{b4})) \cong 2(k_{t2} \parallel k_{b3} \parallel k_{b4}) \tag{3.12}$$

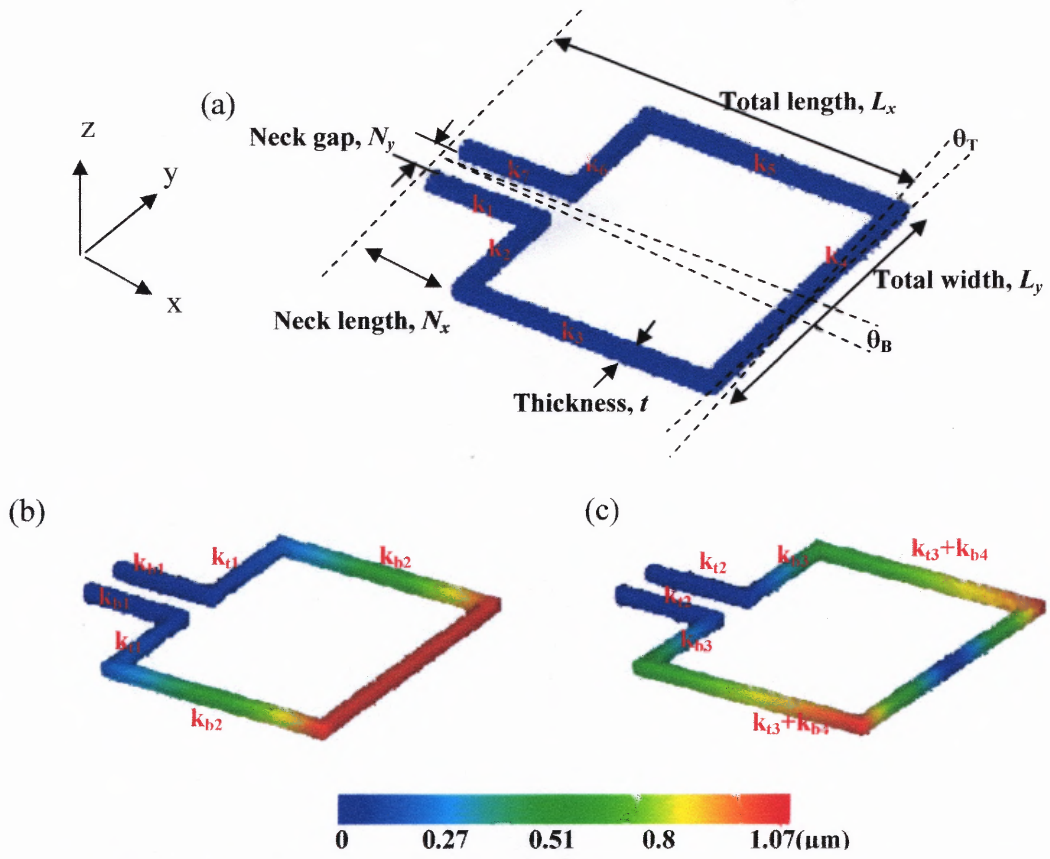

Figure 3.3 The displacement of loop structure in Coventor simulation software; (a) the simplified micromachined Coriolis mass flow sensor, (b) bending mode, (c) torsion mode.

In this investigation, various types of structures are explored using Coventor simulation software to verify the suggested theoretical assumption in Figure 3.4. and the simulation specifications and results of investigated structures are mentioned in Table 3.1. The simulation shows that the ratio ($\omega 1/\omega 3$) ranges from 0.4 to 0.9 in Table 3.1.

As a result, the T type of structure produced similar natural frequencies and thus, better sensitivity to mass flow, a key requirement as explained earlier in the Section. This simulation has shown to be the best structure with the frequency ratio of 0.88 in the sample 7 above. The simulation revealed that the structure has the closest frequencies when it has a T-type shape as in Figure 3.4. Based on the equation (3.5), of course, the smaller the bending spring constant is, the better the sensitivity will be, because the bending and torsion frequencies are closer. Using the optimized T structure overcomes this disadvantage and maintains a smaller bending spring constant.

The ideal T structure arrived at is fixed at the base. The cross bar of the T is free to move and as the mass flow passes through the length of the cross bar, the device is displaced. The resonant beam is also fixed at the base of the T and is attached to the middle of the length of the crossbar. Therefore, the displacement of the crossbar is transferred to the resonant beam.

Table 3.1 Investigated Simulation Specification and Results in Figure 3.4

Sample No.	Total length (μm)	Total width (μm)	Neck length (μm)	Neck gap (μm)	Bending frequency (ω_B, Hz)	Torsion frequency (ω_T, Hz)	Ratio (ω_B/ω_T)
Sample 1	3400	2300	750	300	7990	11600	0.69
Sample 2	3400	2300	0	2100	12288	27489	0.45
Sample 3	3400	2300	750	300	5289	12723	0.42
Sample 4	3400	2300	750	900	10295	20900	0.49
Sample 5	3400	2300	750	0	9314	18573	0.5
Sample 6	3400	2300	2150	300	10350	17081	0.61
Sample 7	2000	2300	750	300	29000	32940	0.88

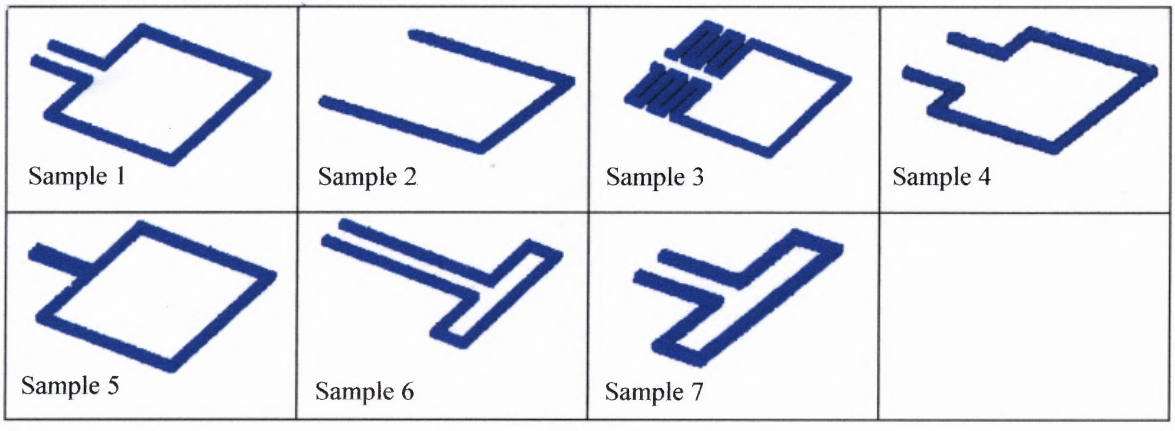

Figure 3.4 Various structures investigated in Coventor simulation software.

3.4. Resonant Beam Detection Method

Up to this point, structural modeling and design have been dealt with. In this Section, the detection method is developed and the conventional and optimized structures are explained. Also, the dynamic resonant beam detection method is investigated and compared with previous detection methods. A Coriolis mass flow sensor arrives at results by detecting Coriolis mechanical forces. Several alternate detection methods are already being used for mechanical force sensing and a review of these methods follows below.

3.4.1 Overview of Previous Detection Methods

Table 1.1 summarizes the common used mechanical sensing mechanisms and their features in micro machined devices. Important considerations include the needs for sensitivity and power consumption, linearity, a vacuum system, temperature coefficients, and so on when choosing such mechanisms.

A piezoresistor [24] has been used as a strain gage for a long time in the industry with the advantage of having a simple implanted microfabrication technique Change in gauge dimensions bring about proportional changes in resistance in the sensor. Therefore the sensitivity of gauges can be easily varied, depending on their design. All strain gauges can be very linear over the range of strain, which makes them useful in many applications. Strain sensors are a part of many MEMS devices, serving to measure strain change by the displacement of structures. In general, the sensitivity is expressed by the gauge factor (dimensionless),

$$GaugeFactor = \frac{\Delta R/R}{\Delta L/L} = \frac{\Delta R}{\varepsilon R} \tag{3.13}$$

The disadvantage of this method is that it is sensitive to temperature. In practice, temperature compensation resistors are required to adjust for errors caused by temperature and a Wheatstone bridge is required to maximize the output signal [24].

A capacitive (or electrostatic) method is one of the oldest and most accurate sensing mechanisms, and is commonly used in measurement systems. Capacitive displacement sensors have a simple structural design (one or more fixed plates, with one or more moving plates), but the capacitive method has a disadvantage in that it can not be batch-fabricated, but needs sacrificial micromachining or wafer bonding to create the gap the capacitor requires. Figure 3.5 illustrates the basic structure of a mass flow meter with the capacitance detection method. It is made of a silicon microtube and a glass substrate, anodically bonded together. The twisting angular motion is detected via capacitance measurements using the two electrodes located along the two sides of the tube structure. A capacitive transducer is not sensitive to temperature on condition that the material in the gap has a low-temperature coefficient than its dielectric coefficient. In most cases the noise performance of the capacitive sensors is superior piezoresistive sensors, particularly since surface micromachining techniques can produce extremely small gaps sensitive to minute capacitances [24]. Actually, the piezoresistive or capacitive method also plays a role in the resonant beam method. In fact, the capacitive method has been used as a vibration pick-up method to measure the transverse vibration of resonant beams as shown in Figure 3.5. Ultimately, the resonant beam method works by measuring the strain or displacement change, which can be detected by a piezorestor or a capacitor.

The optical method can be easily used to measure mechanical displacement through the reflecting angle in a testing set-up with a laser and a lateral photo-detector.

The optical method for a Coriolis mass flow sensor is shown in Figure 3.5(c). Here, the tube structure is electrostatically actuated by an external electrode. The amplitudes of the vertical displacement of the tube structure are detected by a two-dimensional lateral photodetector and a lock-in amplifier [19]. To make this system more accurate, the measurement set-up requires some distance, which is a disadvantage.

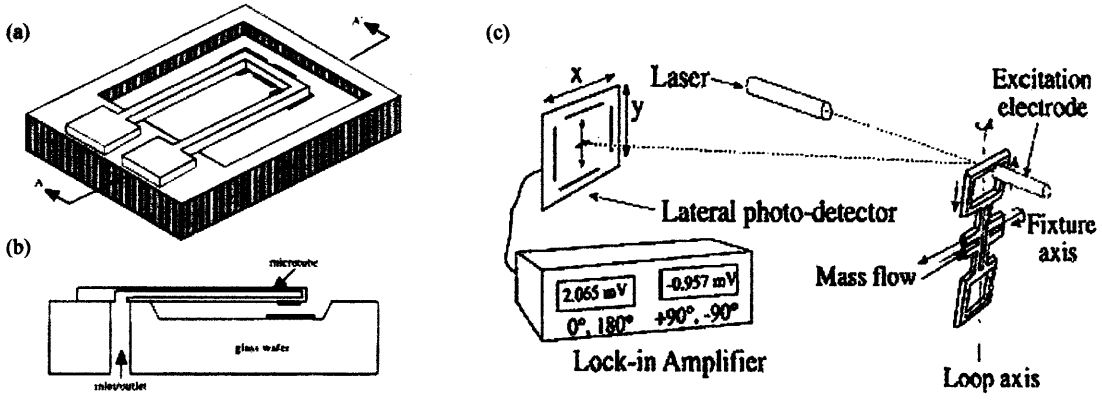

Figure 3.5 (a) A three-dimensional view and (b) a cross-sectional view of a micromachined mass flow sensor with the capacitive method [33] (c) a schematic of a measurement set-up for the optical detection method [19].

3.4.2 The Resonant Beam Method for Coriolis Force Detection

The resonant beam method is introduced in a micromachined Coriolis mass flow meter in this section. The focus will be on the relationship between a resonant beam and the Coriolis force since the relationship between the mass flow and the Coriolis force is already mentioned above in Section 3.2. Resonant beam measurement has already been

implemented in pressure sensors and accelerometers as a detection and read-out method due to its advantages [7,44]. However, this technique has never been used in a Coriolis mass flow measurement system. Three types of Coriolis mass flow sensors have been classified by signal detection and read-out techniques as mentioned in the previous Section: piezoresistive [16], capacitive [32], optical methods [19], this dissertation meanwhile introduces the innovative use of a resonant beam as the vibration pick-up for the Coriolis force, and hence the mass flow rate measurement.

The actual operation of a Coriolis mass flow sensor with a resonant beam involves three vibrations. The 1st vibration is actuated externally with the lowest tube torsion resonant frequency depending on flow density. The 2nd vibration, is introduced by the Coriolis force, and is an induced bending mode, where the Coriolis force is given by $F_C = -2M_f\vec{V}_f \times \vec{\omega}_1$ where $M_f\vec{V}_f$ is the mass flow momentum and $\vec{\omega}_1$ is the angular frequency of the 1st torsion vibration. Periodic $\vec{\omega}_1$ leads to a periodic Coriolis force imposed in a direction orthogonal direction of the 1st vibration, causing the elastic structure to undergo a 2nd vibration which is the bending mode of the tube structure. The measurement of mass flow now becomes the measurement of the peak amplitude of the 2nd vibration. As shown in Figure 3.6, the beam of the 3rd vibration is fixed with both ends on the tube, spanning the displacement of the 2nd vibration. As a result, the beam is periodically stretched or compressed. The resonant frequency of the beam under this periodic strain change will have a periodic shift and the detection of this frequency shift becomes the measurement of the amplitude of 2nd vibration, hence a measurement of the mass flow [44].

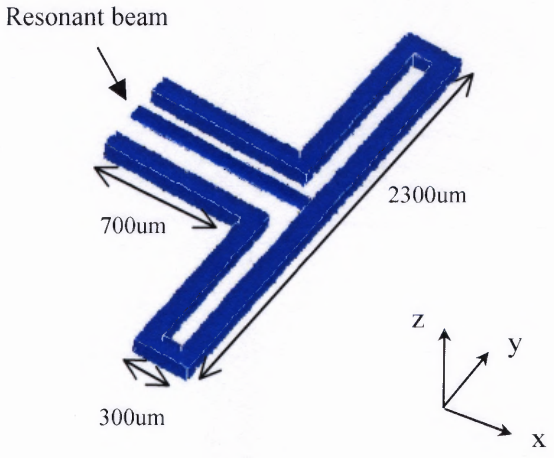

Figure 3.6 The Coriolis mass flow sensor with the resonant beam.

3.4.3 Detection Mechanism

The detection mechanism of the mass flow is explained in this section. The definition of mass flow is the mass of flowing materials per second. This mass flow change is known truly by the detection steps through the Coriolis principle. The resonant beam method is explained with a transient response in Figure 3.7. In the resonant beam, there are three detection steps: the Coriolis force to the axial force, the axial force to the resonant beam frequency, and the frequency modulation and pick up. The axial stress changes with the form of a sinusoidal function in Figure 3.7 (a, b) - the dashed line represents the stress change of the tube structure and the solid line that of the resonant beam. The normal cantilever is bending up and down without the total stress change. Its neutral axis stays on zero, which means there is no overall stress change. On the contrary, the beam (a) is only valid in the positive region because the buckling of the resonant beam occurs in the

negative region. Figure 3.7(c) shows the excited resonant frequency of the resonant beam. Figure 3.7(d) illustrates frequency shift produced by the stress change in Figure 3.7(a). The frequency increases when the beam is stretched more while the frequency increase is less when the beam is stretched less. The resonant beam method is possible enough to be contributed to measure the Coriolis force, and furthermore, the mass flow.

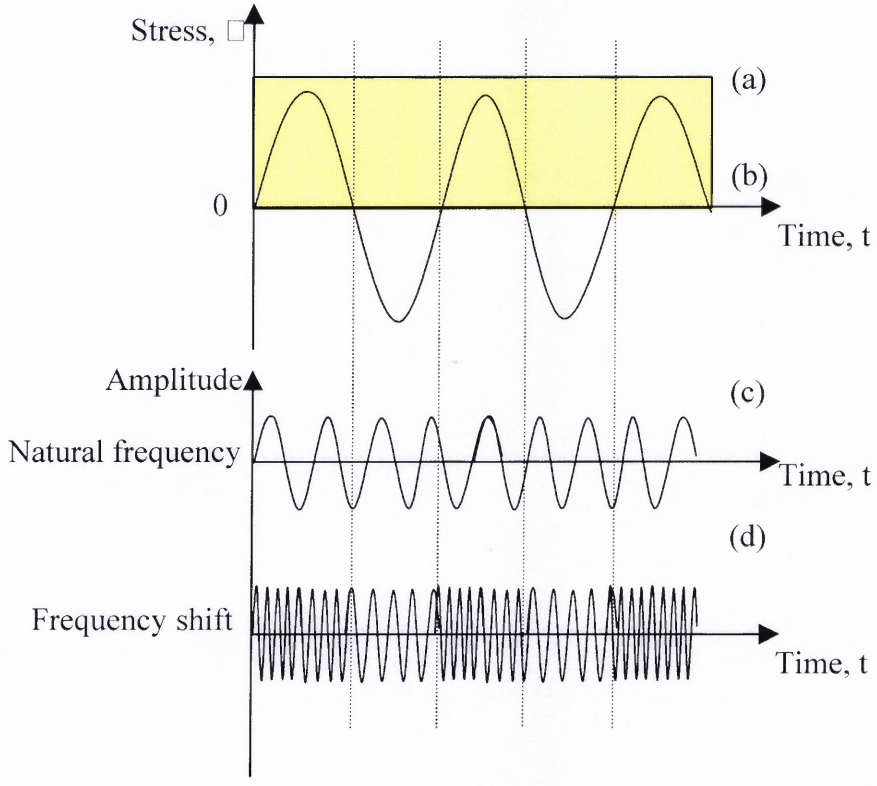

Figure 3.7 Schematic graph showing the transient response of the resonant beam measurement system; (a) actual stress, (b) bending of the free cantilever, (c) resonant driving vibration in natural frequency, (d) frequency response as affected by Coriolis force.

3.4.4 Stress Analysis of the Resonant Beam Method

The key to this device is the resonant beam. There is a thin beam connected to the top of the crossbar of tube structure in Figure 3.8. Since the entire tube is a cantilever-like structure, the tube itself will have no extra tension when it bends up or down. The tube structure bends down or up depending on the direction of mass flow and the angular motion of torsion vibration. When the tube is bent down or up by Coriolis force, the hypothetical beam - connected to middle of the tube - would not have axial force since it stays on the neutral axis if it is.

However, a beam connected to the top or bottom beam undergoes extra tensile and compressive stresses. The neutral axis of the beam itself, unlike that of the tube structure does undergo extra tensile stress since the neutral axis of the beam is located at the top surface region of the tube structure, which has a tensile stress when the tube with the beam is bending down as in Figure 3.8(a). A more detail explanation is presented in Figure 3.8(c). The tensile and compressive stresses of the top and bottom surfaces are cancelled out for the beam itself, but the extra stress change still occurs since the neutral axis of the beam lies on the top surface of the tube structure. Therefore, there is no doubt that the beam has an axial tensile stress even if this stress effect is small.

Based on the theoretical calculation, the strain change is ~5nm for 100kPa of Coriolis pressure on the $1000x100x2\mu m^3$ beam in Figure 3.11(b) below. This strain change induces 1kPa (0.2μN) of axial force applied to the resonant beam. Theoretical calculation results verify the statement that the total length of the resonant beam is changed and stretched, even if both the resonant beam and the tube structure are in bending mode. Simulation results in Figure 3.10 verify the statement that the total length

of the resonant beam is changed and stretched even if both the resonant beam and the tube structure are in bending mode.

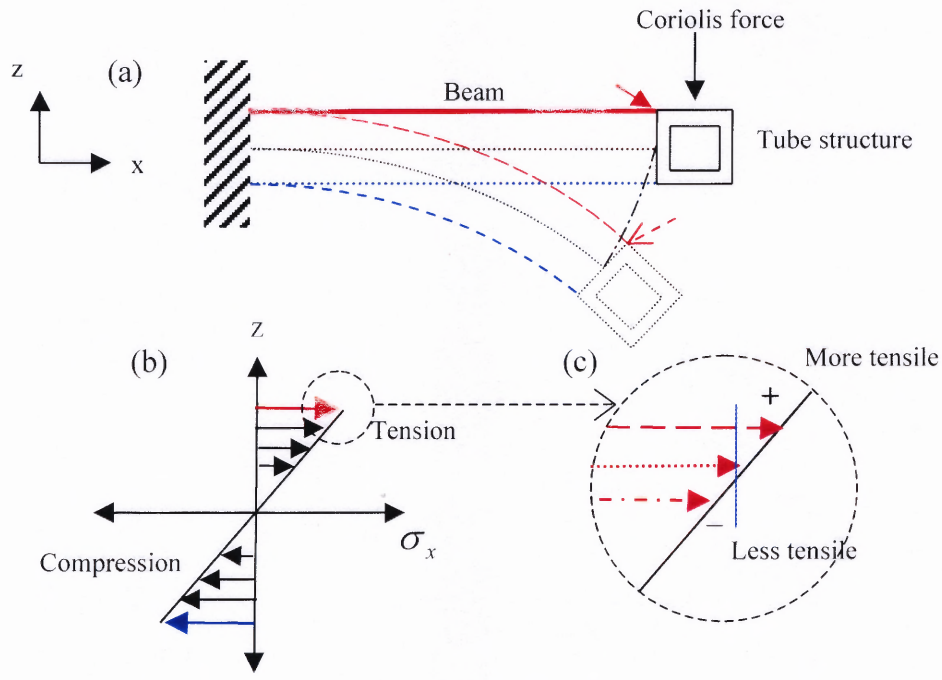

Figure 3.8 Stress and strain relationship of cantilever bending;(a) side view of Coriolis mass flow meter with resonant beam, (b)stress analysis, (c) magnified picture of (b).

3.4.5 Simulations for Stress Analysis

Sample 1 in Figure 3.4 is further investigated in Figure 3.9. The size of the device is mentioned in Table 3.1. The size of the beam is 2550um x 100um x 10um. This tube structure is a Ω-type suspended structure fixed to the wall in Figure 3.10(a). In order to prepare the simulation specifications, the Coriolis force must be known. The magnitude of the Coriolis force(N) per the mass flow (g/s), can be calculated by the equation shown above (3.3). The Coriolis force is around 20mN and the Coriolis pressure is about 20kPa with a torsion excitation frequency of 174kHz in the conventional structure (sample#1 in Figure 3.4).

The third vibration mode, which is the resonant beam vibration mode, is shown in Figure 3.9(a) according to COVENTORWARE MEMS simulation software. It enlightens that there is the vibration mode only for the resonant beam. In Figure 3.9(b), and as discussed in Section 3.2, the displacement profile is shown after the Coriolis force, represented by the arrows, is applied. The x-axis component profiles of displacement and stress on the resonant beam along A-A' in Figure 3.9(b) is shown in Figure 3.10. These results show that the entirety of the displacement profile is in the positive region and indicate that the tensile stress has been applied to the resonant beam even though the tube is bending freely.

Sample 7 in Figure 3.4 is further investigated in Figure 3.11. The size of the device is mentioned in Table 3.1. The size of the beam is 1000um x 200um x 2um. The tube structure is a Ω-type suspended structure fixed to the wall in Figure 3.6. In order to prepare the simulation specifications, the Coriolis force must be known. The magnitude of the Coriolis force (N) per mass flow (g/s) can be calculated by equation (3.3). The

Coriolis force per unit tube length (6600μm) of the sample #7 in figure 3 is around 50mN and the acting pressure is about 200kPa, where L_x is 300μm, L_y is 2300μm, a torsion excitation frequency is 36 kHz, and ϕ is 1g/s. A pressure of 100kPa is applied to the tube structure for the 0.5g/s of mass flow. Figure 3.11 depicts a pressure of 10kPa and a mass flow of 0.05 g/s is applied to visualize how the Coriolis force works on the structure.

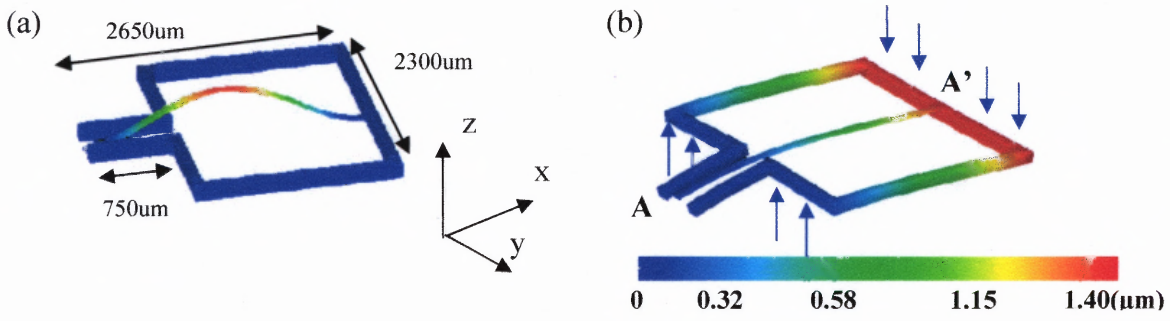

Figure 3.9 Conceptual pictures of a Coriolis mass flow meter with a resonant beam; (a) resonant beam displacement, (b) displacement after Coriolis force.

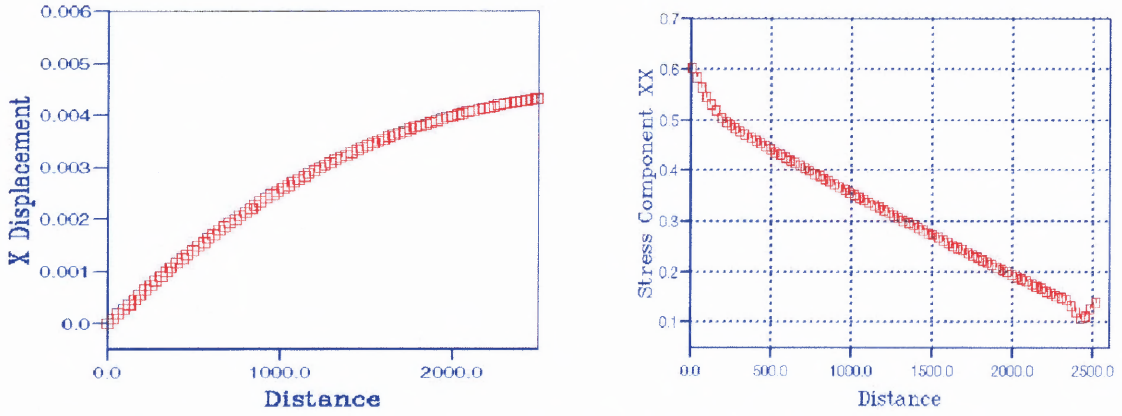

Figure 3.10 Stress and displacement profile along A-A' in Figure 3.10(b) with resonant beam according to the Coriolis force applied; x component of (a) displacement and (b) stress.

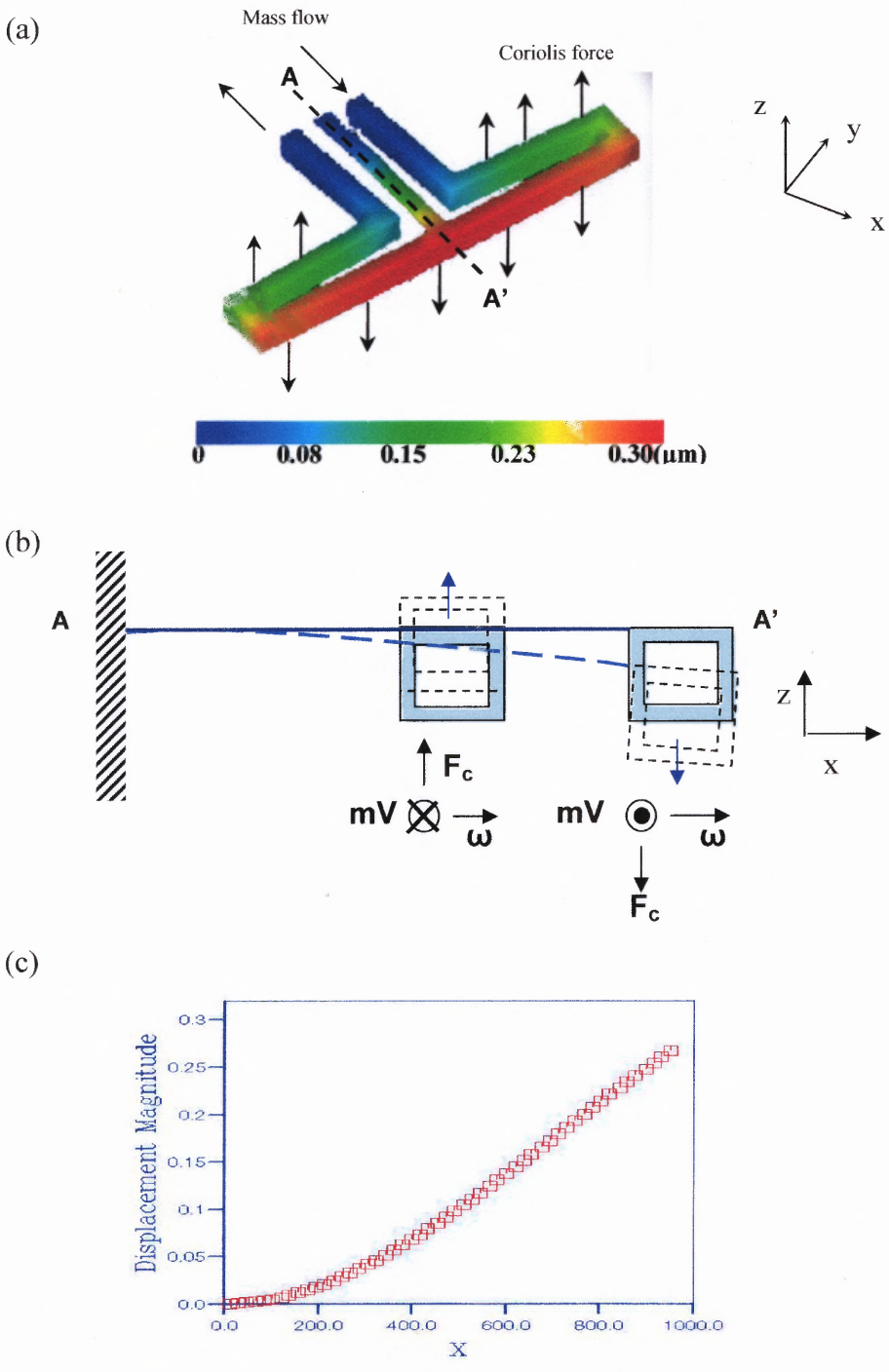

Figure 3.11 The structure and operation of the device; (a) simulation results after Coriolis force (10kPa) is applied, (b) side view of the device, (c) the displacement magnitude along A-A'.

3.4.6 Static Frequency Shifts for a Coriolis Force

Other research has already applied resonant beam technology to pressure sensors [19, 33]. The new proposed device surpasses prior developments by creating a dynamic strain change instead of merely a static one. The static resonant beam method is explained below. The equation for frequency shift is given by $f = \frac{1}{2\pi} \cdot \frac{n^2\pi^2}{l^2} \cdot \sqrt{\frac{EI}{\rho A}} \cdot \sqrt{1 + \frac{l^2}{n^2\pi^2 EI} S}$, where E is Young's modulus, I is the inertia of bending moment, ρ is density, S is an axial force, l is length, A is a cross-section, n is the vibration mode. The Coriolis force is transferred to strain in the resonating beam via the tube loop structure. The beam is fixed at both ends within the tube loop structure and any strain change causes a shift of its resonant frequency [19]. The beam is periodically stretched or compressed by the bending vibration of the tube. In the Pseudo Dynamic model, the resonant frequency of the beam under this periodic strain change will have a time-varying frequency shift. The time-varying frequency shift is capable of measuring the variations in bending vibration amplitude, and thus is a dynamic measurement of mass flow rather than a static measurement of pressure alone.

Despite being a very different structure, suitable for very different applications, studying the static resonant beam method can provide useful insights into the Pseudo Dynamic resonant beam measurement device. The relationship between strain change and pressure illustrated by the equation above can apply to the relationship between the strain and Coriolis force in a PD sensor because the frequency of the resonant beam is a function of strain change as in above equation. The Coriolis force-dependent strain in the beam is numerically simulated using finite-element method (FEM) analysis. Simulation results of a new designed structure show a 1% frequency shift per 100kPa Coriolis force

in figure 3.14 and table 3.3 while the theoretical calculation shows a 3% frequency shift. The simulation results show the strain change to affect the frequency shift in table 3.3. The Coriolis effect makes the strain change affect the frequency change and the resulting frequency shift moves to a higher range since the resonant beam bends downward and the stress on the beam is tensile. It expresses a linear response to the Coriolis force caused by the mass flow. In the following paragraphs, the characteristics and advantages of the Pseudo Dynamic Resonant Beam Method will be discussed.

As mentioned above, the resonant beam method was first appl;ied in pressure sensors, wherein a resonant beam is built in or connected to the membrane structure. The pressure caused membrane bending which induced an axial tensile S in the beam, the resonant frequency of which varied with the tensile force. Thus the pressure was measured. The partial differential equation that describes the transverse oscillation of such a beam under a constant axial tensile S is given by Timoshenko [37]

$$EI\frac{\partial^4 y}{\partial x^4} - S\frac{\partial^2 y}{\partial x^2} = -\rho A\frac{\partial^2 y}{\partial t^2} \tag{3.14}$$

where E, the Young's modulus, I, the moment of inertia of the cross section of the beam, S, the axial tensile acted along the length of the beam, ρ, the density of the beam, and A, the cross area of the beam, are all constants. By using the method of variable separation, we have

$$y(x,t) = X(x)P(t) \tag{3.15}$$

Substitution of (3.15) into Eq. (3.14) leads to

$$EI\frac{d^4 X}{dx^4}P - S\frac{d^2 X}{dx^2}P = -\rho AX\frac{d^2 P}{dt^2} \tag{3.16}$$

Division of Eq. (3.16) by $X(x)P(t)$ yields

$$\frac{EI\dfrac{d^4X}{dx^4} - S\dfrac{d^2X}{dx^2}}{X} = \frac{-\rho A\dfrac{d^2P}{dt^2}}{P} = \lambda \tag{3.17}$$

where λ, the eigenvalue of Eq. (3.14), is a constant and depends on the boundary conditions of the beam.

Thus

$$\rho A\frac{d^2P}{dt^2} + \lambda P = 0 \tag{3.18}$$

$$EI\frac{d^4X}{dx^4} - S\frac{d^2X}{dx^2} - \lambda X = 0 \tag{3.19}$$

Eq. (3.18) is the equation of motion of a simple harmonic oscillator, which has the general solution

$$P(t) = e^{\pm i\omega t} \tag{3.20}$$

where

$$\omega = \sqrt{\frac{\lambda}{\rho A}} \tag{3.21}$$

The solution of Eq. (3.19) is

$$X(x) = e^{\pm i\gamma x} \tag{3.22}$$

The eigenvalue γ depends on the boundary condition and the mode of vibration of the beam or string

$$\gamma = \frac{n\pi}{l} \tag{3.23}$$

where l is the length of the beam or string,

$$n = 1, 3, 5, \ldots \tag{3.24}$$

for the case of both ends simply supported, and

$$n = 2, 4, 6, \ldots \tag{3.25}$$

for the case of both ends rigidly supported.

Substituting (3.22) to Eq. (3.19) yields

$$EI\gamma^4 + S\gamma^2 - \lambda = 0 \tag{3.26}$$

Thus, the resonant frequency of the resonant beam is expressed as

$$\omega = \sqrt{\frac{EI}{\rho A}} \frac{n^2\pi^2}{l^2} \sqrt{1 + \frac{l^2}{n^2\pi^2 EI} S} \tag{3.27}$$

By measuring the resonant frequency (3.27) we can measure the signal which affects the beam's axial tensile *S*.

3.4.7 Simulations of Frequency Shifts

Simulations are investigated to examine the descriptions given in the previous Section. Optimization of the structure design also affects the modeling and design of the resonant beam. Figure 3.12 shows the modes of a conventional sensor structure with a resonant beam. The frequency ratio of sample 1 with the beam is low (~0.48) since the ratio of bending mode to torsion mode for Coriolis effect has been changed from mode 1 (7990Hz)/mode 3 (11600Hz) to mode 1 (9198Hz)/mode 4 (174338Hz) after the beam structure is added due to structural vibration modes, whereas that of sample 1 without beam is not really low (~0.6). The fourth mode is only for the beam vibration. Since the mode frequency for the beam is between bending and torsion frequencies, it may be coupled with those frequencies. Resonant beam frequency should be larger than the bending and torsion frequencies in order to distinguish the frequency of the beam from the bending and torsion frequencies.

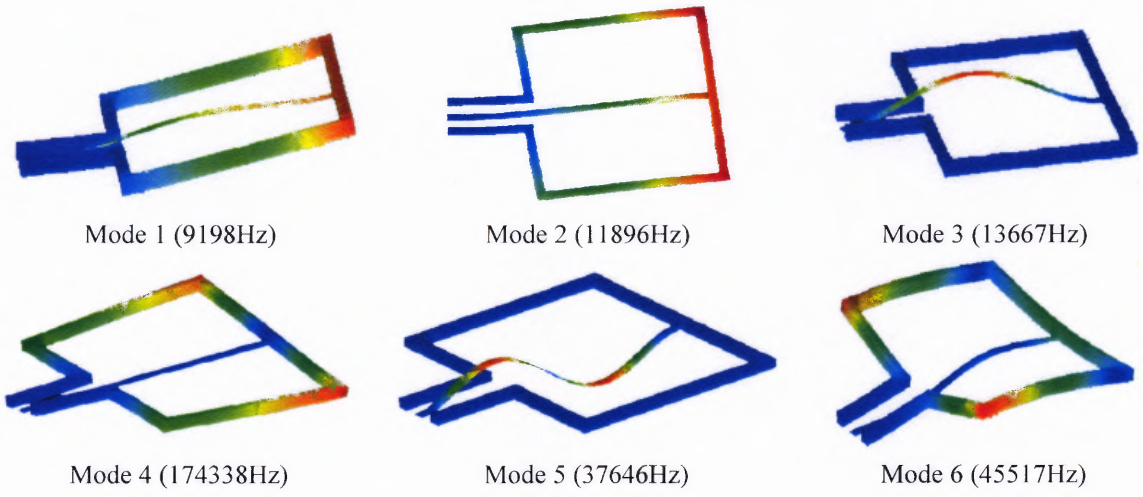

Figure 3.12 Modes of the structure; mode 1 and mode 4 are bending and torsion modes, mode 3 is first bending mode only for the resonant beam.

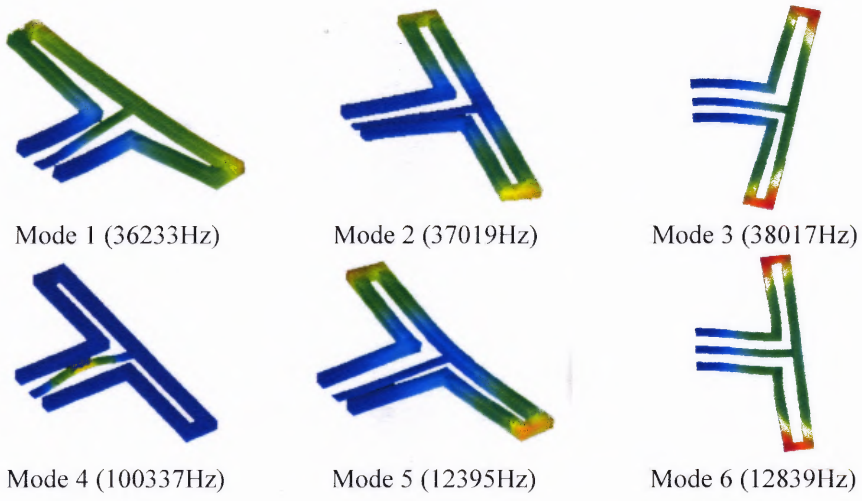

Figure 3.13 Vibration modes of structure from 1st to 6th mode.

Resonant beam frequency can be controlled by the structural design. Figure 3.13 shows simulation results for each vibration mode of the investigated structure according to COVENTORWARE MEMS simulation software. The fourth vibration mode, which is the resonant beam vibration mode itself, is shown and it is evident that this is the vibration mode only for the resonant beam and is distinct from the other modes.

After optimizing torsion and bending frequency to be similar with the ratio of 0.88, the resonant beam frequency rises clearly beyond the torsion and bending modes. Mode 4 differs from Mode 1 by a factor of three. As reminded of the Section 3.4.6, this frequency difference should be larger for the optimization of the Coriolis force and the PD resonant beam method. Simulation for resonant beam alone shows a parametric effect when even small z-direction displacement is applied to end of beam. The size of the simulated resonant beam is 1000 (length) x 100 (width) x 2 (height) μm^3. Each end of the beam is clamped and one end is displaced along the z-axis from 0 to 1μm. The travel range is considered to be 30 % (i.e. 0.74μm) pull-in displacement of the 2μm gap due to the pull-in effect.

Simulation results with a new designed structure show linear response to the Coriolis force of mass flow. Basically, this parametric linear effect is valid in small Coriolis forces so that this sensor responds linearly as seen in Figure 3.14 and Table 3.2.

Based on the theoretical calculation, the strain change is ~5nm by the 100kPa of the Coriolis pressure on the $1000x100x2\mu m^3$ beam in Figure 3.11(a). This strain change makes the 1kPa (0.2μN) of axial force applied to the resonant beam. And, then this axial force affects the 3% of frequency shift. Theoretical calculation results verify the

statement that the total length of the resonant beam is changed and stretched even if both the resonant beam and the tube structure are in bending mode, shown in Table 3.3.

The natural frequency of mode 4 differs from that of mode 1 by a factor of around 3. This frequency difference should be at least 10 times larger for the optimization of the Coriolis force and the Pseudo Dynamic (PD) Resonant beam method. This will be explained in detail later.

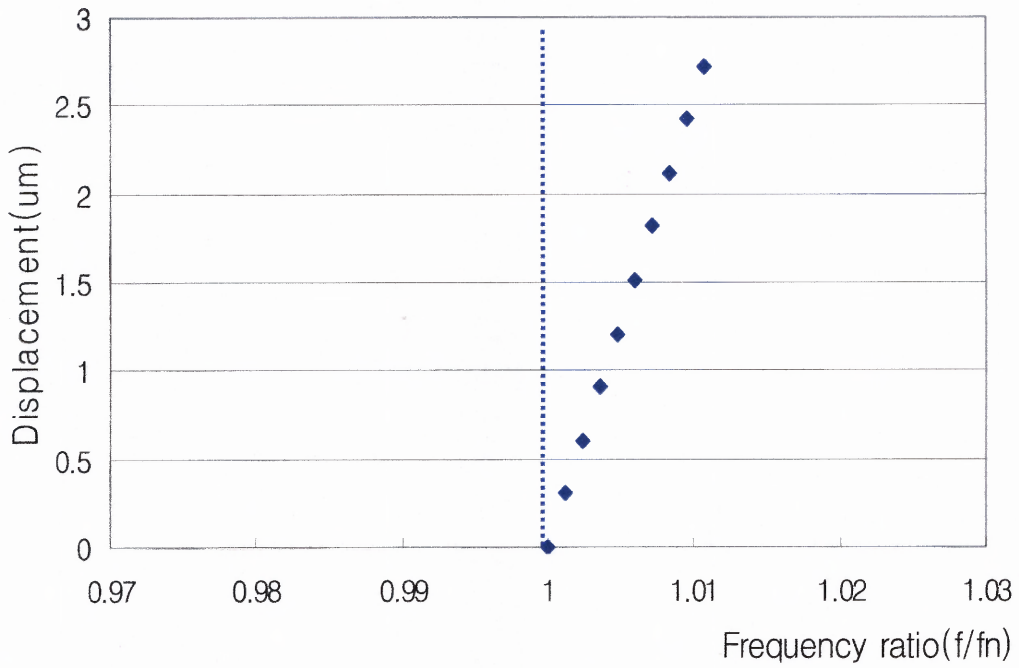

Figure 3.14 Linear resonant beam frequency shifts by small z-direction force.

Table 3.2 Simulation Results for the Relationship between Coriolis Force and Natural Frequency Shifts

F(kPa)	Frequency(Hz)	Shift(Hz)	Displacement(um)
0	100337	0	0
10	100458	121	0.303
20	100579	242	0.605
30	100699	362	0.907
40	100818	481	1.211
50	100937	600	1.513
60	101056	719	1.816
70	101173	836	2.119
80	101290	953	2.421
90	101406	1069	2.724
100	101522	1185	3.026

Source: Coventor (MEMS simulation) software

Table 3.3 Comparison between Calculation and Simulation

F(kPa)	Frequency(Hz)		Shift(Hz)	
	Calculation	Simulation	Calculation	Simulation
0	131000	100337	0	0
100	134930	101522	3930 (3%)	1185 (1%)

3.4.8 The Pseudo Dynamic Resonant Beam Method

All of the above equations also apply to the Pseudo Dynamic method. However, when the signal being measured is time varying, such as the pressure sensor used as an acoustic sensor, an accelerometer with varying acceleration, or the Coriolis flow meter, wherein an oscillating torque with frequency ω_s is applied to the sensor to generate Coriolis force, the tensile S is a function of time, varying with the measured signal. By adapting the governing equations of the Static Resonant Beam Method, the basic design principles of the Pseudo Dynamic method become clear. Equation (3.14) is modified as

$$EI\frac{\partial^4 y}{\partial x^4} - S(t)\frac{\partial^2 y}{\partial x^2} = -\rho A\frac{\partial^2 y}{\partial t^2} \tag{3.28}$$

The method of variable separation gives

$$y(x,t) = X(x,t)P(t) \tag{3.29}$$

$$\frac{EI\dfrac{\partial^4 X}{\partial x^4} - S(t)\dfrac{\partial^2 X}{\partial x^2}}{X(x,t)} = \frac{-\rho A\dfrac{d^2 P}{dt^2}}{P(t)} = \lambda(t) \tag{3.30}$$

Eq. (3.18) and (3.19) become

$$\rho A\frac{d^2 P}{dt^2} + \lambda(t)P = 0 \tag{3.31}$$

$$EI\frac{\partial^4 X}{\partial x^4} - S(t)\frac{\partial^2 X}{\partial x^2} - \lambda(t)X = 0 \tag{3.32}$$

A second variable separation of t and x yields

$$X(x,t) = Q(t)e^{i\gamma x} \tag{3.33}$$

Substitution of (3.33) to (3.32) yields

$$EI\gamma^4 + S(t)\gamma^2 - \lambda(t) = 0 \tag{3.34}$$

and Eq. (3.31) takes the form of

$$\rho A\frac{d^2P}{dt^2}+[EI\gamma^4+S(t)\gamma^2]P=0 \tag{3.35}$$

Assuming

$$S(t)=S_o+S_s\sin\omega_s t \tag{3.36}$$

where S_0 is the static axial tensile along the beam or string, S_s the amplitude of the tensile variation due to the signal under measurement, and ω_s the variation frequency of the signal. Let

$$\frac{EI\gamma^4+S_o\gamma^2}{\rho A}=\omega_o{}^2 \tag{3.37}$$

$$\frac{S_s\gamma^2}{\rho A}=\omega_1{}^2 \tag{3.38}$$

and Eq. (3.36) is simplified as

$$\frac{d^2P}{dt^2}+(\omega_o{}^2+\omega_1{}^2\sin\omega_s t)P=0 \tag{3.39}$$

Generally, for a linear differential equation with non-constant coefficient such as

$$\frac{d^2P}{dt^2}+[\omega(t)]^2P=0 \tag{3.40}$$

$\omega(t)$ is not the intrinsic or resonant frequency of the system. Neither

$$P(t)=\exp[\pm i\omega(t)t] \tag{3.41}$$

nor

$$P(t)=\exp[\pm i\int_0^t\omega(t)dt] \tag{3.42}$$

is the solution of the equation of motion (3.40). Substituting (3.41) to Eq. (3.40), we have

$$2i\omega'+(i\omega''-2\omega\omega')t-\omega'^2 t^2=0 \tag{3.43}$$

as the requirement for (3.41) to be the solution of (3.40). Substitution of (3.42) to Eq. (3.40) yields

$$\omega'(t)=0 \quad or \quad \omega=const \tag{3.44}$$

as the requirement for (3.42) to be the solution of Eq. (3.40).

Note that the instantaneous angular velocity of the "solution" (3.41) is

$$\frac{d\phi}{dt}=\omega(t)+t\omega'(t) \tag{3.45}$$

while the instantaneous angular velocity of the "solution" (3.42) is

$$\frac{d\phi}{dt}=\omega(t) \tag{3.46}$$

For the case of

$$|\omega(t)|>>|t\omega'(t)|\approx 0 \tag{3.47}$$

the difference between (3.41) and (3.42) is insignificant or negligible when the instantaneous behavior of the system is concerned. As (3.42) is written in the same form as in the widely used signal frequency modulation (FM), we will use (3.42) instead of (3.41) in our future discussion.

Note that for Eq. (3.39), which is a special case of Eq. (3.40), we have

$$\omega=\sqrt{\omega_o^{\,2}+\omega_1^{\,2}\sin\omega_s t}=\omega_o(1+\frac{1}{2}\frac{\omega_1^{\,2}}{\omega_o^{\,2}}\sin\omega_s t-\frac{1}{8}\frac{\omega_1^{\,4}}{\omega_o^{\,4}}\sin\omega^2{}_s t+\cdots)\approx\omega_o(1+\frac{1}{2}\frac{\omega_1^{\,2}}{\omega_o^{\,2}}\sin\omega_s t) \tag{3.48}$$

under the condition

$$\omega_o>>>\omega_1 \tag{3.49}$$

In addition, if we have

$$\omega_o >> \omega_s \tag{3.50}$$

then we can show that

$$P(t) = \exp[\pm i(\omega_o t + \frac{1}{2}\frac{\omega_1^2}{\omega_o}\int_0^t \sin\omega_s t dt] \tag{3.51}$$

or

$$P(t) = \exp[\pm i(\omega_o t - \frac{1}{2}\frac{\omega_1^2}{\omega_o\omega_s}\cos\omega_s t] \tag{3.52}$$

is the approximate solution of equation (3.39) [2]. Note that the time derivative of the phase or the instantaneous angular velocity is

$$\frac{d\phi}{dt} = \omega = \omega_o(1 + \frac{1}{2}\frac{\omega_1^2}{\omega_o^2}\sin\omega_s t) \approx \sqrt{\omega_o^2 + \omega_1^2\sin\omega_s t} \tag{3.53}$$

Such a dynamic system with slowly varying tensile $S(t)$ that satisfies the conditions (3.49) and (3.50) is called a pseudo-dynamic system, wherein the result of the case with a constant tensile force can be used.

Substitution of Eq. (3.37) and (3.38) to Eq. (3.49) yields the first design rule of the pseudo-dynamic resonant beam sensor

$$EI\gamma^2 + S_o >> S_s \tag{3.54}$$

For the lowest mode of beam oscillation, (3.49) becomes

$$EI\frac{\pi^2}{l^2}\gamma^2 + S_o >> S_s \tag{3.55}$$

for the resonant beam with both ends simply supported, and

$$EI\frac{4\pi^2}{l^2}\gamma^2 + S_o >> S_s \tag{3.56}$$

for the resonant beam with both ends rigidly supported.

Eq. (37) is a condition imposing on the bandwidth or the varying rate of the measurand, such as pressure or acceleration, which can be measured. The primary reason for this limitation is related to the main advantage of the resonant beam (or string) method – the quasi-digital output of the frequency shift. Typically, it is required that

$$\omega_s < 0.01 \sim 0.001\omega_o \tag{3.57}$$

When the resonant sensing principle is adapted to the Coriolis force true flow meter, Eq. (44) imposes a serious restriction on the design of the device structure, since the Coriolis force is proportional to ω_s, the frequency of the torque of torsion or bending that generates the variation of the tensile S in the resonant beam.

$$S(t) \propto \omega_S(t) \tag{3.58}$$

The resonant beam frequency should be 10 times or more larger than the Coriolis bending frequency in order to get valid output for the frequency demodulation. Thus a more precise name for this specific device might be a 'Pseudo-dynamic (PD) resonant beam method' since the resonant frequency shift of the Coriolis force becomes that of the pressure sensor if the Coriolis frequency becomes more than 10 times smaller the resonant beam frequency. And, the PD resonant beam method makes the frequency pick-up an easy matter. The peak frequency shift of the beam responds to the modulations of the Coriolis force frequency and is given by:

$$f = f_{rb} + f_{rb1}\sin(\omega_c t) \tag{3.59}$$

Thus, the frequency shift, f_{rb1}, shows the mass flow changes ultimately by a sequence of detecting mechanisms in the Coriolis vibration system in the equation (3.59).

$$Mass\_flow(g/s) \propto Coriolis\_force(N) \propto strain\_change \propto f_{rb1}$$

One issue occurs concerning the Coriolis force and the PD resonant beam method. It is at times difficult to maintain the correct frequency differential required for optimum functioning of the PD resonant beam method. The Coriolis force increases according to the frequency of the torsion excitation in the equation (3.3) - $F = 4\omega\phi L_x L_y$, but the PD resonant beam method requires the frequency of torsion excitation to be much smaller than the frequency of resonant beam excitation. If the frequency of the torsion excitation increases in order to increase the Coriolis force, the frequency of this torsion may rise to equal the natural resonant frequency of the resonant beam. In order to maintain the required difference, the resonant beam excitation should be modified while the frequency of the torsion excitation is fixed.

There are two options to modify it; the usage of a higher mode of natural frequency and some modification of the structure. Although it is true that the frequency of the resonant beam increases with a shorter and thicker structure, it can not be increased beyond a factor of 10 due to the limitations of the structure itself, therefore the first option is preferred. The simulation data based on the new device shows frequencies of 36 kHz torsion and 100 kHz for the resonant beam respectively. This frequency difference (less than a factor of three) can be improved by using the two modification options mentioned above to meet the requirement, which is a frequency difference in the range of a factor of 10. If the requirement is met, a sensitivity of 0.02/g/s is realized with the PD resonant beam method. If the required difference is not met, the PD method can still function with a difference that is only in the range of a factor of about 3.

In this case, an additional digital converter or Fast Fourier Transfer (FFT) helps to refine the sensitivity to detect a 1% frequency shift per g/s. The proposed device achieves

a frequency difference of about a factor of three and using FFT manages to function within the parameters of success for a Resonant Beam Sensor.

3.5 Frequency Measurement

Figure 3.15 shows the measurement set-up to test the frequency shift of the beam. The electromechanical behavior of the electrostatically driven and sensed one-port beam resonator can be modeled by examining its equivalent electrical circuit. The impedance, $Z(\omega)$ of the equivalent circuit is given by:

$$Z(\omega) = \frac{V(\omega)}{I(\omega)} = \frac{1}{j\omega C_{rb}} + \frac{1}{j\omega C_{ref}} \tag{55}$$

where C_{rb} is the equivalent capacitor for resonant beam and C_{ref} is the reference capacitor. The output voltage that can be measured is calculated by:

$$V_0(\omega) = \frac{Z_{ref}(\omega)}{Z(\omega)} \cdot V(\omega) = \frac{C_{ref}}{C_{rb} + C_{ref}} \cdot V(\omega) \tag{56}$$

where $Z_{ref}(\omega)$ is the impedance for reference capacitor. After Coriolis force is applied, the capacitance of the resonant beam varies with the Coriolis vibration in the time domain, given by:

$$C_{rb}(t) = C_{rb0}(\sin(\omega_{rb}t + \delta\sin(\omega_c t)) + C_c \sin(\omega_c t) \tag{57}$$

where C_{rb0} is the initial capacitance fore the resonant beam, C_c is the capacitance for the Coriolis force, ω_c is the Coriolis frequency, ω_{rb} is the resonant frequency, and δ is the frequency shift. Thus, the output voltage is shown by:

$$V_0(t) = \frac{C_{ref}}{C_{rb0}(\sin(\omega_{rb}t + \delta\sin(\omega_c t)) + C_t \sin(\omega_c t) + C_{ref}} \cdot V(t) \tag{58}$$

This output voltage is measured through a digital converter and a FFT in Figure 3.15.

In the above circuit and simulations, 100kHz of beam excitation was applied, with a 1% frequency shift coupled with a Coriolis frequency of 36kHz. These mixed frequencies can be separated clearly by fast Fourier transfer (FFT) with a high sampling rate under the condition that the damping effect is ignored as in Figure 3.16; (a) time domain, (b)and(c) frequency domain. The PD Resonant Beam Sensor device is currently in the fabrication process.

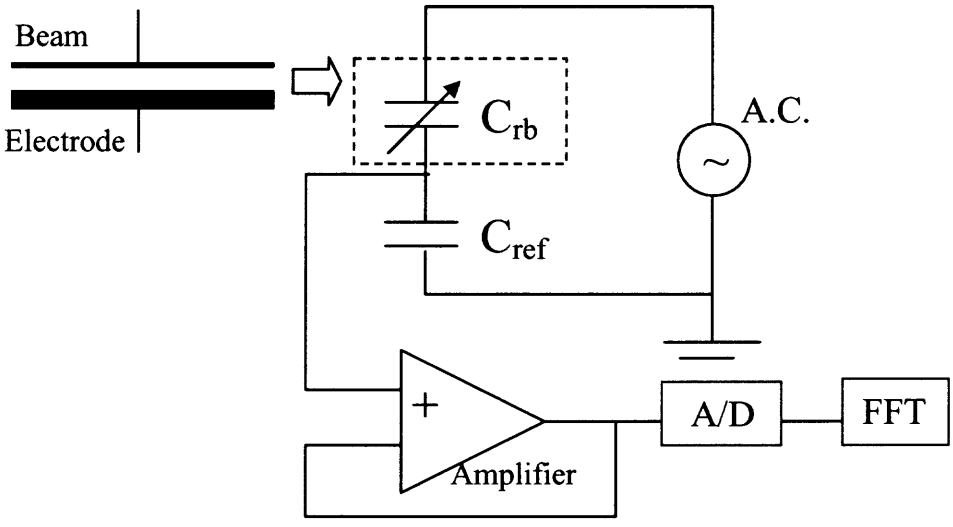

Figure 3.15 Schematic of measurement set-up.

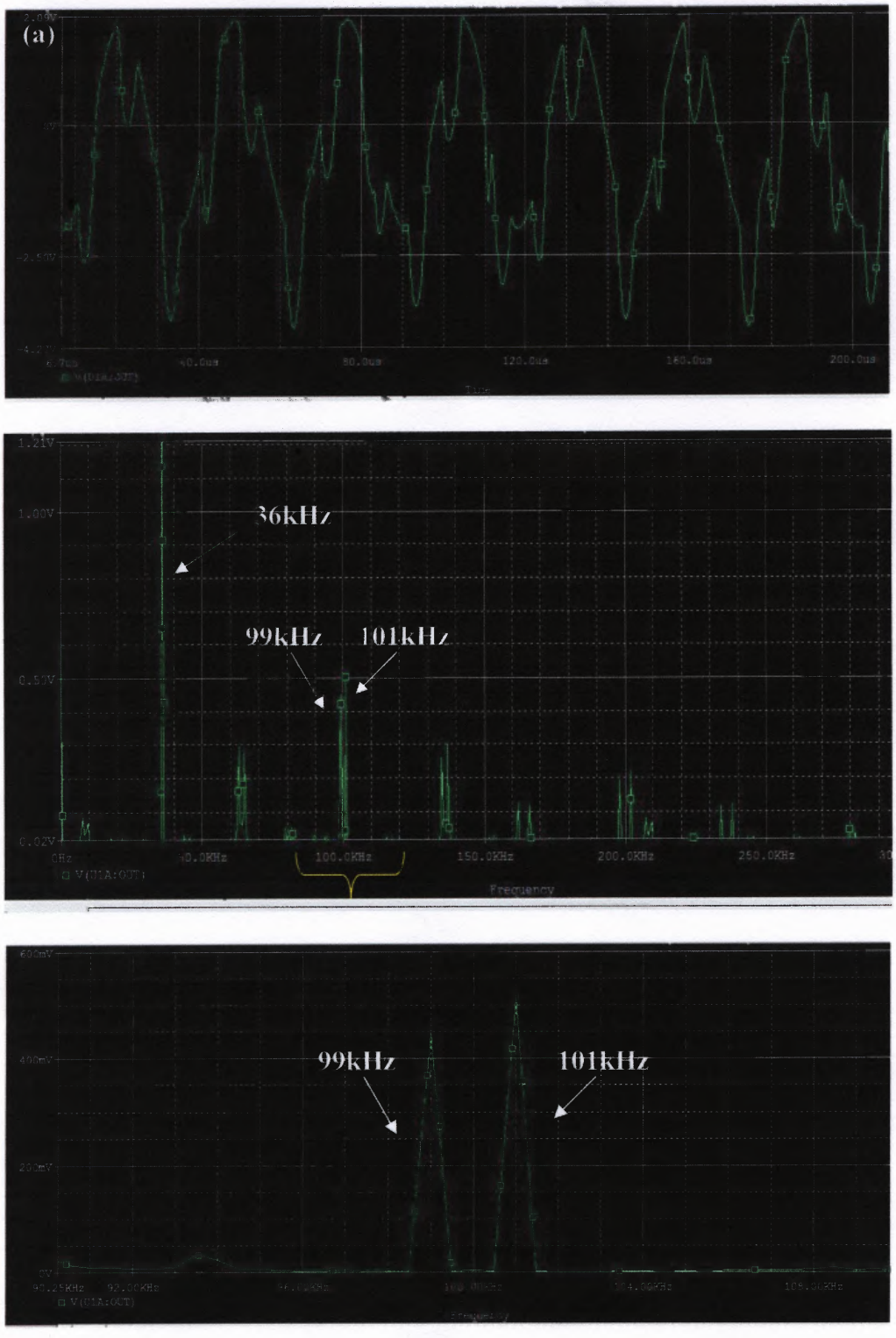

Figure 3.16 Orcad simulation results; (a) Time domain, (b)and(c) Frequency domain.

3.6 Summary

The innovation of this investigation was the introduction of the pseudo-dynamic resonant beam method as a new Coriolis force detecting method in the Coriolis mass flow meters. The dynamic nature of the sensor will permit many new applications. This method has successfully demonstrated a sensitivity of 0.02/g/s. The PD method also has the advantage of linear output. Basically, this parametric linear effect is valid in small Coriolis forces so that this sensor responds linearly as seen in Figure 3.14. However, some fabrication issues remain. For example, the vacuum packaging for high quality factor and the damping effect are critical for resonant devices. These will be the next steps needed to fully realize this PD resonant beam method.

CHAPTER 4

MICROFABRICATION

4.1 Introduction

Microfabrication technology evolved with the computer industry for over 50 years. Microfabrication has not been limited to one area however, but has been extended to the production of microscale devices related to sensors and actuators. Microfabrication processes based on thin film depositions and wet etching techniques have developed into wafer bonding and dry etching techniques for bulk and sacrificial micromachining. After introducing device design and simulation, microfabrication processs and photomask designs will be created and discussed in this chapter. Micromachining technologies for fabricating the resonant beam sensor device will also be introduced and discussed in detail. Micromachining is a great advance for fabricating sensors, actuators, and microsystems such as lab-on-a-chip and system-on-a-chip devices. Basically, the common micromachining tools available, mainly derived from the mainstream integrated circuit industry, involve adding 2-D layers, etching the 2-D layers, bonding on additional substrates, and etching these substrates. Since microfabrication tools almost all involve successive photolithographic patterning, any 3-D aspects of micromachined devices are due to the patterning of the 2-D layers, the interaction of stacked and patterned 2-D layers, and the selective etching of the layers or the substrate [24]. The final material properties can depend on the detailed process and sequencing in applying the proper materials as the device is produced. To design a fabrication process, precise process modeling is required accompanied by a traveler or set of notes that details every step. This modeling is

achieved by using COVENTORWARE simulation software which is specialized for microfabrication or micromachining, especially for MEMS. COVENTORWARE helps every step in the process of matching mask design and real fabrication. In this chapter, the device design, detailed fabrication steps, and techniques used in fabrication are shown. The rest of chapter will discuss technologies such as dry etching and wafer bonding, which are particular to a microfluidic device. There are three main parts in this Coriolis mass flow sensor: a cover glass for the electrostatic actuator; a tube loop microchannel structure to channel the microfluid flow and the Coriolis operation; and a glass substrate for hermetic sealing which can be produced by anodic bonding. As shown in Figure 4.1(b), the cover glass and glass substrate require hermetic sealing with localized aluminum electrodes. The silicon tube microchannel requires some kind of adhesive bonding such as fusion bonding to prevent leakage from the tube channel. COVENTORWARE is capable of analyzing a MEMS device from the mask layout level, including the basic processes of building the microstructure, up to the simulation of the electromechanical behavior of the finished product using finite element techniques. Process simulation typically starts with two-dimensional layout geometry using user-defined process information inputted in the form of intended process and material information. The software then converts this into a three dimensional geometry. A three dimension virtual model for a silicon base tube microchannel part is shown in Figure 4.2 as simulated by COVENTOR MEMS simulation software. Virtually, layer by layer, this picture shows how the design of the device and confirms that the fabrication order is correct.

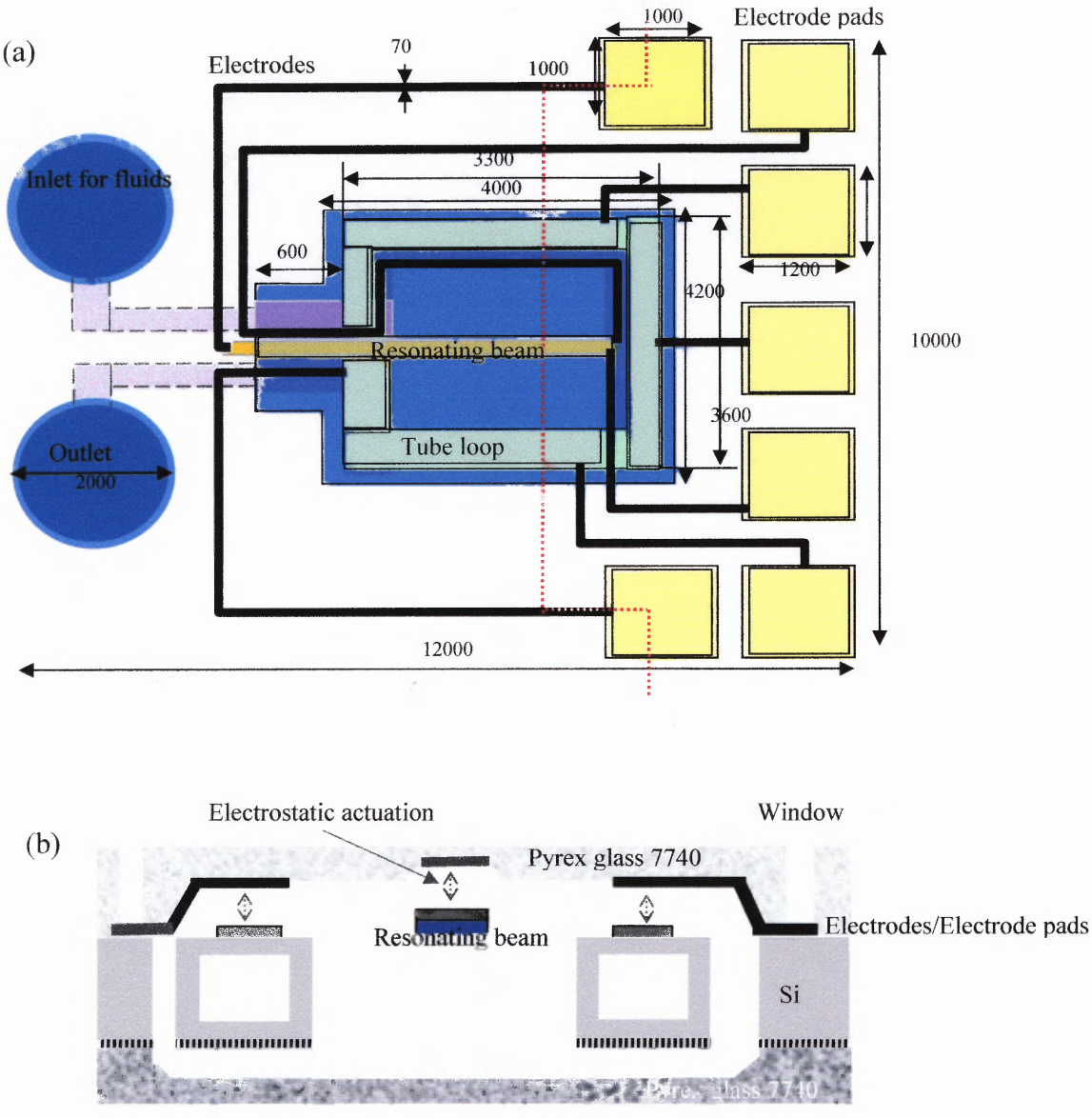

Figure 4.1 Schematic device design for mass flow meter; (a) top view of design (b) side view of device design aligned with the dotted line in (a).

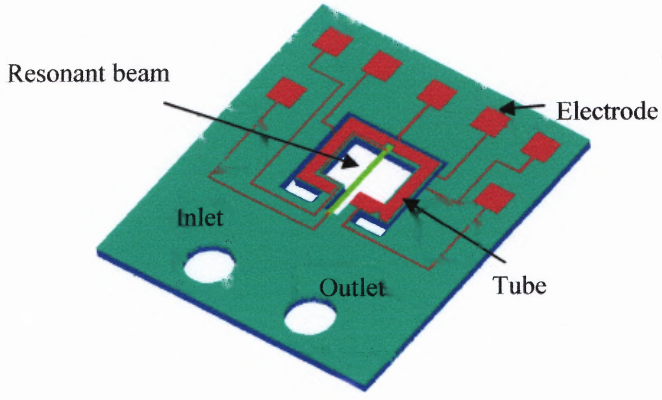

Figure 4.2 Three dimension virtual model for the silicon base tube microchannel part shown in Coventor software.

4.2 Microfabrication for this MEMS Device

4.2.1 Overview

Micromachining for MEMS devices is the newest evolution of microfabrication. It considers the more mechanical structures and characteristics rather than the electrical properties of devices. The detailed process methodology is essential to build up the exact structure which one wants. Thus, the process flow is introduced in this Section 4.2, with the design considerations and the necessary main technologies such as dry etching, wafer bonding, and glass machining.

4.2.2 Materials for Micromachining

Since silicon is the fabrication material for most integrated circuits, silicon and its processing techniques have become the required material and processes for most micromechanical structures. Silicon has outstanding mechanical properties with Young's modulus and hardness and single crystal silicon shows three times the yield strength of steel and has no creep or plastic deformation phase [24]. Silicon (Si) has advantages for a micromachining technology. SiO_2, which can be naturally oxidized to within a few nanometers of a desired size, is very appropriate for photolithographic masking and reactive ion etching, has great thermal stability, and has good adhesion for wafer bonding and adequately low electronic defect densities. Silicon is commonly used in the MEMS field. In Table 4.1, silicon is compared with alternative materials for the main substrate. Single-crystal silicon has been used as a main substrate for this device.

Another main substrate is Corning glass 7740, which is widely used in the micromachining field. It can be useful for hermetic sealing by anodic bonding. Its weakness is that it is hard to do wet-etching the glass wafer (~20nm/min).

Table 4.1 Mechanical Properties of Silicon and Other Materials [24]

Materials	Yield Strength (10^9 N/m^2)	Young's Modulus (GPa)	Density (g/cm^3)	Thermal Conductivity (W/cm·K)	Thermal Expansion Coefficient (10^6/K)
Si	7	190	2.3	1.57	2.33
SiC	21	700	3.2	3.5	3.3
Diamond	53	1035	3.5	20	1
SiO_2	8.4	73	2.5	0.014	0.55
Si_3N_4	14	385	3.1	0.19	0.8
Al	0.17	70	2.7	2.36	25

4.2.3 Mask Generation

Microfabricated MEMS devices are shaped by patterns in the various layers created by wafer-level process steps. There are two basic methods to generate masks; optical lithography and e-beam lithography [24]. Both start with fused silica plates (amorphous quartz 5" square plates are typical) that have been coated with thin chromium layers, and then with a photoresist. The actual mask fabrication is much like a step-to-repeat lithography process: a rectangle is exposed, the wafer is repositioned, and another rectangle is exposed [24]. Based on the virtual fabrication process flow, masks can be designed with the drawing tool of from Mentor Graphics since the design tool in COVENTOR MEMS simulation software is less accurate. The GDS II file, made by Mentor Graphics, can be converted to another graphic file format such as Postscript (.ps) or AutoCAD drawing files (.dxf, .dwg) layer by layer in LINKCAD software. The final graphic file can be printed out with a high-resolution printer or can be sent directly to a mask pattern generator. Figure 4.3, shows wafer scale drawing (a) and unit cell scaling (b) as postscript-type pictures. In Figure 4.3(b), the overlapped area shows that two electrodes on the silicon tube and the cover glass become physically bonded when it is anodically bonded.

The photoresist is then developed and baked, and the chromium etched into the correct pattern. The photoresist is removed, leaving a chromium-on-quartz mask. Emulsion masks are cheaper to make, but are more susceptible to scratching and surface damage than chrome masks. Since the feature size is larger than 50um in this design, an alternate low-cost mask making method can be used. The Mentor graphics drawing is printed out to high-resolution transparent film with a 20um minimum feature size. A

photoresist-covered chromium mask to which design-patterned film is attached, is then exposed to UV for 55 sec., and then developed in MF-319 for 2 min., and rinsed in DI water for 2 min. After drying or hard baking for 5 min, the chromium layer is etched for 5 min, and rinsed in DI water for 2 min. Finally, after drying, it becomes the true mask for photolithography. The sample drawings in transparent files are shown in Figure 4.4.

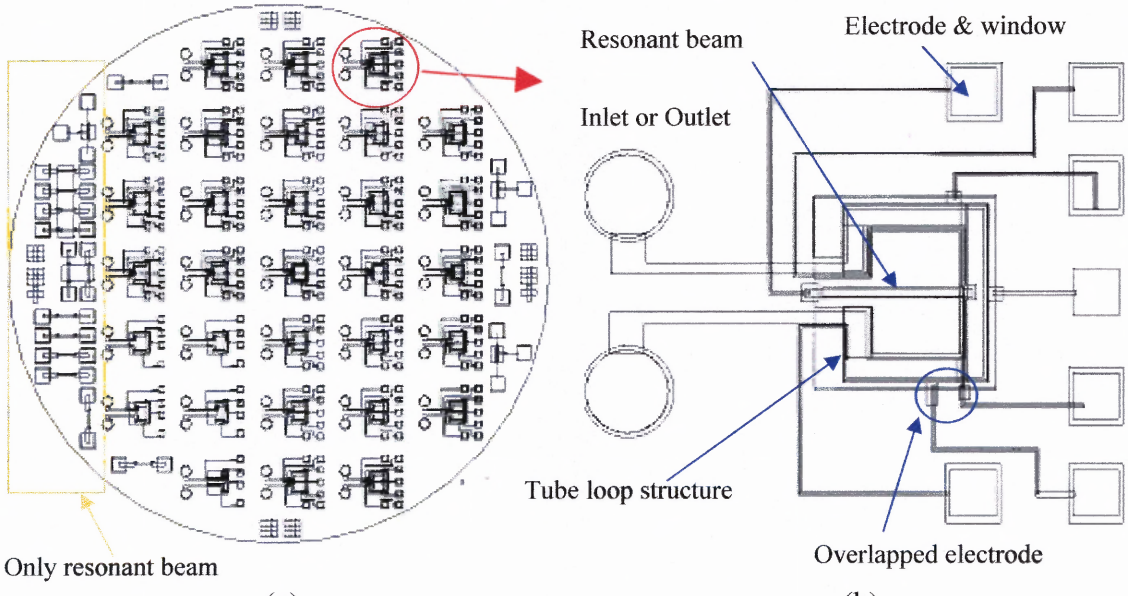

Figure 4.3 Mask design in Mentor graphics software; (a) 4" wafer scale drawing, (b) unit cell scale drawing

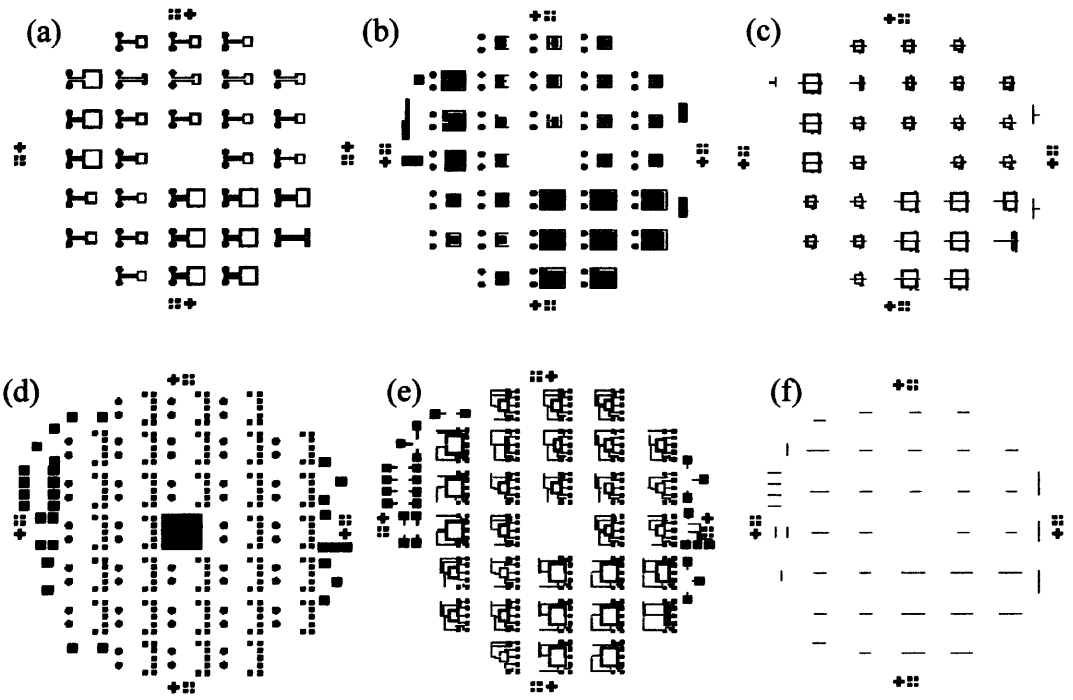

Figure 4.4 4" scale mask designs in high-resolution transparent film; (a) loop inside, (b) loop outside, (c) electrode on glass substrate, (d) window, (e) electrode on silicon, (f) resonant beam.

4.2.4 Process Design and Traveler

Designing a microfabrication process for MEMS devices means numerous trials and errors before realizing the preferred shape and arriving at a reasonable process. The process sequence of steps is very important in order to prevent fabrication errors. Table 4.2 lists a number of critical process-design issues that should be considered. Processes that require a vacuum and an suspended tube channel structure make the process order more complicated. For example, when using high vacuum-required deposition processes such as sputtering and evaporation, thin film-covered cavities and areas in DRIE will be cracked or opened due to the pressure difference. The fabrication order of wafer bonding

to make tube structures should be carefully considered since vacuum-required steps may not be used after wafer bonding has been completed. And, when Al is used as an electrode material, the next photolithography steps should be carefully chosen since Al is soluble in developer (MF-319) after a few minutes. There are many other considerations which should be carefully kept in mind at each step of the fabrication process. The traveler is a set of notes that describe every fabrication process and should be written before fabrication is begun. To track the fabrication, the virtual process simulation should be converted into a traveler such as the traveler for DRIE as shown in Table 4.3.

Table 4.2 Process Design Issues

Thermal constraints	Backside processing
Materials property control	Institutional constraints
Mechanical stability	System partitioning
Process accuracy	Packaging
Alignment features	Process partitioning
Wafer architecture	Cleaning requirements
Die separation Device geometry	Cross-contamination constraints

Source: Stephen Senturia, Microsystem design, 2000, Kluwer academic publishers

Table 4.3 A Sample of Traveler for DRIE

	Date	Wafers	Operator	Comments
Starting materials: 4" p-type (100) Si Wafer ρ=1~10Ω.cm Thickness: 380μm Double side polished				
1. P-clean 5:1 H_2SO_4:H_2O_2 110°C, 10 min				
2. Rinse HOT DI 10 min				
3. Rinse COLD DI 5 min				
4. Spin dry				
5. Apply thick Photoresist ~7um Shipley 3813, 3000rpm,30sec				Caution! Keep clean the FRONTSIDE
6. Soft bake:110°C, 100sec Cool on cold plate for 60 sec 18°C				
7. Align and expose Mask: (a) inloop Time: 35 seconds				
8. Develop Apply developer AZ 300K Wait for 2min 30 sec Spin & Rinse with DI				
9. Hard bake 115°C for 60 sec Cool on cold plate for 60 sec 18°C				
10. Si dry Etching DRIE;250μm				
11. Inspect				
12. Strip PR M-pyrol, 95°C 10 min PRIMARY 10 min SECONDARY				Optional method 1 isopropanol 2 Acetone
13. Rinse COLD DI 10 min				
14. Spin dry				
15. Inspect				

4.2.5 Fabrication Process Flow

The fabrication process is explained in detail in this Section. In Figure 4.5, the total process consists of three main parts; producing the tube-shape structure, glass machining, and attaching these together.

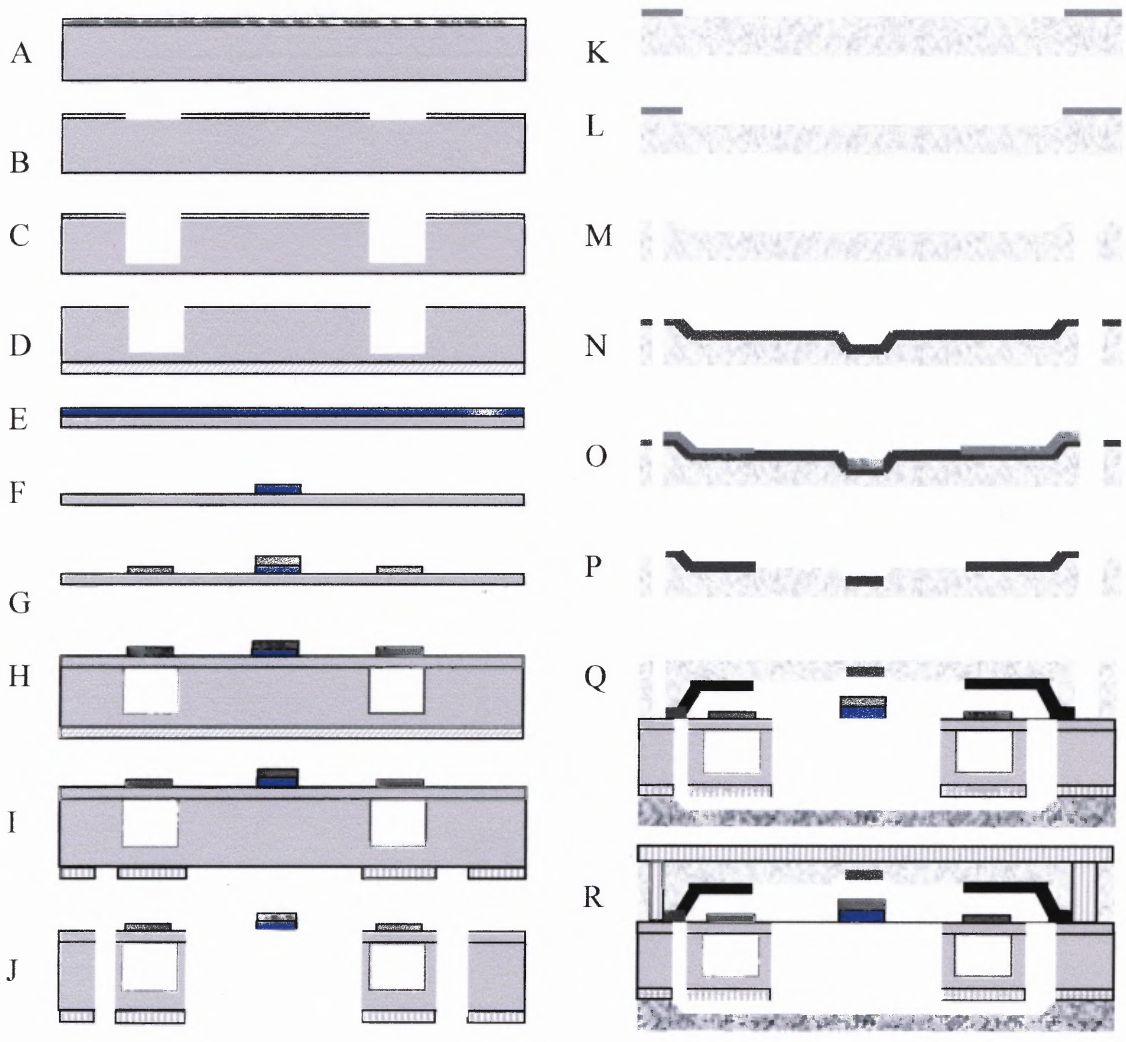

Figure 4.5 Total process flow for a micro machined Coriolis flow meter.

In more detail, it comprises using DRIE for the cavity inside in A-D, resonant beam and electrode patterning on ultra thin film to make the top layer of the tube in E-G, which will be attached to the cavity-patterned silicon wafer in H. Then, back side aligning and DRIE are used to create the suspended tube structure in I-J, followed by glass HF shallow cavity wet etching and holes drilling in K-P, anodic bonding to attach the glass to the silicon wafer in Q, and finally silicon dioxide deposition to create a hermetic seal.

Preliminarily, it must be clear that cleaning is introduced and is an important step throughout the fabrication. The cleaning procedure for normal bare silicon is as follows: NMP (N-methyl pyrrolidone) first bath at 95°C for 10 min, NMP second bath at 95°C for 10 min, DI (de-ionized) water at 20°C for 10min, P (Piranha)-clean at 110°C for 10min, Hot DI water at 80°C for 10min, Cold DI water at 20°C for 10min. This cleaning process is applied not only to normal silicon, but also to the wafers on which the photoresist used. For hydrophilic fusion bonding, there is one more step after normal silicon cleaning; BOE (100:1) at 20°C for 1min, Cold DI water at 20°C for 10min.

A. After cleaning the bare silicon wafer, the silicon wafer is baked for 30sec for good adhesion with photoresist and thick photoresist (AZ9260) is deposited at 3000rpm for 30sec. The wafer is pre-baked for 100sec at 110°C. In order to prevent photoresist failure, the wafer can be oxidized before photolithography.

B. After cooling down for 1min, the wafer is exposed to ultraviolet rays with mask (a) in Figure 4.6 for 35sec and is hard baked for 1min. It is developed for 2min 30sec in AZ 300K developer. And then, the wafer is post-baked for 15 min before DRIE.

C. Deep reactive ion etching (DRIE) is achieved using the Bosch process. Detailed conditions will be given in Section 4.3.

D. Acetone and isopropanol are used to remove the rest of photoresist. Normal cleaning steps are following. The wafer is thermally oxidized in 1hour at 1100°C and a single side oxide layer is stripped in BOE solution.

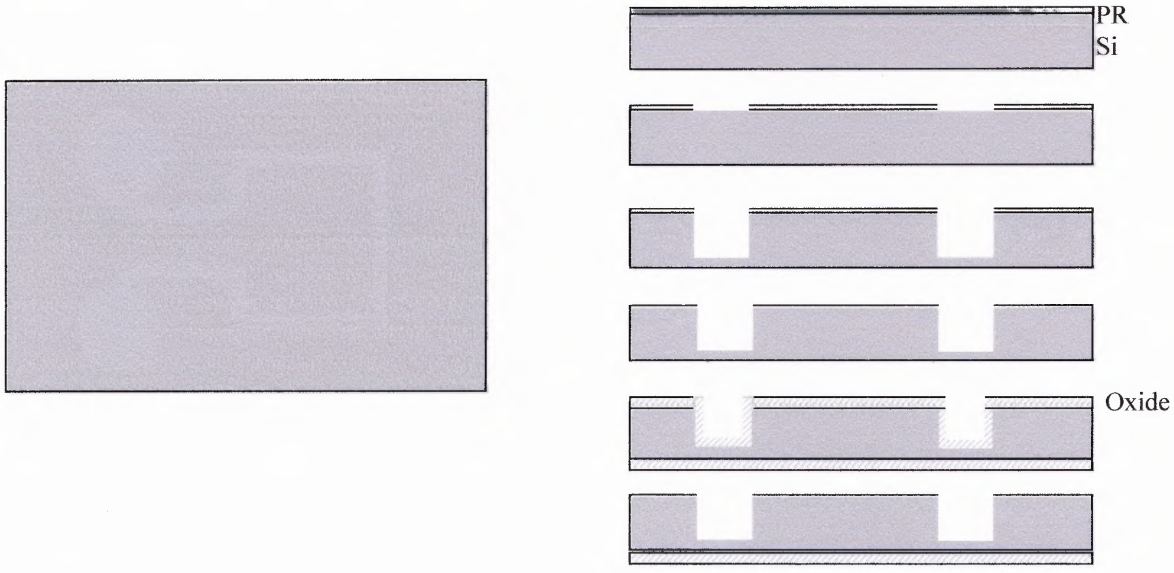

Figure 4.6 Deep reactive ion etching for the channel inside in steps A-D.

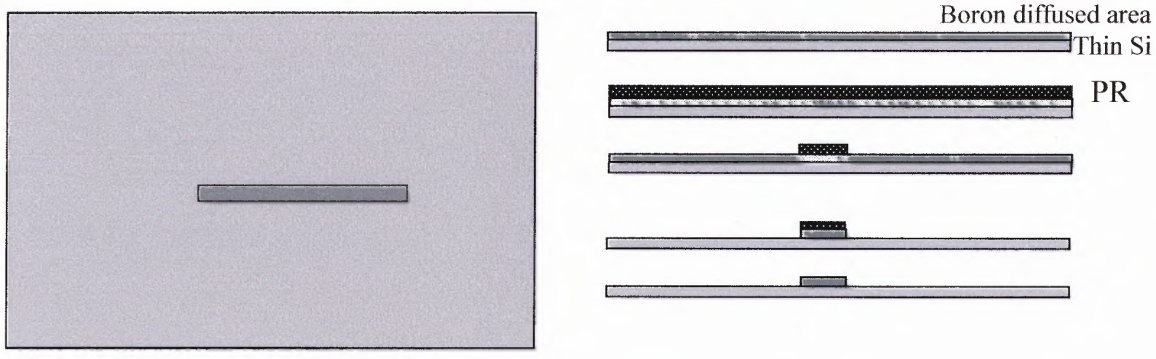

Figure 4.7 Deep reactive ion etching for resonant beam in steps E, F.

E. To get a resonant beam to be a piezoresistor and function as a strain gauge, an ultra thin 100um wafer and SOI wafer(2/0.5/100um) is p-type heavily doped at a shallow layer (100nm) in Ion implantation under the condition of 5e+13eV.

F. After being p-type heavily doped, these thin wafers are deposited with AZ9620 thick photoresist under the following conditions; spinning 2000rpm 60sec, exposure 20sec, developing in AZ 400K in 4min, rinsing with cold DI water, hard bake for 10min. The photoresist thickness is about 1.8um for which 12:1 selectivity is assumed. DRIE is applied to the 2um (SOI wafer) and 10um (ultra thin wafer) following the recipe in the Table. Figure 4.8(d) shows images of the released resonant beam in Figure 4.8(a, b, c) and the vertical profile on silicon wafer in DEKTEK surface thickness measurement. The pictures show the porous patterned silicon with the thickness of 7.4um. In this sample it appears that the photoresist was not properly working, which means the SF_6 etching passed through the photoresist and etched unwanted areas.

G. After stripping the photoresist with acetone and isopropanol, the wafer is on p-clean and aluminum is sputtered to 200nm. For electrode patterning, these thin wafers are deposited with S3813 thin photoresist under the conditions; spinning 2000rpm 60sec, exposure 20sec, developing in MF-319 for 3min, rinsing with cold DI water. The MF-319 developing solution attacks aluminum if the exposed photoresist is overdeveloped. After hard baking for 20 min, the aluminum is etched in an aluminum etching bath at 43°C for 1min.

H. After stripping photoresist with acetone and isopropanol, the wafer is on p-clean and on 100:1 BOE cleaning in 1min and rinse in 10min for making a hydrophilic surface in Figure 4.10. Prebonding is under 1000N force for 30sec with an EV501 bonding machine and these bonded wafers are annealed at 1100°C in 1hour.

I. Backside patterning: from step D, the backside of silicon wafer still has an oxidized surface. After fusion bonding, AZ9260 thick photoresist is deposited on the backside of the silicon wafer with the spinning condition of 1500rpm for 60sec and the wafer is soft-baked at 1100°C in 80sec, then aligned with the IR camera, and exposed for 57sec, developed with AZ400K developer in 35min, rinsed in cold DI water, and hard baked in 10min at 120°C. The oxide layer through photoresist window is etched in 3min and the wafer is rinsed in cold DI water for 5min. It is hard baked again for 5min to be ready to etch through bonded wafer with DRIE. The thickness of the photoresist is about 50um.

J. Backside DRIE: total etching thickness is about 480um (380 silicon and 100um thin wafer) in Figure 4.11. AZ9260 has better selectivity than Shiply220. Photoresist on the oxide layer is patterned with thick photoresist (AZ9260) at 3000rpm for 30sec, pre-baked in 100sec at 110°C, developed in AZ400K, 10min, and post-baked in 10~20min at 110°C.

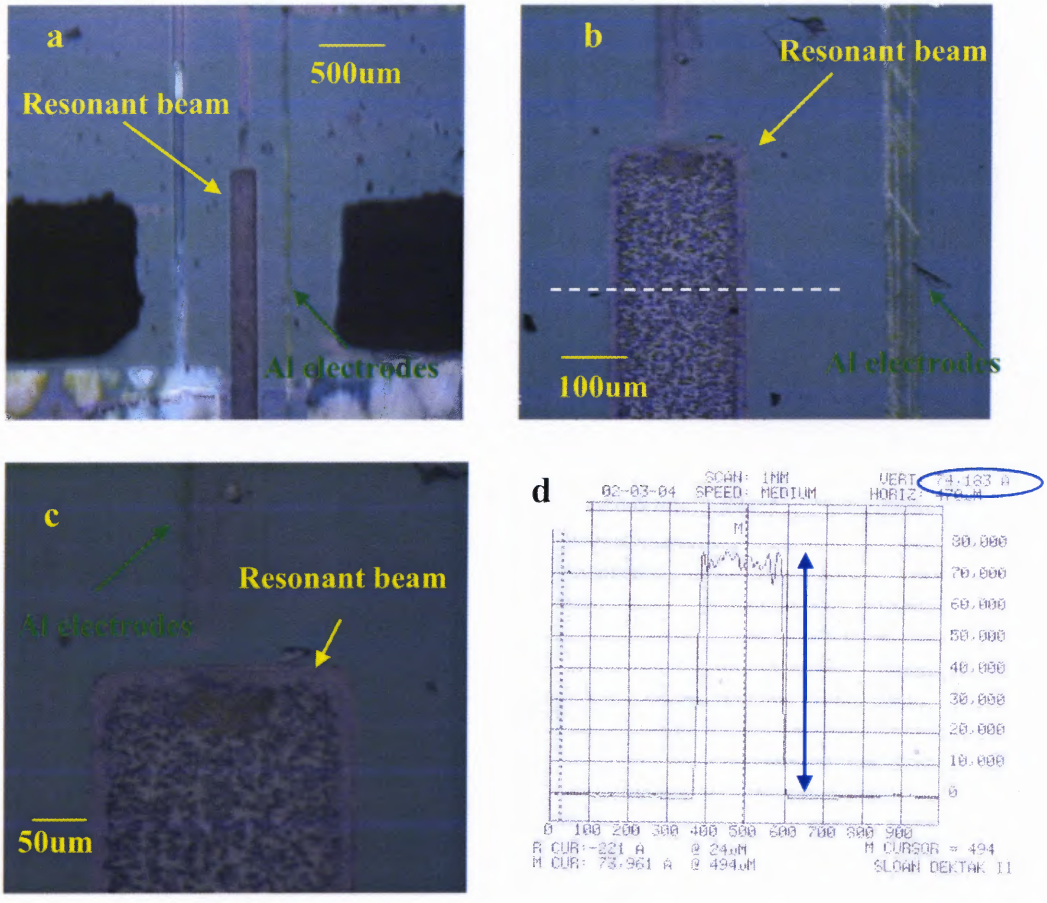

Figure 4.8 The microscopic pictures of the resonant beam; (a) x5, (b) x10, (c) x20, (d) Dektek surface thickness measurement of resonant beam along with the dash line in (b) after 7.4um DRIE of 100um ultra thin Si wafer.

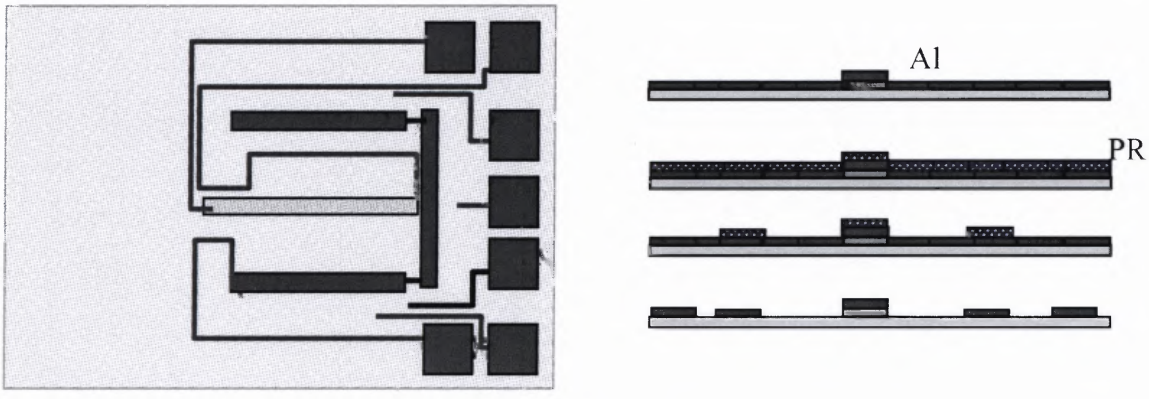

Figure 4.9 Aluminum electrodes patterning with sputtering in step G.

K. Au/Cr is sputtered to a thickness of 500nm/50nm. Chromium is used as a buffer layer between the gold and the glass substrate since chromium has good adhesion between glass and gold, as shown in Figure 4.12.

L. The 5um deep shallow layer in glass wafer is etched. The etching rate is slower than oxide etching. This is because sodium ions interrupt the HF etching to the silicon dioxide.

M. After the wafers have bonded, the holes are drilled – using ultrasonic drilling – to make contact through the glass to the electrodes on the silicon wafer.

N. Aluminum is sputtered to a 200nm thickness as electrodes in Figure 4.13.

O. The aluminum-sputtered glass wafer is patterned with S1813 under the conditions of 1500 rpm spinning 60sec, soft bake in 80sec at 110°C, 19sec exposure, post bake in 80sec, developing in 2min. Because the glass wafer has holes, after it is spun, the photoresist on the glass wafer is not smooth. And it must be noted that holes drilled into the glass wafer required a dummy wafer to support the glass wafer from vacuum chuck. MF-319 developer also etches aluminum layer. So, if the exposed S1813 is over-developed, the MF-319 will etch the aluminum.

P. The aluminum is etched away in aluminum etchant in 1min at 43°C. According to the thickness of the substrate, the recipe of photolithography may need to vary.

Q. The glass wafer and the silicon wafer are anodic-bonded at 400°C with 1000V voltage and 1000N force, as shown in Figure 4.14. In the circled areas, electrodes on the glass and silicon are bonded physically, under pressure and voltage, during the anodic bonding process.

R. To make a hermetic seal, the device may require the deposition of an oxide layer, as shown in Figure 4.14.

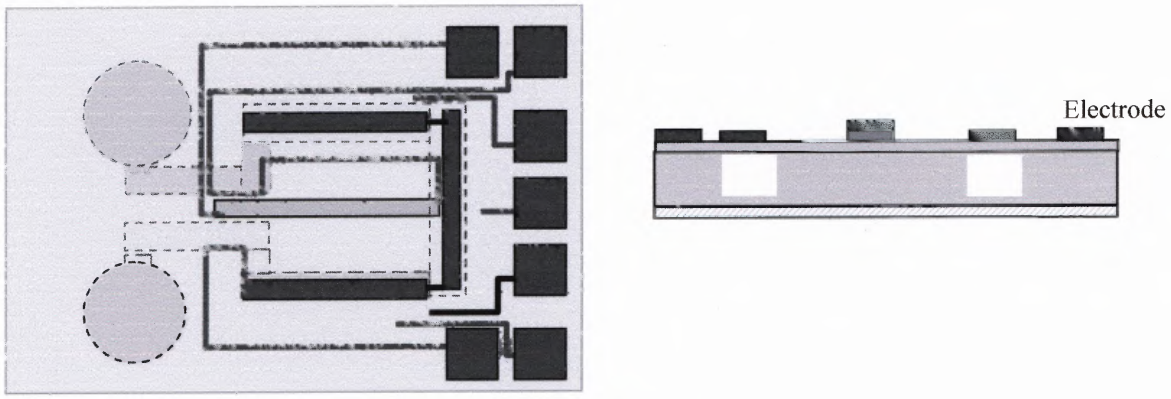

Figure 4.10 Fusion bonding/Photoresist bonding in steps H.

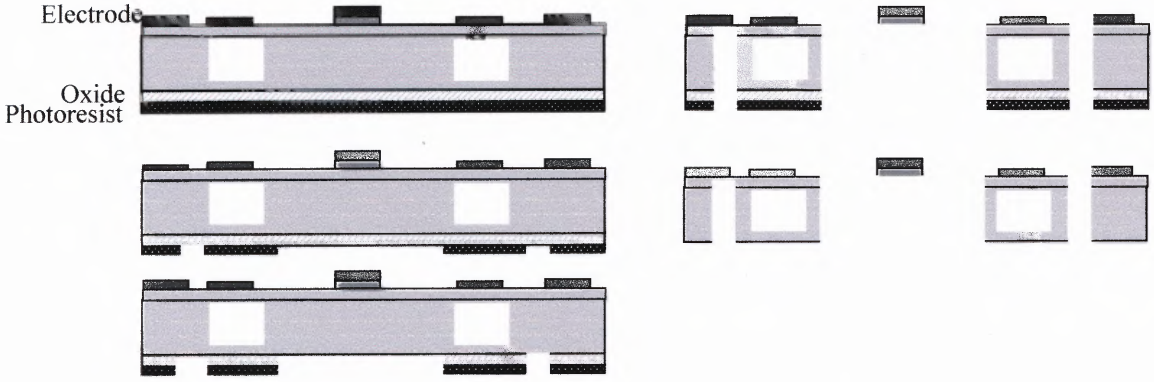

Figure 4.11 Deep reactive ion etching for the back side in step I and J.

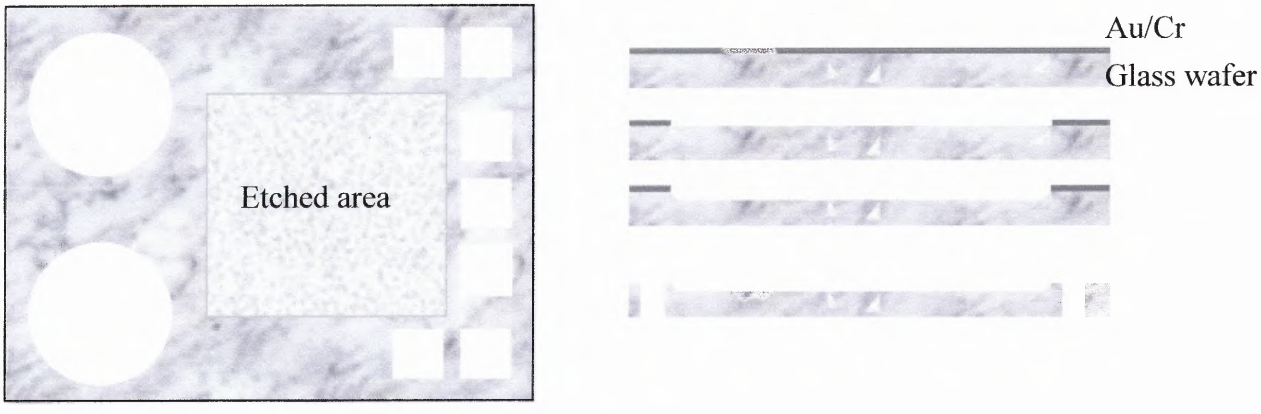

Figure 4.12 BOE wet etching for glass cavity in steps K-M.

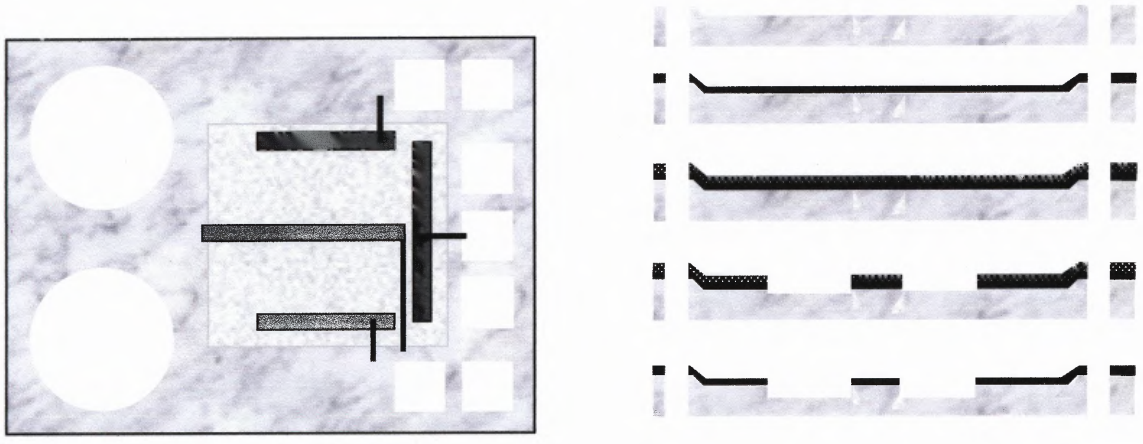

Figure 4.13 Aluminum electrodes patterning in steps N-P.

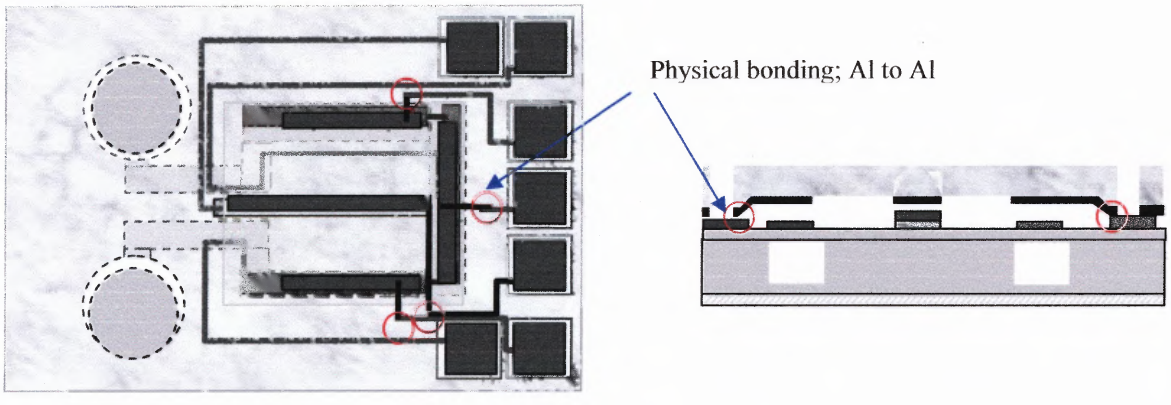

Figure 4.14 Anodic bonding for hermetic sealing in steps Q, R.

4.2.6 Wafer Cleaning

Wet chemical cleaning has been used for years in the cleanroom to remove chemically or physically bonded contaminants from wafer surfaces. However, there are some issues if the process has metal film deposition wafers. Wafer cleaning makes use of highly reactive chemicals that do not attack the corrosion-resistant materials of the wafers themselves but may affect the metal deposition. The wet chemical cleaning step has to be used selectively and carefully after the deposition of metal film on the wafer. The following Sections briefly introduce the common cleaning techniques and specific refinements to manufacture this device.

A. Piranha Cleaning: This term refers to a hot solution of H_2SO_4 and H_2O_2 mixed in any ratio. The most normally used mixture is sulfuric acid ($98\%H_2SO_4$): hydroperoxide ($30\%H_2O_2$) 3:7. This solution has been dubbed "piranha clean" because it attacks organic materials so insistently. Wafers are soaked in piranha at 100-130°C for about 10min. The wafers are vigorously rinsed in de-ionized (DI) water at 100°C and 18-23°C respectively for 10min. Piranha is used for 10min to clean organic and metallic contaminants from wafers. Piranha strips photoresist and other organics by oxidizing them, and removes metals by forming composites that stay in the solution, but it does not have any effect on silicon dioxide and silicon nitride and has the smallest of effects on bare silicon by forming a thin layer of hydrous silicon oxide [42, 43].

B. N-methyl Pyrrolidone (NMP): The aggressive acids and alkali solutions used in the RCA clean can be no longer be used after metals are deposited on the wafer. Instead, cleaning ought to be done with less reactive solvents. The general solvent used for such cleaning is NMP [43].

C. Acetone and Isopropanol: Acetone is used to strip photoresist, destroying the structure of the photoresist and making it soluble. While acetone easily strips the photoresist, its effectiveness depends on the processing which the photoresist has already gone through. Heating the photoresist by a few tens of degrees above 120degrees, during hard-baking or another process step, will make it significantly harder to dissolve. Some plasma processing gives rise to a similar effect [42]. After the acetone application, isopropanol is used to dissolve the acetone and to keep the residues of acetone reactant from the wafer.

D. Oxygen Plasma Photoresist Etches: This oxygen plasma is used to strip photoresist. The plasma-processing step is used for removing undesired thin layers of freshly developed photoresist. Oxygen atoms "burn" the organic photoresist, forming mostly H_2O, CO_2, and CO [24].

4.2.7 Photolithography

The photolithography process includes the use of an optical image and a photosensitive film to create a pattern on a substrate. In microsystems, photolithography is used to place patterns for masks for cavity etching in bulk micromanufacturing or for thin film deposition and etching of sacrificial layers in surface micromachining. Photoresist has been involved in dry etching or used by itself such as SU-8 negative photoresist used in MEMS [24]. In dry etching using the plasma, photoresist selectivity is a critical point since the photoresist also is attacked by the plasma. In Figure 4.13, thick photoresist is patterned by photolithography for deep DRIE in (a) and a photoresist thickness profile of a 400um wide channel is shown in (b). The tolerance of the photoresist shape at the edge of the cavity defines the tolerance of the cavity-wall shape and angle.

A. Materials for Photoresist: There are two type of photoresist; thin photoresist (S3813, S1813), thick photoresist (S220-7, AZ9260, SU-8). Thin photoresist is used for thin film deposition and wet etching at the several micron scale. Thick photoresist is used for building up the structure for deep dry etching (S220-7, AZ9260) or molding the structure (SU-8). The recipes for photolithography are detailed for those photoresist materials in Table 3.4. In using S220-7, the photoresist reaction with plasma is sensitive to the photoresist's hardness. In other words, harder photoresist is to plasma. These photoresists may lose their plasma-resist property even after they are re-heated by hot plates since the thick photoresist inside itself may not be hard enough to resist DRIE plasma after a short hard-bake. Thus, the photoresist should be hard-baked for a long enough time. For example, the hard-bake should be at least 30min for a 10um thick coating.

B. Photoresist Removal: Photoresist stripping techniques include using oxidizing-type (inorganic) strippers, organic strippers, and dry-type stripping. Oxidizing strippers can only be employed to remove resist from non-metallized wafers. Organic strippers carry out resist removal by breaking up the structure of the resist layer. Organic strippers based on n-methyl-pyrrolidone are available. Dry etching of resist is best achieved with plasma resist-stripping tools, with oxygen as the process gas. In this project, O_2 flow rate in the Bosch DRIE process was 70 sccm in 10min [43]. However,

oxygen plasma cleaning is not effective enough to remove contaminants such as the plasma–hardened photoresist after long-time use on the wafer.

C. Double-Sided Lithography: Many MEMS devices require patterning on both sides of a wafer. To realize the necessary positional alignment between the front and back side, special tooling is required. In this effort, there are two options to visualize the back side image from the front side: an IR camera with a normal light bulb and a Normal aligner with an IR light. The back-side mask was aligned to marks on the tool, the technician then places the wafer over this mask, and aligns the wafer to the tool using alignment features on the front and using one of the above methods to see the back side. The wafer and the back-side mask are then aligned to each other within alignment tolerances.

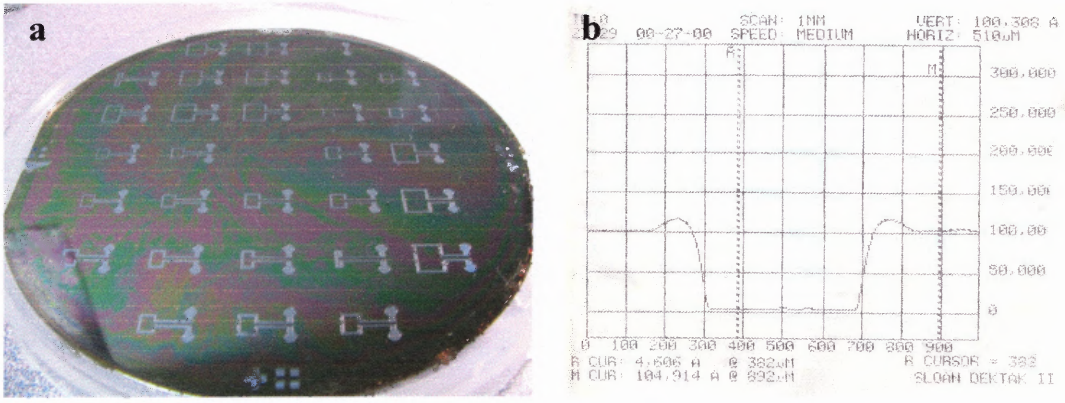

Figure 4.15 (a) Shipley 220 thick photoresist (PR) patterned 4" silicon wafer, (b) Dektek measurement of 10um thick photoresist for 250um DRIE.

Table 4.4 The Properties of Different Photoresist Used

Materials	S3813(thin)	S220-7(thick)	AZ9260(thick)
Spin rate/time	2000/60	3000rpm / 30sec	
Prebake temp./time	110/60	110C/100sec	110/80
Expose time	21sec	35sec	49sec
Developing materials	MF-319	MF-319	AZ400K
Developing time	4min	2min 30sec	5min
Postbake temp./time	10min	15min	10min
Film thickness	1.8um	7.7um	8.7um
Purpose	Resonant beam Al patterning	Deep cavity	Deep cavity

4.3 Deep Reactive Ion Etching (DRIE)

An essential part of the fabrication of this device was the Deep Reactive Ion Etching (DRIE) process. This technique involves repeated exposure of a photoresist-masked silicon wafer to an etchant (usually SF_6) plasma in alternation with a passivant (usually C_4F_8) plasma. So the etching process cycles between etching and deposition steps several times to achieve a deep etching with a quite vertical profile. This technique can achieve aspect ratios of up to 20:1 (sidewall angles 90+/-2degree), with photoresist selectivities of 10:1, silicon dioxide selectivities of 120 to 200:1, and etch rates 5um/min [24]. The etch rate, profile and selectivity to the mask are controlled by adjusting the efficiency of the etching and passivation steps or the time ratio of the two steps. After substrate cleaning (piranha cleaning) and photolithography with thick photoresist (AZ 9260), DRIE began with the following recipe in Table 4.5. It must be pointed out that DRIE is very sensitive to chamber pressure, temperature, and etching/deposition time ratios.

Elevated temperature in the chamber affects the working plasma quite seriously. Before starting, it should be carefully calibrated and allowance must be made an increase chamber temperature due to prolonged continuous usage. Regarding chamber pressure and temperature, it is important to note that normally, etching steps have a higher pressure than deposition steps. Also, the radio frequency power of the etching steps is higher due to the etching mechanism. In Figure 3.15, the pictures show a 380um thick silicon wafer etched to 250um by the process in Figure 3.5 A-D with the recipe #1 from Table 4.5. Figure 4.18 shows a 2D image and x-y etching profile in Veeco optical profilometer Note that the bottom side roundness is quite large due to the loading effect and it being the edge of the wafer.

Figure 4.16 The deep reactive ion etching machine used in this study.

Table 4.5 The Recipes of DRIE Used

	Steps/loop	Temp	Pressure (mTorr)	Flow rate (sccm)	RF1 (W)	RF2 (W)	O_2 (sccm)	Time (sec)	Etching rate (um/min)	Angle	Note
1	Deposition	18	16	40	600	2	7	4	5	-2°	Good
	Etching		20	104	750	14	7	8			
2	Deposition	25	11	40	600	2	7	14	-	-	Failed
	Etching		20	104	750	14	7	11			
3	Deposition	18	10	40	600	2	7	15	-	-	Failed
	Etching		15	104	750	14	7	8			
4	Deposition	18	11	40	600	2	7	14	3	-2°	Good
	Etching		20	104	750	14	7	11			
5	Deposition	18	10	40	600	2	7	11	3	-5°	Large angle
	Etching		16	104	750	14	7	15			

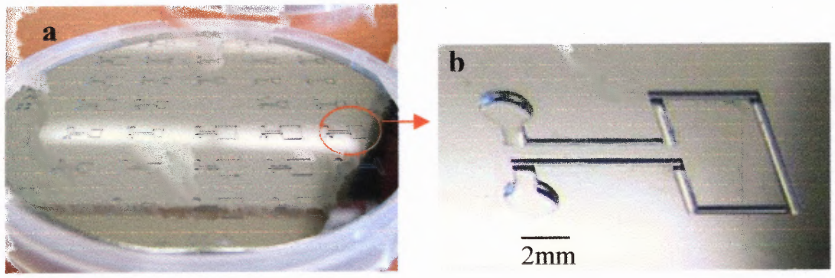

Figure 4.17 250um etched silicon wafer; (a) whole wafer (b) one unit scale.

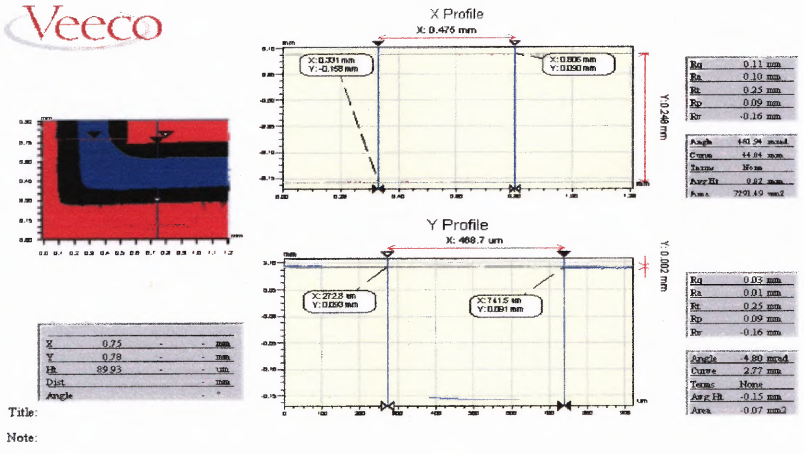

Figure 4.18 2D image and x-y etching profile in Veeco optical profilometer.

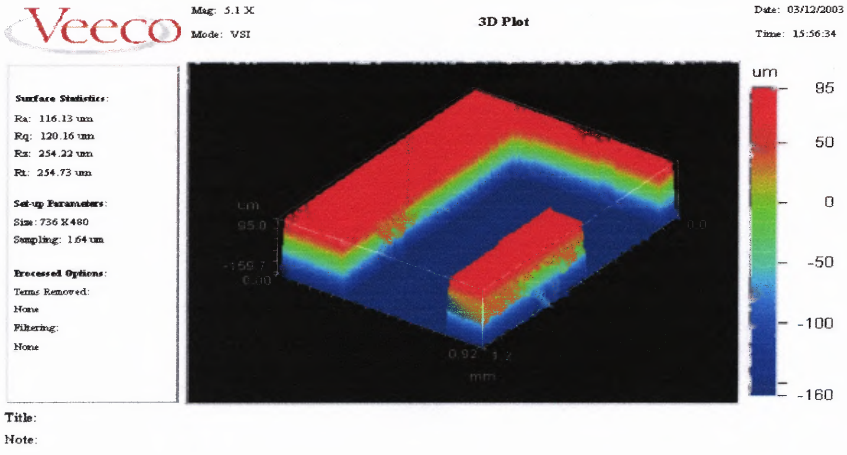

Figure 4.19 3D visualization of etching profile in Veeco optical profilometer.

The picture in Figure 4.18 is based on the recipes #2 and #3 in Table 4.5. It shows the failure of DRIE to take into account that the elevated temperature caused a delayed plasma working time in the etching step and then, with less etching time and low plasma, it was not possible to etch away the residues of C_4F_8 reactant in Figure 4.18(a). In Figure 4.18(b), the photoresist mask was removed earlier than expected due to poor quality photoresist. There are two assumptions that can follow from this: insufficient hard bake time would leave the photoresist without the necessary hardness to resist the ion bombarding and chemical reactions in the etching step; there is a lack of information about Shipley220-7 whose selectivity is lower than expected. Using S220-7, the DRIE was properly accomplished due to the thicker photoresist and a longer hard bake time.

In Figure 4.19, the picture shows the etching vertical profile. Note that recipe #4 has a larger angle than recipe #5 (in Table 4.5) which can be explained simply by controlling etching/deposition time. In Figure 4.20, the picture shows the suspended microchannel after backside DRIE etching. The image is slightly misaligned since it was aligned manually with an IR camera (at 2x). However, this wall of channel could still function as the sealing tube.

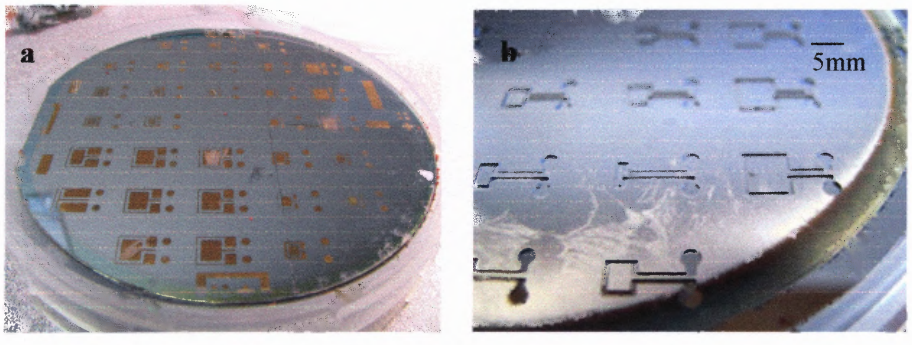

Figure 4.20 (a)DRIE failed 4"silicon wafer; the residues of C_4F_8 reactant remained on the area in which should be etched due to the deposition cycle of C_4F_8 is dominant to the etching cycle of SF_6, (b) overetched silicon wafer.

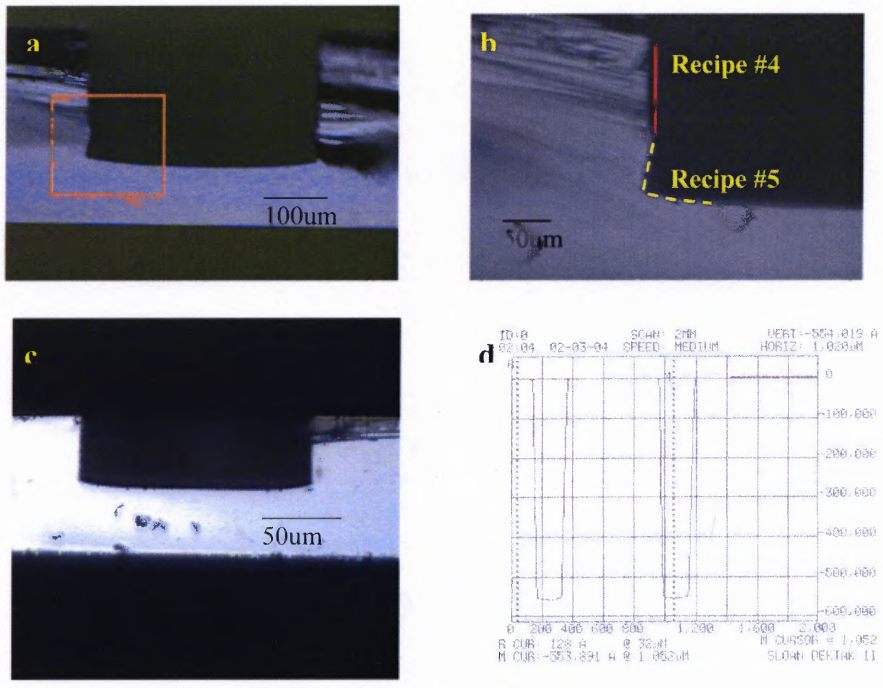

Figure 4.21 The side view of the micro channel structure;(a) 250um deep cavity in 380 um silicon substrate(x10), (b) magnified picture(x20), (c) 100um ultra thin Si 55um DRIE, (d) the picture of Dektek vertical depth measurement .

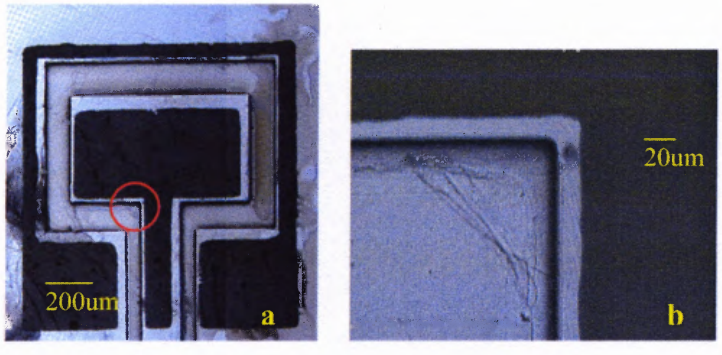

Figure 4.22 The picture of a double side etched silicon wafer; (a) unit device scale, (b) magnified picture.

4.4 Wafer Bonding

Wafer level bonding techniques have been a subject of interest for many years. The most common bonding techniques are fusion bonding, anodic bonding, low temperature glass bonding, eutectic bonding and adhesive bonding. The presented device consists of two wafers of silicon and glass or silicon wafers which are bonded together. A discussion of possible bonding methods follows below.

4.4.1 Fusion Bonding

Silicon wafer level fusion bonding has been identified as a technology applicable in a large variety of MEMS project and structures, for preparing silicon-on-insulator substrates and for demonstrating packaging schemes at the wafer level. Silicon fusion bonding is an attractive approach for fabricating intricate MEMS structures because it eliminates thermal mismatch problems and has the potential to achieve bonds with strengths comparable to that of bulk silicon. Silicon fusion bonding is called "silicon direct bonding." Two highly polished silicon wafers are brought into contact and bonded by a heat treatment. The wafer surfaces are treated to make them hydrophilic, which enhance the strength of the initial bond. Afterwards the wafers are heat treated, at 600 – 1100°C, to bring the bond to full strength. The strength of the bond is as high as that of bulk silicon material. In this bonding, the surface roughness is really the critical criterion because it has only a force of 1000N whereas anodic bonding needs the high electric voltage with the condition of the fusion bonding. For fusion bonding, there are three main parts to the process: wafer cleaning; prebonding; and annealing. The process is listed in Table 4.6. Above all, the cleaning step is very important since fusion bonding does not have any bonding factor other than point tip pressure because it only uses Van

der Waals bonding energy, whereas anodic bonding uses voltage with point tip pressure. In HF solution and cold DI, the surface of the wafer becomes hydrophilic to facilitate hydrogen bonding with another hydroxyl radical of the other hydrophilic wafer [29,30].

In Figure 4.23(a), (b), the images show the annealing effect of fusion bonding. Due to bad surface roughness caused by poor cleaning, some particles caused many small voids between wafers. However, most of the voids were eliminated through annealing at 1100°C for one hour. The reasons that the wafer had some particles of residue were two-fold; poor cleaning already mentioned and hardening of the photoresist by plasma exposure after DRIE. In Figure 4.23(c), (d), a boron diffused silicon wafer has been used in fusion bonding. The wafer is bent from center to edge due to residual stress on the surface from the boron ion implantation, so the wafer edge has poor bonding. Only some of the center area is bonded partly. A single side impurity doping requires compensation for the stress caused by doping.

Table 4.6 Process Steps for Fusion Bonding

1. Cleaning	Piranha 10min
	Hot DI 10min
	Cold DI 10min
	Spin dry
	HF(100:1) solution 1min
	Cold DI 10min
2. Pre-bonding	1000N 30sec
3. Annealing	1hour at 1100°C

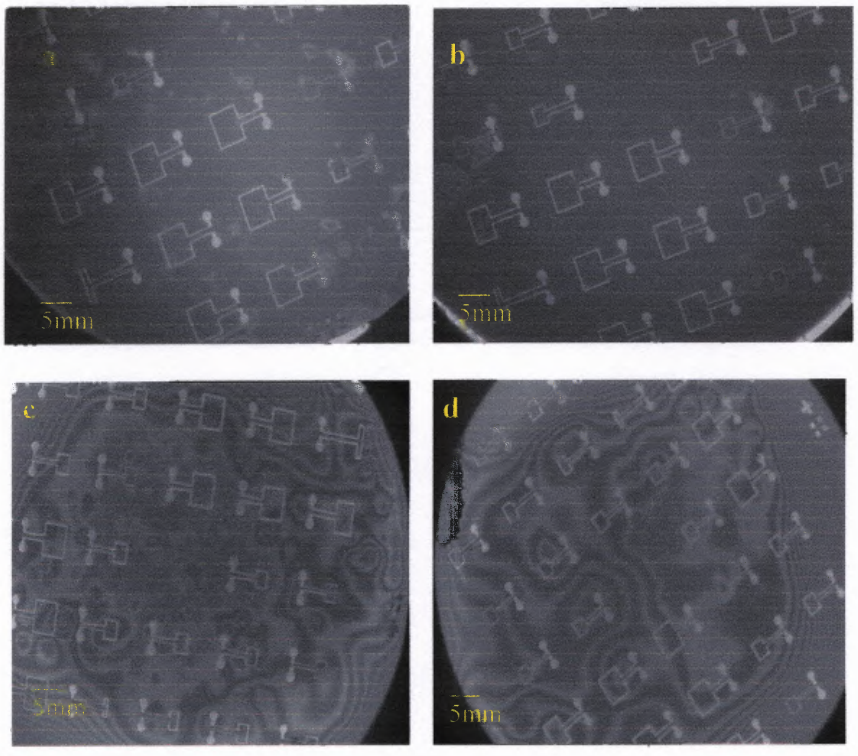

Figure 4.23 The pictures captured by infrared camera; (a) fusion bonding before annealing,(b) after annealing at 1100°C for 1hour, (c) boron doped wafer fusion bonding before annealing(failed), (d) boron doped after annealing at 1100°C for 1hour (failed).

4.4.2 Plasma-Activated Wafer Bonding

Plasma-assisted wafer bonding is a room temperature bonding method, which exhibits very high surface energies, comparable to what can be achieved with annealing steps in the range of 600-800°C using normal wet chemical activation before bonding [24]. The oxygen plasma creates a silica surface. That is, oxygen plasma for fusion bonding is very good for not only cleaning the wafers, but also for generating high surface energy.

4.4.3 Adhesive Bonding – Photoresist (S3813)

A variety of wafer-bonding methods exists in the field of microsystem packaging, compound wafer fabrication and wafer transfer fabrication. Some common methods are anodic bonding [17], surface-activated bonding [24] and eutectic bonding [11]. The disadvantages of these techniques are the need for high temperatures (silicon fusion bonding), high voltage (anodic bonding) or special surface conditions or preparation. Metal compression bonding at room temperature or temperature below 200°C requires high pressure and is therefore not yet suitable for wafer-level bonding. Adhesive wafer bonding uses polymers or inorganic adhesives as intermediate bonding material. The advantages and disadvantages of adhesive bonding methods are listed briefly below [28].

Advantages:

- Low bonding temperature (<200°C possible)
- Applicable for various wafer materials, stress reduction due to the elastic properties of the adhesive
- Compensation for surface nonuniformities by planarisation properties of the intermediate bonding film
- Simple, low cost process steps

Disadvantages:

- No hermetic seals with organic materials
- Limited long-term stability of most adhesives, especially in harsh environments
- Limited temperature stability of many adhesives
- Lower bonding strengths than metal bonds

For adhesive bonding, a polymer film is used as a bonding material. Several different polymers that have been used for adhesive bonding include polyimides, epoxies, and photoresists. In this project S1813 photoresist has been used as the bonding material. The curing conditions were 30min at 110°C. Normal photoresist can be used to rapidly

produce prototypes if the rest of process does not require high temperature conditions above 200°C such as annealing using a furnace.

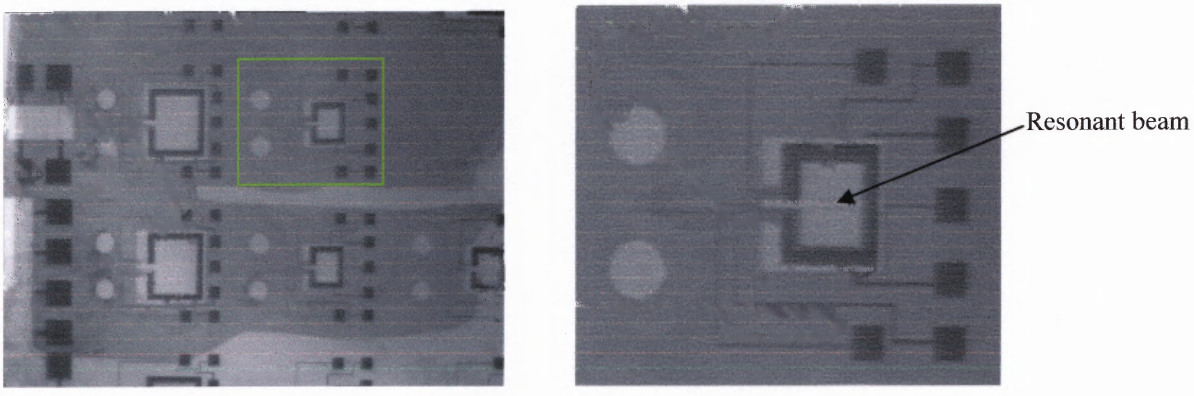

Figure 4.24 The pictures captured by an infrared camera; (a) a part of 4" bonded wafer, (b) one unit scale. The relatively bright area is not a bonded area except for the resonant beam.

4.4.4 Anodic Bonding

Anodic bonding is a low pressure packaging technique which develops the mechanical quality factor because it reduces air damping considerably. This is used to build a hermetic and mechanically solid connection between glass and metal wafers or between glass and semiconductor wafers. The hermetic seal offers the high vacuum environment required for gyroscopes, accelerometers and pressure sensors to improve their performance. A sodium glass such as Corning 7740 is used as the other material of the anodic bonding. When an external electric field is applied at high temperatures, the positive ions in the glass move and create a depletion layer in the glass near the silicon surface. The voltage drop over this depletion layer creates a large electric field that pulls the wafers together. The substrates are heated to a typical temperature of 400-450°C. A typical voltage of 400-1200V is applied to the wafer pair to be bonded. Electrostatic force

and the migration of ions lead to an irreversible chemical bonding at the interface of the individual wafers [5,12] .

In the presented device, the silicon tube is anodically bonded to a metallized and etched Pyrex wafer to form a resonating cantilever U-shape tube. A difficult problem was encountered in the transition from an R&D prototype, running in a laboratory vacuum chamber, to one that was vacuum packaged at the chip level. A Q-value above 1000 was desired to obtain sufficient frequency and hence density resolution with the sensor. For the resonating mass flow meter, a pressure of under 50mTorr is required to obtain a Q-value above 1000. Usual anodic bonding produces cavity pressures in the 100-400Torr range. One solution to this low Q-value problem is the incorporation of a getter to absorb the trapped and desorbed gases left in the microcavity [11, 34].

4.5 Glass Micromachining

Microfabrication of Pyrex glass is important in the field of MEMS because it can be used in anodic bonding with silicon. The glass is also used for the substrates of many microsystems. Further development of glass fabrication technology will open a new era in sensor technologies such as 3D flow channel systems, and electrical or optical interconnection between layered sensor components put combination by anodic bonding. There are several ways to etch glass substrates. In this thesis, wet etching with hydrofluoric acid is used. There are two methods which have been tried as mask materials, photoresist and metals (Au/Cr). Photoresist was tried first, since it is cheaper and fast. The process specifications follow below:

In Table 4.7, after Corning 7740 glass was placed for 1 hour in BOE (Buffered oxide etching) with S3813 photoresist as a mask material, bubbles are brought about beneath the photoresist, which means that the BOE has started to peel off the photoresist and attack undesired areas. Therefore, the second option was tried, using gold and chromium as mask materials. In using Au/Cr as a mask material, the process is the same as in Table 4.7 other than the photolithography step. Instead, gold and chromium are deposited on glass wafer by sputtering to a thickness of 500/50nm .

To detail process steps, the cleaning step is the same as that for a standard silicon wafer. It is cleaned in baths of primary NMP, secondary NMP, and DI water rinse for 10 minutes each. After that, it is put in the p-clean bath, hot DI water, and cold DI water. Using sputter deposition, Gold/Chromium is deposited to 500nm/50nm. Gold can be etched with an aqueous KI_3 solution, an opaque, black etchant with corrosive vapors (due to excess I_2). The opacity of this etchant makes end-point detection quite difficult. It is generally used in a temperature range of 20 to 50°C. Chromium can be etched using etchants such as 5g ceric ammonium nitrate, 4ml nitric acid (70%) in 5ml H_2O, and is generally used at 25°C.

Normally Chromium has very good adhesion to glass. Nevertheless, in this sample, there is huge lateral etching compared with vertical etching (~30:1). In Figure 4.27, the etching rate is linear to etching time. However, one interesting observation came to light. As etching proceeds, the HF solution absorbs residues of reactant, especially, at the corners. New BOE solution provides lateral etching that is twice larger than old solution which has been used for 3+ hours. In 4.26, it looks like an anisotropic shape,

however, it is seen that this etching follows isotropic behavior when the ratio of x and y scales is shown.

Table 4.7 Process Steps for Glass Etching Using a Photoresist Mask

Process	Specification
Primer Spinning	5000rpm/20sec
Cooling down	30sec
S3813	2000rpm/30sec
Prebake	90C/30sec
Expose	18sec
Postbake	110°C/60sec
Develop	MF319
Hardbake	110°C/5min
BOE(6:1)	1hr 20min
Film thickness	0.9um
Etching rate	15.5nm/min
Etching depth	1.4um

An alternative is a dry etching process using DRIE. Pyrex glass can be etched by deep reactive ion etching using SF_6 plasma. Pyrex glass is a glass suitable for DRIE because it contains only a small percentage of mass ratio of nonvolatile atoms such as Na and Al. Xinghua Li [26] reported the characteristics of the Deep RIE of glass in SF6 plasma. High etch rates (~0.6um/min) were achieved for Pyrex glass under low pressure (0.2Pa) and high self-bias voltage (-390V). This means that physical sputter-etching helps to remove nonvolatile etch products during the etching process.

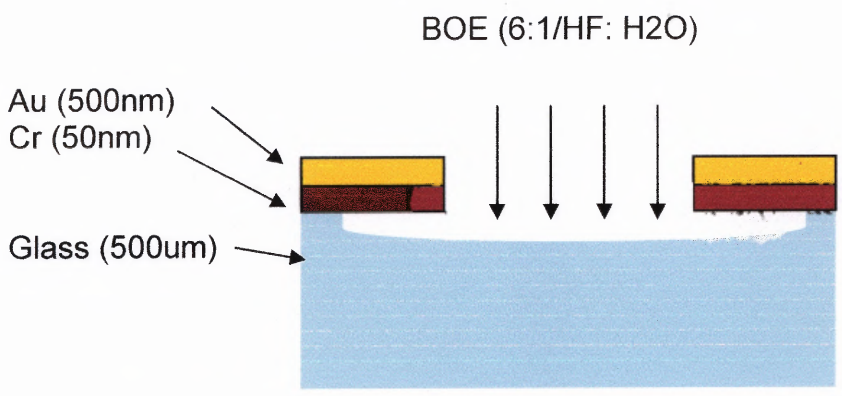

Figure 4.25 A side view of glass etching; BOE wet etching after depositing Au/Cr and photoresist patterning.

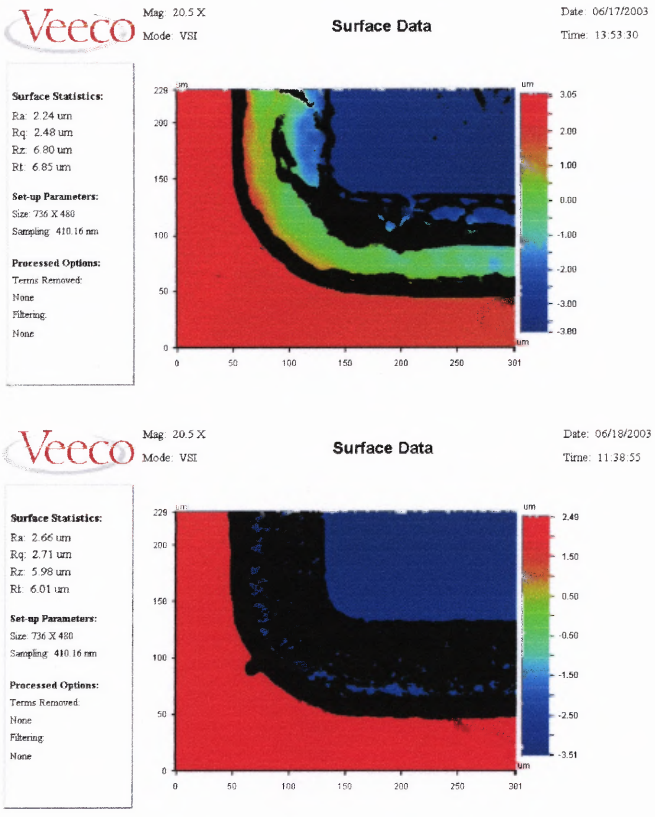

Figure 4.26 Veeco optical profilometer images after 300min BOE etching; (a) before, (b) after the Au/Cr mask layer is stripped.

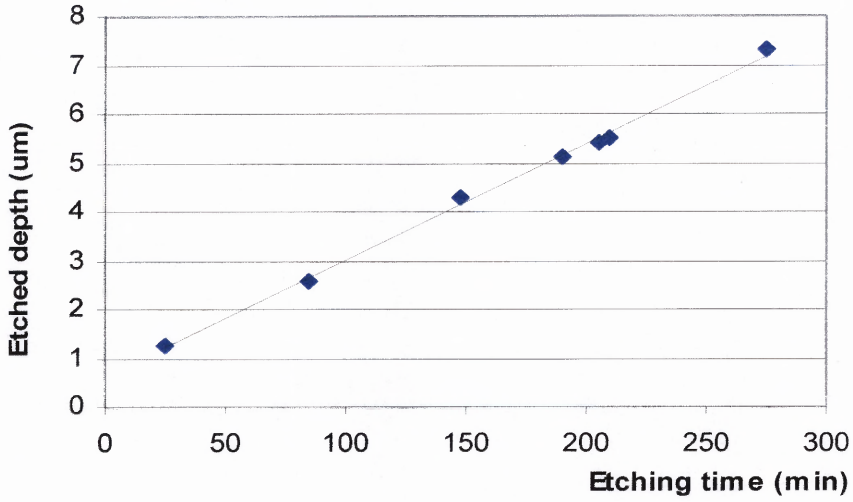

Figure 4.27 Relationship between etching time and etching depth.

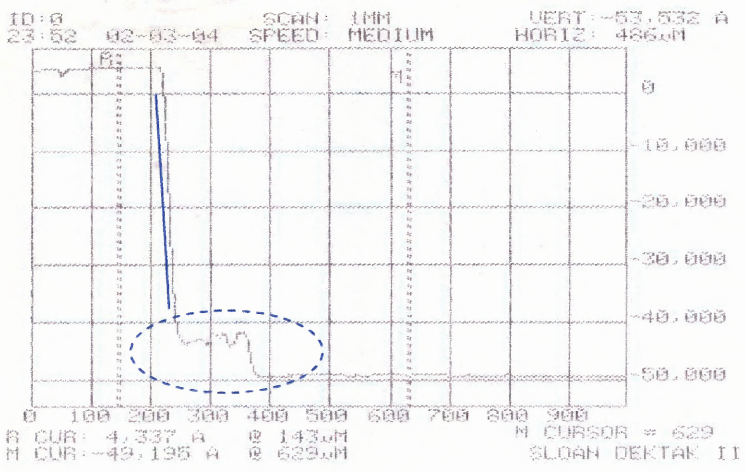

Figure 4.28 The Dektek vertical depth measurement of glass etching up to 5.3um deep in BOE solution for 300min.

4.6 Discussion

4.6.1 Fabrication Issues

It is important to recognize that the wafer handling, such as cleaning and storage between steps after fusion bonding, has failed several times. The cleaning step is really important, particularly in fusion bonding, and furthermore, in all the steps. In deep reactive ion etching (DRIE), even if there are many advantages, there are some certain techniques that should not be ignored.

1. If it is necessary to do DRIE after wafer bonding, it should be done very carefully since DRIE requires low vacuum levels.

2. A supportive dummy substrate should be used for etch-through etching. When the wafer is etch-through without this supporting substrate, the helium sensor detects that a wafer is properly not loaded the operation of the DRIE will stop working.

3. Photoresist should be hard baked enough not to stick to the holding ring in the chamber when the chamber is heated up during deep etching.

4. In glass wet etching, large lateral etching occurs due to surface tension in the interface of Cr/Au/Glass. Recently reported dry glass etching may be recommended for shapes with sharp edges [27].

4.6.2 Packaging Issues for Quality and Reliability

A MEMS product is complete only when it is fully packaged. Packaging is one of the major technical issues that has caused the long development times and high costs of MEMS products. Many MEMS devices such as accelerometers, pressure sensors and Coriolis mass flow meters require their moving parts to be enclosed in hermetically sealed ultrahigh vacuum cavities that can be fabricated by using wafer level bonding techniques. An even more important problem concerns the maintenance of the high vacuum over the lifetime of the sensors [36].

CHAPTER 5

EXPERIMENTS

5.1 First Prototype of the Resonant Beam Coriolis True Mass Flow Meter

The first prototype was made from a silicon tube structure, both with and without the resonant beam. The silicon tube structure without the resonant beam was over-etched during back-side DRIE as in Figure 5.1. A suspended tube structure was released fully. For the case of the tube structure with the resonant beam, the oxide layer still remained, as in Figure 5.2(a), (b) since a SOI wafer was used as cover layer to make the tube loop, after back-side DRIE. In order to release the resonant beam from the oxide layer, the wafer should be in an HF (100:1) solution for a few seconds. Figure 5.2(c), (d) shows the device after the release of the resonant beam.

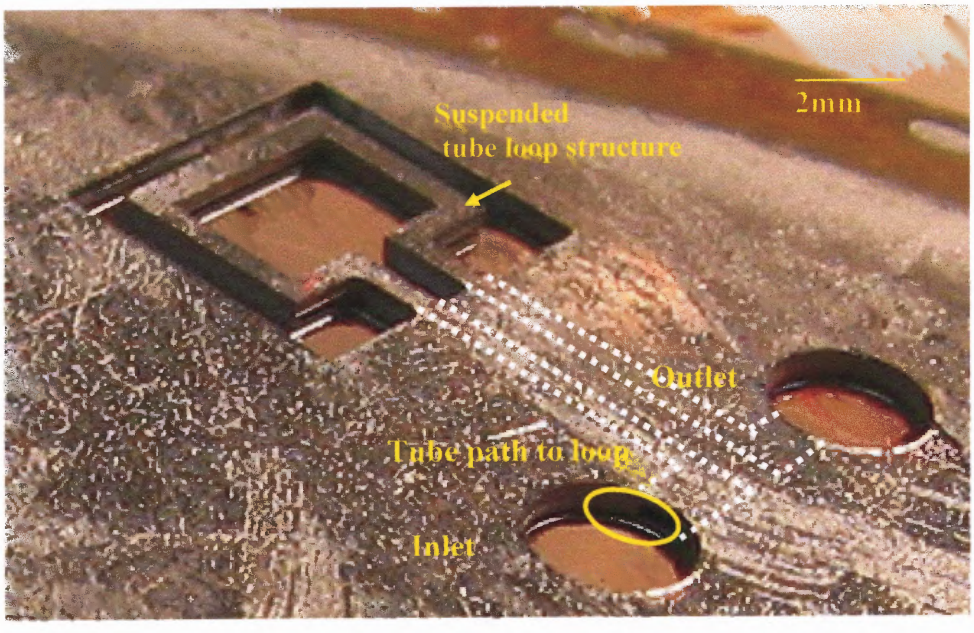

Figure 5.1 The Micromachined silicon tube loop structure without resonant beam.

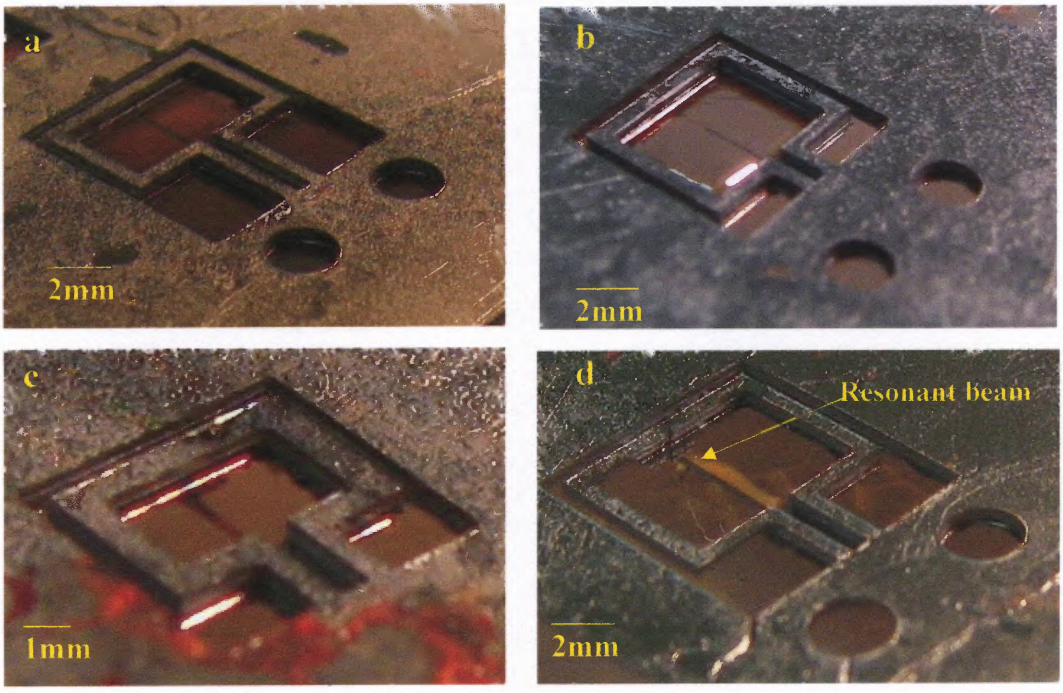

Figure 5.2 The pictures captured by a digital camera; (a),(b),(c) before releasing the oxide layer, and (d) the prototype device after releasing the oxide layer.

5.2 Experiments for Testing Natural Frequency

The experiment set-up has mainly three parts for a basic testing shown in Figure 5.3: D.C. power supply, a function generator, and an oscilloscope. The A.C. voltage source is superposed on the D.C. source. The signals of input and output can be seen in the oscilloscope. This A.C. source is controlled by a function generator. In Figure 5.4, input voltage is A.C. 5V and output is A.C. 0.44 ~ 0.97V. The investigated device is the device shown in Figure 5.2 (d). The measured natural frequency is about 1.4 kHz shown in Figure 5.4. This agrees with the simulation results in Figure 5.5 and Figure 5.6. However, the testing data do not match with the data which were discussed in Chapter 3 since only a few devices were successfully realized from the various devices in the wafer and these had a slightly different structure from the one chosen for the simulation.

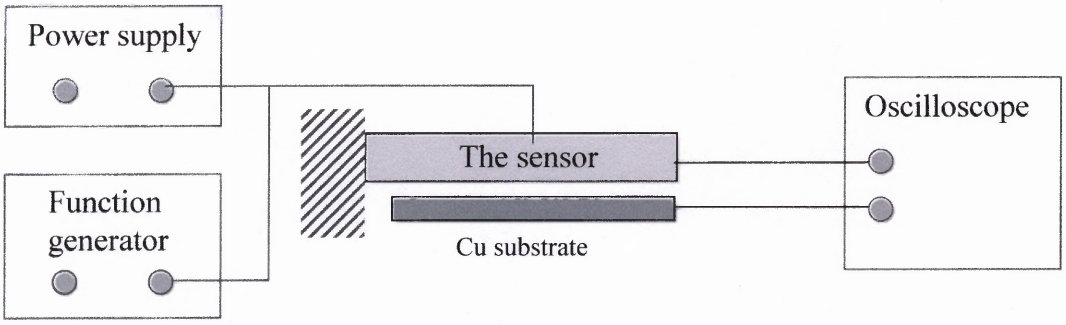

Figure 5.3 Schematic sketch of testing the natural frequency.

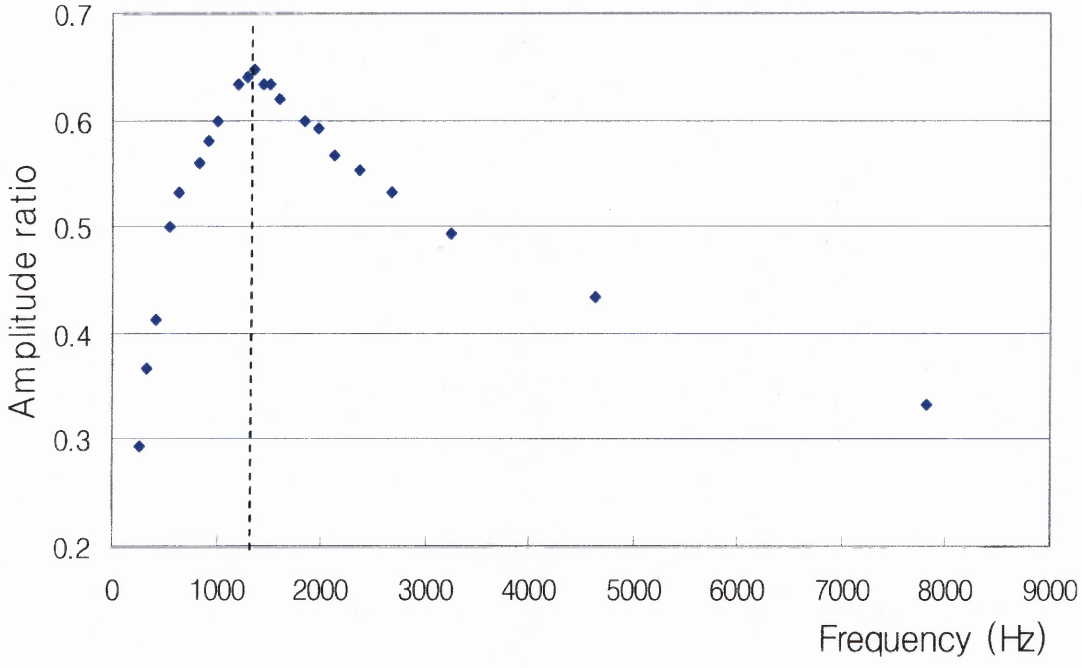

Figure 5.4 A.C. response for the bending of a tube loop structure with resonant beam. The natural frequency is ~1.4kHz. Q-factor is very low due to the damping effect of air.

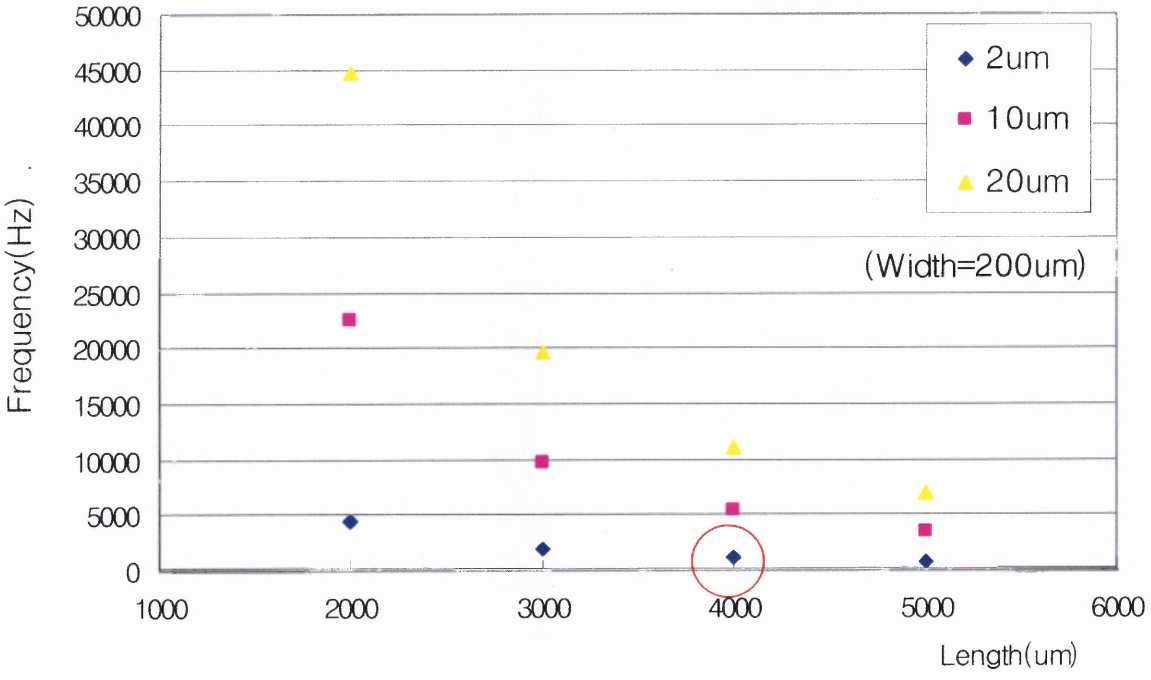

Figure 5.5 Simulation results for resonant beams of different sizes.

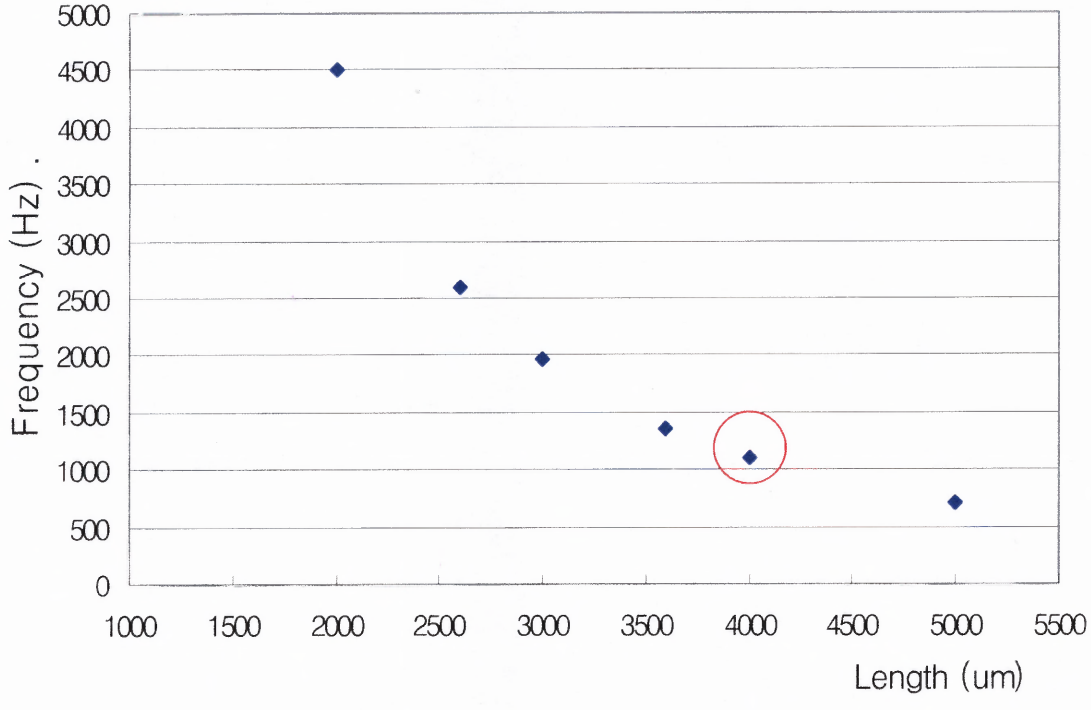

Figure 5.6 Simulation results for resonant beams of 200um width and 2um thick.

5.3 Experiments for Electrostatic Actuation

5.3.1 Electrostatic Actuation

This capacitive method, used as a sensing technique, has been mentioned in Section 3.4.1. Now, in the following Section this method is reviewed as an actuation technique. To drive or excite torsion vibration and resonant beam vibration, electrostatic actuation has been used as another aspect of the capacitive principle. Electrostatic actuators can be modeled as variable capacitors suspended by a spring structure. An effective bias voltage is across the variable capacitor/actuator. The structural equation can be given by applying Newton's Second Law to the basic actuator system [9]:

$$\frac{1}{2}\frac{dC}{dx}V^2 = Kx \tag{5.1}$$

Where C is the actuator capacitance of the system, and K and x are spring stiffness and displacement, respectively. The equation describing the pull-in effect is given by differentiating with respect to x, and multiplying by x and subtracting equation (5.1) in equation (5.2):

$$\frac{\partial^2 C}{\partial^2 x_{pin}} - \frac{1}{x_{pin}}\frac{\partial C}{\partial x_{pin}}\bigg|_{x=x_{pin}} = 0 \tag{5.2}$$

The pull-in voltage can be therefore be derived by combining equations (5.1) and (5.2)

$$V_{pin} = \sqrt{\frac{2K}{\frac{\partial^2 C}{\partial x^2}\Big|_{x=x_{pin}}}} \tag{5.3}$$

Rewriting the pull-in equation at the pull-in point results in:

$$\frac{1}{2}\frac{dC}{dx}V_{pin}^2 = Kx_{pin} \tag{5.4}$$

Combining equations (5.2) and (5.4) cancels out spring parameters and yields a two-parameter unitless equation [9]:

$$\Lambda \cdot U^2 = 1 \qquad \Lambda = \frac{\frac{1}{x}\frac{dC}{dx}}{\left[\frac{1}{x}\frac{dC}{dx}\right]_{x=x_{pin}}} \qquad U = \frac{V}{V_{pin}} \qquad \text{(5.5a, b, c)}$$

From the above equations, it is apparent that the pull-in position is independent of spring stiffness K, which is only variable **as** the pull-in voltage changes. Additionally, the first and second derivates of the capacitance characterize an electrostatic microactuator, the pull-in position and actuation curve can be easily obtained by applying equations (5.1)-(5.5), without going through a coupled electrical-structural analysis [9]. For a parallel rigid plate capacitor system, the capacitance can be expressed as:

$$C = \frac{\varepsilon A}{d - X} \qquad (5.6)$$

where d is the initial distance and X is the displacement by electrostatic attraction force. Applying equations (5.6) into equations (5.2) and (5.3), the pull-in position and pull-in voltage are given by [9, 35]:

$$X_{pin} = \frac{1}{3}d \qquad V_{pin} = \sqrt{\frac{0.83Kd^3}{\varepsilon L^3 W}} \qquad \text{(5.7a, b)}$$

Pull-in position can be determined by only capacitance while pull-in voltage can be determined by the spring stiffness of the deformable plate as well as capacitance [35].

5.3.2 Electrostatic Torsion Actuation

With regard to the proposed device, the actual structure is close to a rectangular full-plate torsion actuator, for which capacitance is written as [9]:

$$C = \frac{\varepsilon_0 A}{L\theta} \ln \frac{D}{D - L\theta} \tag{5.8}$$

Where θ is the tilt angle between the two plates of the capacitor system and A is the area of the electrode area. The pull-in deflection angle is calculated to be $\theta_{pin} \approx 0.44 \cdot \tan^{-1}(D/L)$, and the corresponding pull-in voltage is: [9]

$$V_{pin} \approx \sqrt{\frac{0.83 K_\theta D^3}{\varepsilon_0 L^3 W}} \tag{5.9}$$

where K_θ is the torque stiffness, and D, W and L are the initial gap depth, electrode width and electrode length, respectively. In an investigated Coriolis-type actual device, this conceptual application of torsion cantilever actuation can be applied to the device since the static motion of the device is very similar to the torsion cantilever motion.

The simulations of bending and torsion electrostatic actuation are investigated in Figure 5.7. The simulation results explain the relationship between pull-in voltage and pull-in distance. In Figure 5.9, a larger sized structure is investigated for the same pull-in effect. The results show the same features as Figure 5.8. In other words, a third of the gap is shown as pull-in distance in bending actuation while half the gap is shown as pull-in distance in torsion actuation.

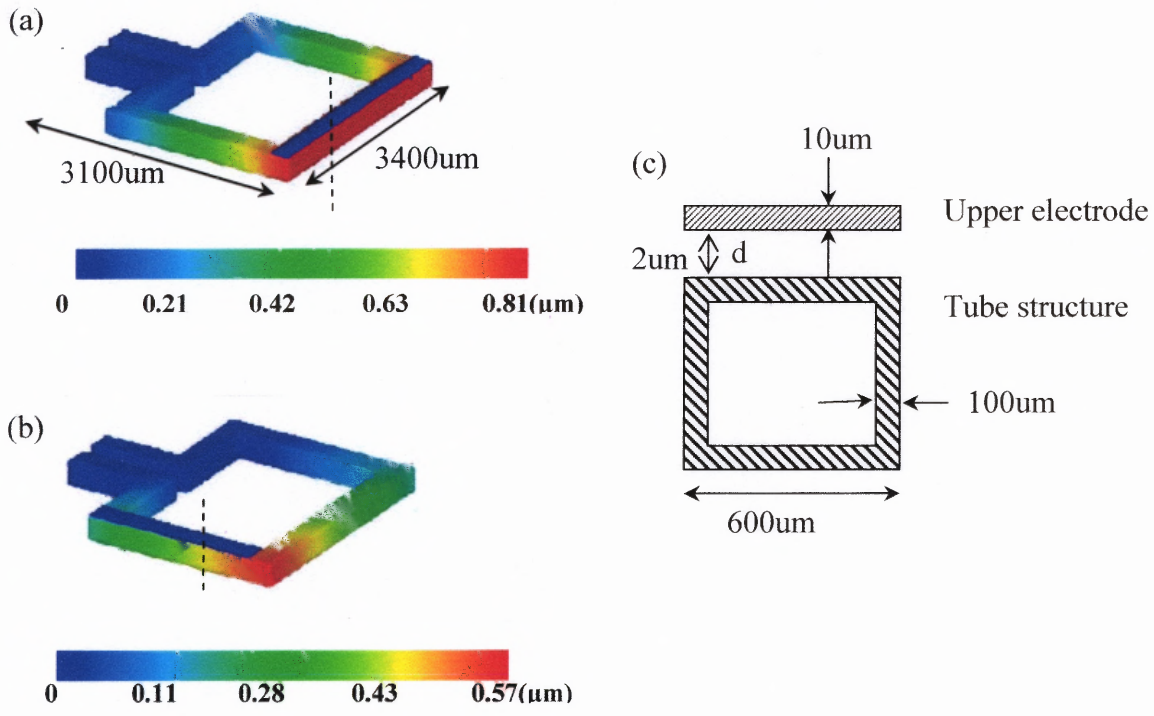

Figure 5.7 Simulation results for bending and torsion electrostatic pull-in effects; (a) bending actuation, (b) torsion actuation, (c) side view of actuation system.

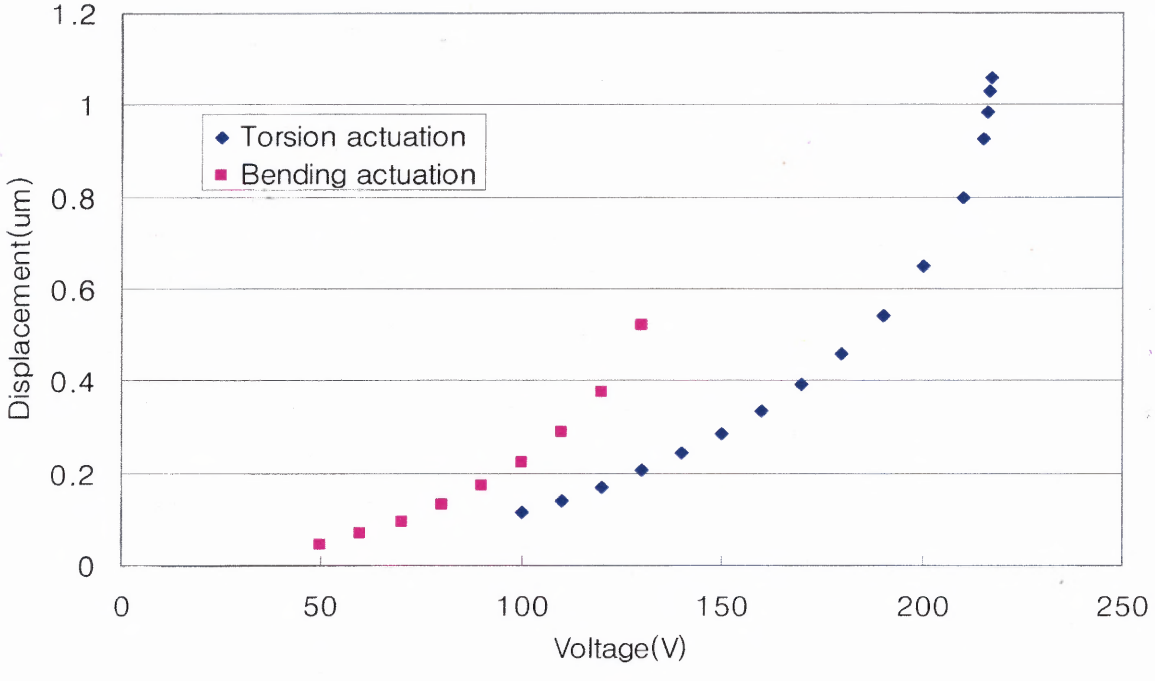

Figure 5.8 Pull-in effect of bending and torsion actuations in Figure 5.7 (a), (b).

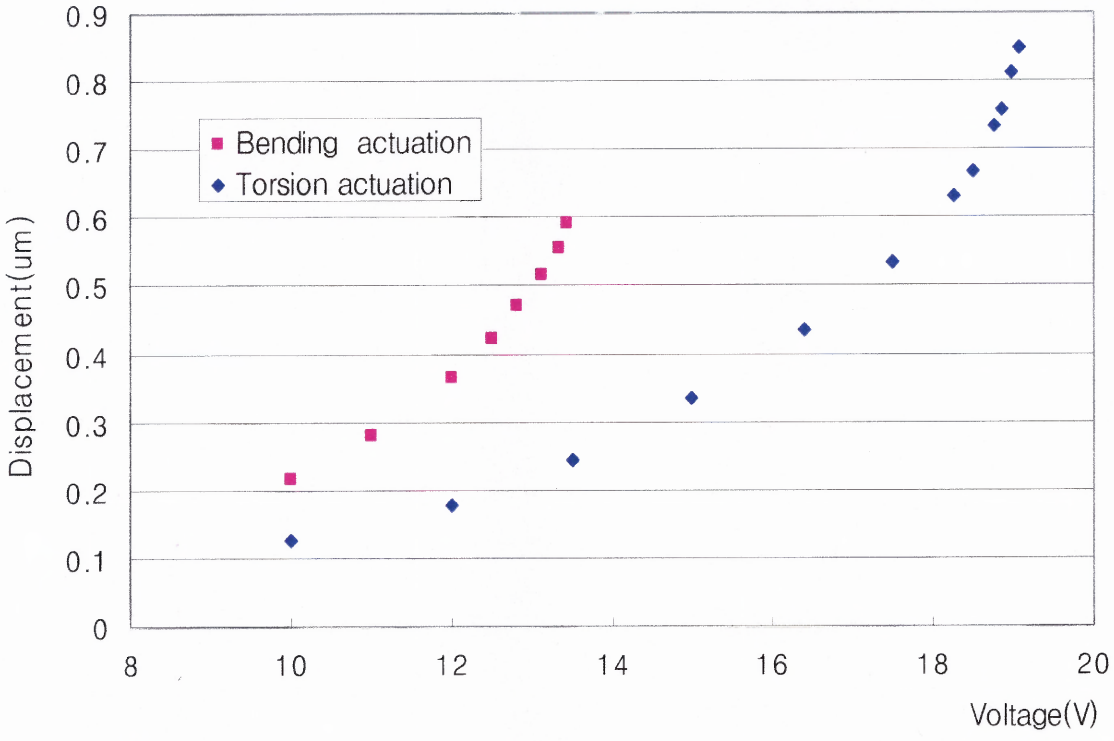

Figure 5.9 Pull-in effect bending and torsion actuation in the larger (6000 x 5000um^2) version of the same structure as Figure 5.7.

5.3.3 Measuring the Capacitance for Electrostatic Actuation

Measuring the capacitance of the device gives information if the electrostatic actuator works properly. There is one parallel plate capacitor in the measurement, in which the device is the upper electrode and the copper substrate is the lower electrode in Figure 5.10. The cantilever-type device is excited by the attractive Coulomb force between the two capacitor plates. If these parallel plates are fixed, many charges are accumulated between these plates and a high electric field occurs. However, if one of the plates is movable, the accumulated charges attract each other and one movable plate bends

towards the other plate. This is called the "pull-in effect." In terms of capacitance, capacitance does not change in the fixed plates set-up if the applied area is not changed. The simplified equivalent circuit of the testing set-up is shown in Figure 5.10(b). Three different devices are used in this experiment. The parameters of each sample are shown in Table 5.1.

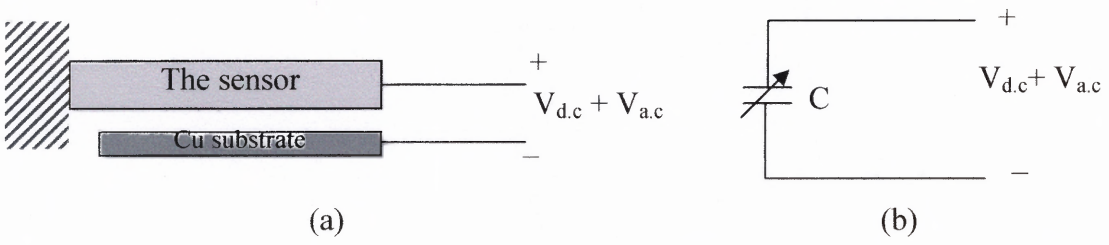

Figure 5.10 Capacitance measurement setup; (a) schematic, (b) simple lumped parameters for an equivalent circuit.

In Figure 5.10, the picture shows that the capacitance increases as the voltage increases, which means that one fixed substrate and one movable device attract each other and the substrate is pulling in the device. Calculated pull-in voltage is [9]:

$$V_{pin} = \sqrt{\frac{8kd^3}{27\varepsilon A}} \tag{5.10}$$

where k is spring constant (k=9000 based on simulation results), d is the distance between device and substrate, A is device area (3.1x3.4cm^2), and ε is permeability (8.854x10^{-11}F/cm). Pull-in voltage, V_{pin} is 211V, which means the device travels 8um with 211V. The voltage range applied is within the range of 10-100V due to a limited testing set-up. The moving range of the movable device in the range of 10-100V is very small, so that the capacitance is not much changed.

Table 5.1 Parameters for Measurement Set-up

Sample No.	1	2	3
Total device area, A(um^2)	3100x3400	6000x5000	3100x3400
Distance, d(um)	~25	~25	~25
Applied d.c. voltage (V)	10~30	10~100	10~100
Applied a.c. voltage (V)	500mV	-	-
Note			Oxide layer not released

In Figure 5.11, the capacitance of sample #3 increases more than that of sample #1 because the spring constant is less stiff due to the thin oxide layer, even before the resonant beam is released from the oxide layer. In Figure 5.12, the graph shows the difference between when tip pressure is applied to the tube loop structure and when no pressure is applied. In Figure 5.13, the graphs show the device is moving, which means the device bends towards the substrate.

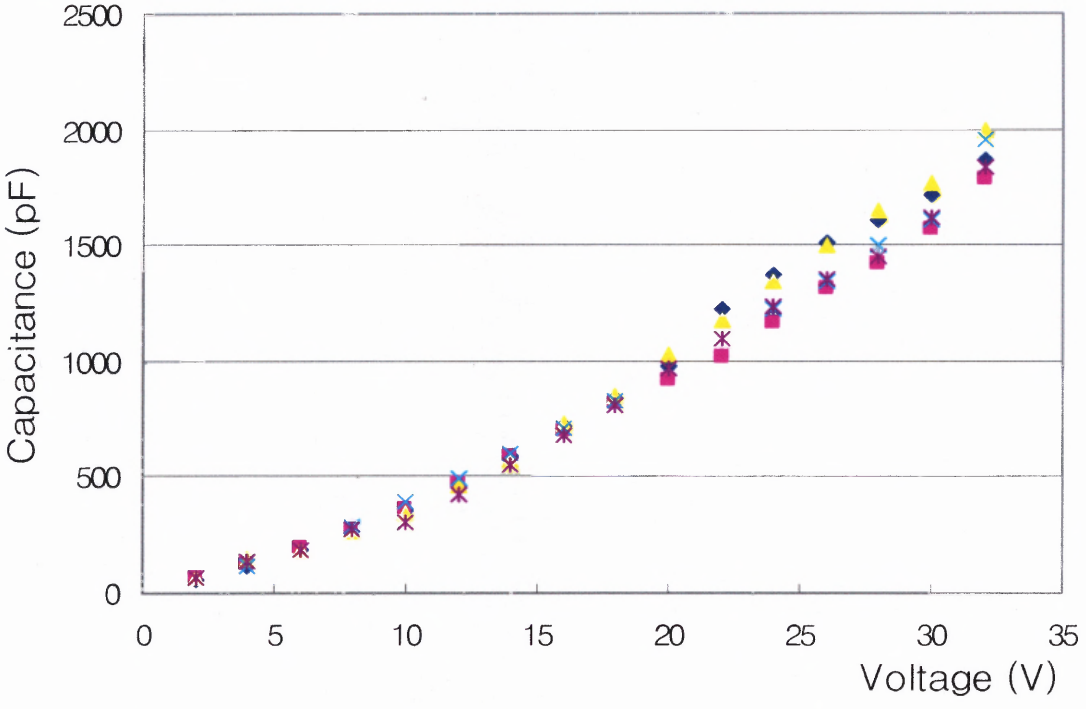

Figure 5.11 C-V measurement for sample #3; mass flow sensor with resonant beam.

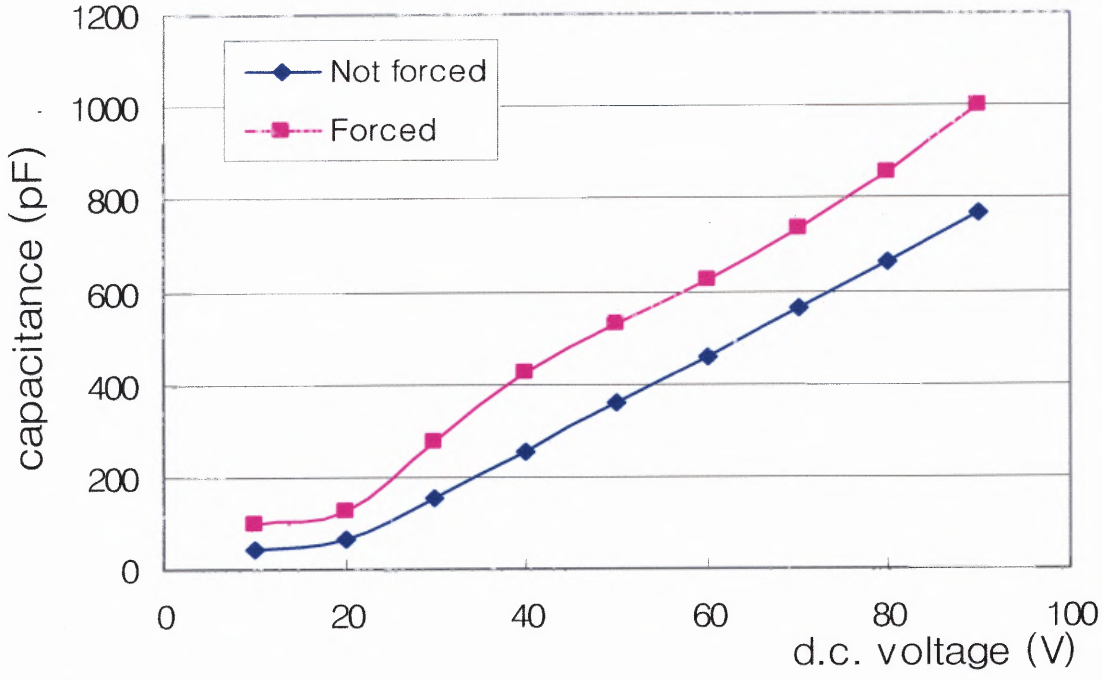

Figure 5.12 C-V measurement for sample #2.

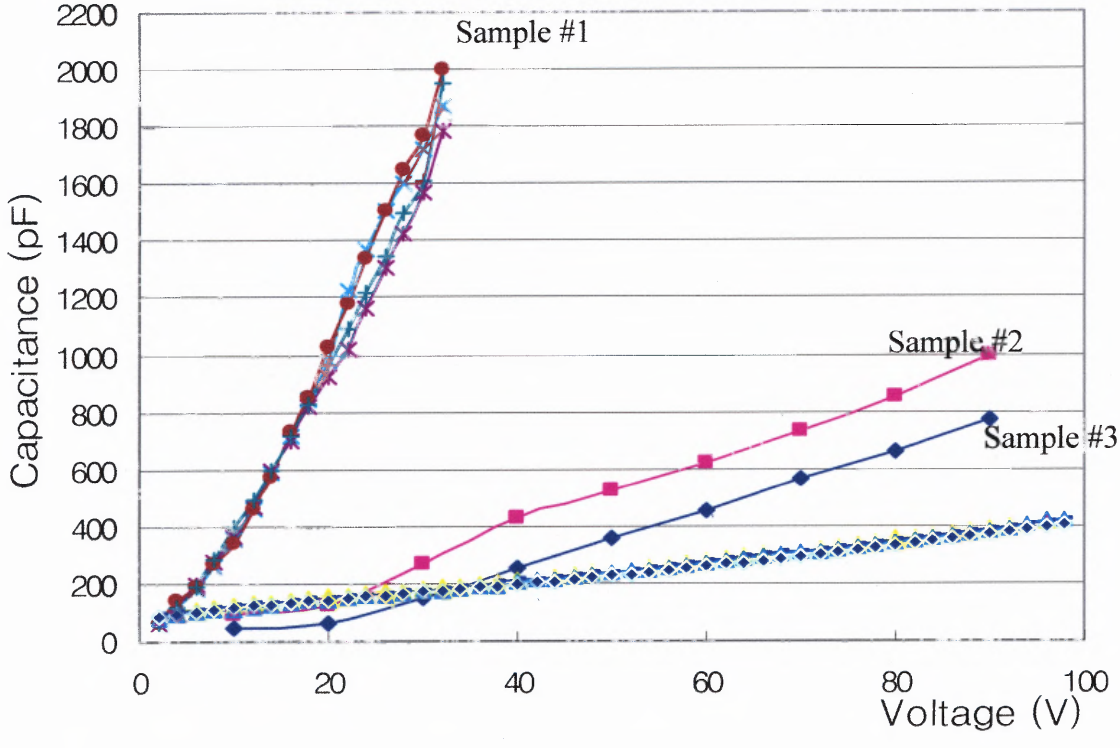

Figure 5.13 Comparison among different devices.

5.4 Discussion

The resonance frequencies of a beam with rigidly fixed ends increase with increasing amplitude of bending vibrations. This effect is known as the hard-spring effect and is due to the stretching of the microbeam at vibration amplitudes. The resonant beam with stretching effects produced by Coriolis force basically shows a parametric response to mass flow. This is the first attempt to apply the already well-known resonant beam detecting method to measuring mass flow based on the Coriolis principle. During theoretical modeling, fabrication, and testing, there were some issues that should be mentioned. It is possible to apply a resonant beam to measure the displacement of a bending structure in a cantilever-type structure, at least in this design as well as in a structure with both ends fixed. Through the stretching effect of the bending structure, the resonant beam for Coriolis mass flow sensors plays the same role as a resonant pressure sensor. The only different thing is that the resonant beam for Coriolis mass flow sensors has a frequency response in the pseudo-dynamic resonant beam method, one of its main advantages, and this can be digitalized and is detectable even in very minute changes as summarized in Section 1.4. Even if the mechanical frequency itself does not have the best sensitivity, this resonant beam method utilizes its property as a transducer as much as possible. Analog mechanical frequency can be measured from the digital circuit system or FFT.

CHAPTER 6

CONCLUSION AND FUTURE WORK

6.1 Conclusion

This thesis has demonstrated that the pseudo-dynamic resonant beam can be used as a Coriolis force detection method for micromachined mass flow sensors. The principle of resonant beam measurement has been studied for static and dynamic inputs. Resonant measurement at the micromechanical scale allows for the precise detection of μN forces and it has the advantages of a direct quasi-digitalized frequency output and good output linearity. However, this project has also demonstrated that resonant beam measurement is not yet applicable to the detection methods of Coriolis force and Coriolis mass flow sensors because of certain difficulties enumerated below. There are some issues yet to be resolved such as: 1) the resonant beam frequency should be much larger than the torsion frequency (Section 3.4.8). 2) When the Coriolis force is perpendicular to the beam the resonant beam is much less sensitive than when the direction of the Coriolis force is parallel to the beam (Section 3.4.4). 3) The stress profile of the resonant beam is not constant, so that Timosenko's vibration theory may not be applied (Section 3.4.6). 4) The noise effects are too significant to be ignored (Section 3.5), and 5) the 1g/s of investigated mass flow exceeds the capability of the simulated 100x100um^2 cross-section structure. But it does work in the 10 times bigger cross-section structure (Section 3.2 and Section 3.4.5). Thus, below there are some suggestions that may realize the potential of the resonant beam method.

6.2 Design Optimization

The resonant beam method has limitations for detecting Coriolis force; a small (1~3%) frequency shift due to the bending effect of the beam and frequencies coupling due to the resonant beam and Coriolis vibration in the same direction. The small frequency shift requires a high quality factor which means high vacuum sealing. In order to maximize the sensitivity of the resonant beam, axial Coriolis force should be applied instead of vertical Coriolis force. The sensitivity of detection can be improved when the direction of the Coriolis force is parallel to the resonant beam than when the Coriolis force is perpendicular to the beam, as shown in Figure 6.1. The difference of the length change in the beam is easily calculated by the equation below. The left side shows Coriolis force parallel to the direction of the beam and the right side shows Coriolis force that is perpendicular to the beam which gives a very small change.

$$\Delta l >> \Delta l \sin\theta \tag{6.1}$$

Since the resonant beam behaves like a cantilever beam, the length change is even smaller than $\Delta l \sin\theta$. A vertically connected resonant beam would be the best structure for resonant sensing but the details of fabrication of this sort of device have yet to be fully realized.

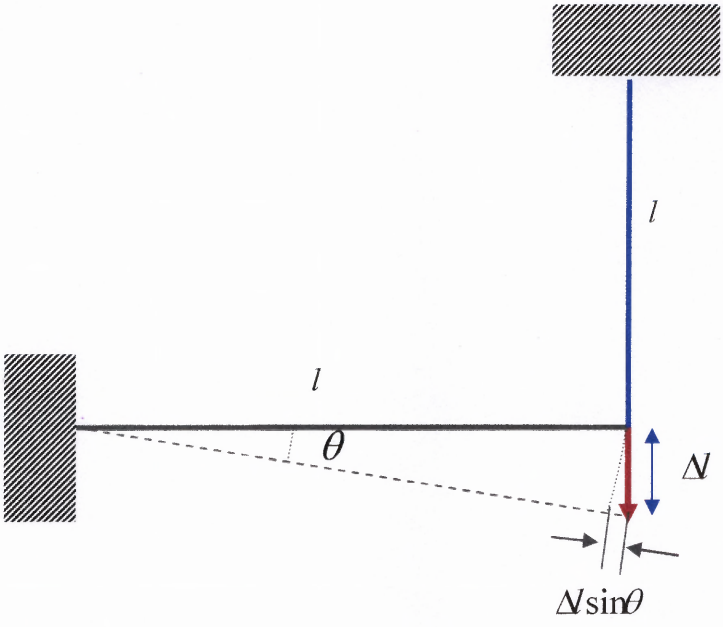

Figure 6.1 A vertical resonant beam for a Coriolis mass flow sensor.

6.3 Frequencies Separation

In Chapter 3 there was a discussion of the results caused by the Coriolis force acting in the z-direction and the resonant beam excitation also vibrating in the same z-direction. In this case, the Coriolis vibration and the resonant beam vibration would be coupled in the same direction, so that these vibrations would need to be separated through a filtering circuit. However, the undesirable cross-coupling can be avoided more easily when the resonant beam vibrates laterally as if in a resonant gyroscope, as shown in Figure 6.2. If the resonant beam vibrates on the y-direction, the frequency of the resonant beam can be detected by the Coriolis force without the Coriolis vibration being interrupted or interfered with.

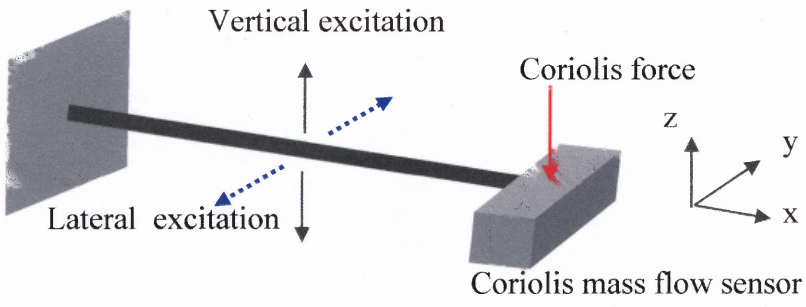

Figure 6.2 Schematic of the lateral excitation of the resonant beam vibration.

APPENDIX A

THE CORIOLIS FORCE [21]

An explanation and discussion of Coriolis force follows. The Coriolis force is one of factors in relative acceleration on a moving coordinate system. Let us consider that the location of a point P is established in a xyz coordinate system. In the meantime, this coordinate system moves simultaneously with a translational velocity and an angular velocity in terms of a fixed XYZ coordinate system. A general expression is derived for the acceleration of a point regarding a coordinate system which is moving itself.

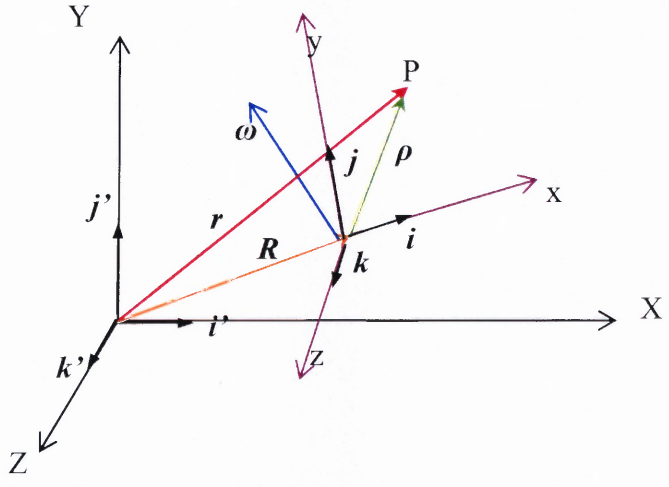

Figure A.1 A moving xyz coordinate system in respect to a "fixed" XYZ coordinate system [21].

The vectors R and r should be traced in the fixed XYZ system. The unit vectors have the direction of the moving coordinate axes, as well as the direction of the fixed coordinate axes. The displacement measurement to the fixed XYZ system determines the absolute displacement r of the point P. The absolute velocity $\dot{r}$ and the absolute acceleration $\ddot{r}$ are given by differentiating this absolute displacement.

$$\vec{r} = X\vec{i}' + Y\vec{j}' + Z\vec{k}' \tag{A.1}$$

$$\dot{\vec{r}} = \dot{X}\vec{i}' + \dot{Y}\vec{j}' + \dot{Z}\vec{k}' \tag{A.2}$$

$$\ddot{\vec{r}} = \ddot{X}\vec{i}' + \ddot{Y}\vec{j}' + \ddot{Z}\vec{k}' \tag{A.3}$$

As the absolute motion is measured in the moving xyz system, it is given by:

$$\vec{r} = \vec{R} + \vec{\rho} = \vec{R} + x\vec{i} + y\vec{j} + z\vec{k} \tag{A.4}$$

where the direction of the unit vectors are given regarding the fixed system. However, the directions of unit vectors change with time since they rotate with the xyz system. In taking the derivatives $\dot{r}$ and $\ddot{r}$, therefore, the time derivatives of these unit vectors must be included:

$$\dot{\vec{r}} = \dot{\vec{R}} + \dot{\vec{\rho}} = \dot{\vec{R}} + \dot{x}\vec{i} + x\dot{\vec{i}} + \dot{y}\vec{j} + y\dot{\vec{j}} + \dot{z}\vec{k} + z\dot{\vec{k}} \tag{A.5}$$

The derivatives of the unit vectors are provided by equations:

$$\dot{\vec{i}} = \vec{\omega} \times \vec{i}; \dot{\vec{j}} = \vec{\omega} \times \vec{j}; \dot{\vec{k}} = \vec{\omega} \times \vec{k} \tag{A.6a, b, c}$$

Therefore,

$$\dot{\vec{r}} = \dot{\vec{R}} + (\dot{x}\vec{i} + \dot{y}\vec{j} + \dot{z}\vec{k}) + \vec{\omega} \times (x\vec{i} + y\vec{j} + z\vec{k}) \tag{A.7}$$

The velocity of the point P, measured to the xyz coordinate system is called the relative velocity ($\dot{\rho}_r$). The expression for $\dot{r}$ becomes:

$$\dot{\vec{r}} = \dot{\vec{R}} + \dot{\vec{\rho}}_r + \vec{\omega} \times \vec{\rho} \tag{A.8}$$

The acceleration of P is come across by a second differentiation:

$$\begin{aligned} \ddot{\vec{r}} &= \ddot{\vec{R}} + \ddot{\vec{\rho}} = \ddot{R} + (\ddot{x}\vec{i} + \ddot{y}\vec{j} + \ddot{z}\vec{k}) + (\dot{x}\vec{i} + \dot{y}\vec{j} + \dot{z}\vec{k}) \\ &+ \dot{\vec{\omega}} \times (x\vec{i} + y\vec{j} + z\vec{k}) + \vec{\omega} \times (\dot{x}\vec{i} + \dot{y}\vec{j} + \dot{z}\vec{k}) + \vec{\omega} \times (x\vec{i} + y\vec{j} + z\vec{k}) \end{aligned} \tag{A.9}$$

Plugging in $(\ddot{x}i + \ddot{y}j + \ddot{z}k) = \ddot{\rho}_r$, the relative acceleration of the point P, the expression for $\ddot{r}$ can be given by:

$$\ddot{\vec{r}} = \ddot{\vec{R}} + \vec{\omega} \times (\vec{\omega} \times \vec{\rho}) + \dot{\vec{\omega}} \times \vec{\rho} + \ddot{\vec{\rho}}_r + 2\vec{\omega} \times \dot{\vec{\rho}}_r \tag{A.10}$$

The last term $\omega \times \dot{\rho}_r$ is called the acceleration of Coriolis, after G. Coriolis (1792-1843), a French engineer who first called attention to this term. The equation of motion in terms of the Newton's Second Law can be written by:

$$\vec{F} = m\ddot{\vec{R}} + m\vec{\omega} \times (\vec{\omega} \times \vec{\rho}) + m\dot{\vec{\omega}} \times \vec{\rho} + m\ddot{\vec{\rho}}_r + 2m\vec{\omega} \times \dot{\vec{\rho}}_r \tag{A.11}$$

APPENDIX B

STRESS ANALYSIS FOR A PURE BENDING STRUCTURE

A tiny segment of a beam has become bent in response to the application of transverse loads in figure B.1 [34]. Applied moment shows a positive sign as does the radius of curvature. The dashed arc in the middle of the beam is called the neutral axis. It is the axis whose length is not changed by bending.

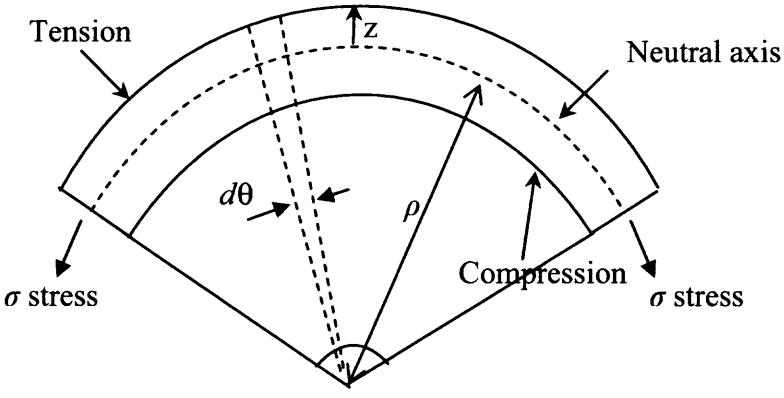

Figure B.1 A section of a beam in pure bending [31].

Fractions above the neutral axis are strained in tension, at the same time as fractions of the beam below the neutral axis are squeezed into compression by the bending. When the beam is bent, the length of an arc segment that subtends an angle depends on how far it is from the neutral axis because there is a small deviation in radius of curvature from the top to the bottom of the beam [34]. The length of the dashed segment at position z is

$$dL = (\rho - z)d\theta \tag{B.1}$$

At the place of the neutral axis, the length of the consequent segment is equal to the differential length of the segment when the beam is not bent. That is,

$$dx = \rho \cdot d\theta \tag{B.2}$$

From which we obtain

$$dL = dx - \frac{z}{\rho} d\theta \tag{B.3}$$

Since the unbent length of the segment is *dx*, we conclude that the axial strain at position z is

$$\varepsilon_x = -\frac{z}{\rho} \tag{B.4}$$

Because stress and strain are proportional, there is also an axial stress in the beam segment whose value depends on z. the expression is

$$\sigma_x = -\frac{zE}{\rho} \tag{B.5}$$

This structure has a distribution of internal stresses. The curvature of beam is related to the free bending of cantilever-type tube structures.

APPENDIX C

PROCESS TRAVELER FOR THE SENSOR DEVICE

This traveler was used to make the device in the cleanroom following the fabrication process flow in section 4.4.

Table C.1 Main Wafer Cleaning

	Date	Wafers	Operator	Comments
Starting materials: 4" p-type (100) Si Wafer ρ=1~10Ω.cm Thickness: 380μm Double side polished				One wafer will be used for testing
1. NMP first bath 110°C, 10 min				
2. NMP secondary bath 110°C, 10 min				
3. Rinse COLD DI 5 min				
4. P-clean 5:1 H_2SO_4:H_2O_2 110°C, 10 min				
5. Rinse HOT DI 10 min				
6. Rinse COLD DI 5 min				
7. Spin dry				
8. Furnace pre-clean 100:1 H_2O:HF 1 min				
9. Rinse COLD DI 5 min				
10. Spin dry				
11. Inspect				

Table C.2 Main Wafer Deep Etching (A-D)

	Date	Wafers	Operator	Comments
1. P-clean 5:1 H_2SO_4:H_2O_2 110°C, 10 min				
2. Rinse HOT DI 10 min				
3. Rinse COLD DI 5 min				
4. Spin dry				
5. Apply thick Photoresist (AZ 9260) 3000rpm, 30sec				
6. Soft bake: 100min in 110°C Cool on cold plate for 30 sec 18°C				
7. Align and expose Mask: INLOOP Time: 35 seconds				
8. Develop Apply developer MF 319 Wait for 2 min 30 sec Spin & Rinse with DI				
9. Hard bake 115°C for 15min Cool on cold plate for 60 sec 18°C				
10. Si dry Etching DRIE;400μm				
11. Strip PR M-pyrol, 95°C 10 min PRIMARY 10 min SECONDARY				Alternative way: Acetone and Isopropanol
12. Rinse COLD DI 10 min				
13. Spin dry				
14. Inspect				

Table C.3 Ion Implantation for Ultra Thin Silicon Wafer (E)

	Date	Wafers	Operator	Comments
Starting materials: • 4" p-type (100) Si wafer ρ=1-10Ω.cm Thickness: 100μm Double side polished				Special caution
1. P-clean 5:1 H_2SO_4:H_2O_2 110°C, 10 min				
2. Rinse HOT DI 10 min				
3. Rinse COLD DI 5 min				
4. Blow dry				
5. Furnace pre-clean 100:1 H_2O:HF 1 min				
6. Rinse COLD DI 5 min				
7. Inspect				
8. Ion implantation Boron dose: 10e+19 Energy: 5e+13 eV Target: 1000Å				
9. Annealing Temp :1050°C >1hr in N_2 or O_2				
10. Inspect				

Table C.4 Beam Patterning (F)

	Date	Wafers	Operator	Comments
Starting materials: The used wafer in step E				Special caution
1. P-clean 5:1 H_2SO_4:H_2O_2 110°C, 10 min				
2. Rinse HOT DI 10 min				
3. Rinse COLD DI 5 min				
4. Blow dry				
5. Apply Photoresist AZ 9620 2000rpm, 60sec				
6. Soft bake:110°C Cool on cold plate for 30 sec 18°C				
7. Align and expose Mask: BEAM Time: 20 seconds				
8. Develop Apply developer AZ 400K Wait for 4min Rinse in Cold DI				
9. Blow dry with N_2				
10. Hard bake 115°C for 10min Cool on cold plate for 60 sec 18°C				
11. DRIE Etching Poly-Si Target : 2um				
12. Inspect				
13. Strip PR M-pyrol, 95°C 10 min PRIMARY 10 min SECONDARY				Alternative way: Acetone and Isopropanol
14. Rinse COLD DI 10 min				
15. Spin dry				
16. Inspect				

Table C.5 Electrode Patterning in Silicon Wafer (G)

	Date	Wafers	Operator	Comments
Starting materials: The used wafers in step A-D Thickness: 380μm Double side polished				Special caution
1. P-clean 5:1 H_2SO_4:H_2O_2 110°C, 10 min				
2. Rinse HOT DI 10 min				
3. Rinse COLD DI 5 min				
4. Spin dry				
5. Sputtering Al Target: 2000Å				
6. Apply Photoresist Shipley 3813 2000rpm, 60sec				
7. Soft bake:110°C Cool on cold plate for 30 sec 18°C				
8. Align and expose Mask: BEAM Time: 20 seconds				
9. Develop Apply developer MF 319 Time: 3min Spin & Rinse with DI				
10. Hard bake 115°C for 60 sec Cool on cold plate for 60 sec 18°C				
11. Etching Al in Al etching bath Target : 2000Å Temperature:43 °C for 1 min Rinse with Cold DI				
12. Blow dry and Inspect				
13. Strip PR M-pyrol, 95°C 10 min PRIMARY 10 min SECONDARY				
14. Rinse COLD DI 10 min				
15. Spin dry				
16. Inspect				

Table C.6 Fusion Bonding (H)

	Date	Wafers	Operator	Comments
Starting materials: The 380μm Si wafer(A-D) The 100μm thin Si wafer(G)				
1. Rinse HOT DI 10 min				CAUTION! DO NOT P-Clean
2. Rinse COLD DI 5 min				
3. Spin dry				
4. Fusion bonding Force:1000N for 30 sec				
5. Inspect with IR camera				
6. Annealing Temp:1050°C >1hr in N_2 or O_2				
7. Inspect				

Table C.7 Back Side DRIE for Releasing the Tube Structure (I, J)

	Date	Wafers	Operator	Comments
Starting materials: The fusion bonded wafer(H)				
1. Rinse COLD DI 5 min				
2. Spin dry				
3. Apply Photoresist AZ 9620 1500rpm, 60sec				
4. Soft bake: 1100°C for 80sec Cold plate for 30 sec for 18°C				
5. Align and expose Mask: BACK CAVITY Time: 57 seconds				
6. Develop Apply developer AZ 400K Time: 60 sec Spin & Rinse with DI				
7. Hard bake 120°C for 10min Cool on cold plate for 60 sec 18°C				
8. Oxide etching for 3min 100:1 HF				
9. Rinse in Cold DI for 5 min				
10. Blow dry and Inspect				
11. DRIE etching Target: 380 μm				
12. Inspect				
13. Strip PR M-pyrol, 95°C 10 min PRIMARY 10 min SECONDARY				
14. Rinse COLD DI 10 min				
15. Spin dry				
16. Inspect				

Table C.8 Glass Machining (K-M)

	Date	Wafers	Operator	Comments
Starting materials 4" pyrex glass (7740) wafer Thickness: 500μm				
1. Rinse HOT DI 10 min				
2. Rinse COLD DI 5 min				
3. Sputtering Cr/Au Target : 50/500nm				
5. Apply Photoresist Shipley 3813 1500rpm, 60sec				
1. Soft bake: 1100°C for 80sec Cold plate for 30 sec for 18°C				Etching solution: HF Etching rate:
2. Align and expose Mask: WINDOWS Time: 19 seconds				
3. Develop Apply developer MF 319 Time: 60 sec Spin & Rinse with DI				
4. Etching Cr/Au				
5. Rinse in Cold DI				
6. Glass wet etching in 8:1 HF Time: 275 min for 5μm				
7. Rinse in Cold DI for 5min				
8. Remove Cr/Au				
9. Rinse in Cold DI for 5min				
4. Spin dry				

Table C.9 Electrode Patterning (N-P)

	Date	Wafers	Operator	Comments
Starting materials 4" pyrex glass (7740) wafer Used wafer (K-M) Thickness: 500μm				
1. P-clean 5:1 H_2SO_4:H_2O_2 110°C, 10 min				
2. Rinse HOT DI 10 min				
3. Rinse COLD DI 5 min				
4. Spin dry				
2. Al sputtering Target: 2000 Å				
6. Apply Photoresist Shipley 3813 1500rpm, 60sec				
7. Soft bake: 110°C for 80sec Cool on cold plate for 30 sec 18°C				
8. Align and expose Mask: window Time: 19 seconds				
9. Develop Apply developer MF 319 Time: 2 min Spin & Rinse with DI				
10. Hard bake 115°C for 60 sec Cool on cold plate for 60 sec 18°C				
11. Inspect				
12. Strip PR M-pyrol, 95°C 10 min PRIMARY 10 min SECONDARY				
13. Rinse COLD DI 10 min				
14. Blow dry				
15. Al wet etching Temp:43°C				
16. Rinse COLD DI 10 min				
17. Inspect				

Table C.10 Ultra Thin Silicon Wafer Anodic Bonding (Q)

	Date	Wafers	Operator	Comments
Starting materials • 4" fusion bonded Si wafer Thickness: 450μm • 4" pyrex glass wafer Thickness: 500μm				
1. Rinse COLD DI 5 min				
2. Spin dry				
1. Alignment and matching				
2. Anodic Bonding Temp: 400°C Voltage: 1kV				**** Comparison between glass to oxide bonding and Al to oxide bonding for hermetic sealing** **** Keeping an eye on Al to Al good bonding**
3. Inspect				

Table C.11 Deposition of SiO_2 for Good Hermetic Sealing (R)

	Date	Wafers	Operator	Comments
Starting materials: 4" p-type (100) Si wafer				Special caution
1. Rinse COLD DI 5 min				
2. Blow dry				
3. Furnace pre-clean 100:1 H_2O:HF 1 min				
4. Rinse COLD DI 5 min				
5. PECVD O_2: 7.5 SLM Temp: 1050°C Time: 5 hour Target: 5000Å				**** Hermetic sealing**
6. Measure oxide thickness				
7. Inspect				

APPENDIX D

CONTACT INFORMATION

These companies and their products were useful in the microfabrication process which made the device.

High resolution printing service
Photographic Stores and Services
54 East Gregory Drive, Champaign, IL 61820
Phone: 217-333-4677
Fax: 217-333-7832
Email: jngallag@uiuc.edu

SOI wafer
AccuCorp Technical Services, Inc.
67 Trevarno Road, Livermore, CA94551
Phone: 925-371-5669
Fax: 925-371-7081
Email: khussinger@aol.com

Chemicals
Transene Company, Inc.
Danvers Industrial Park
10 Electronics Ave. Danvers, MA 01923
Phone: 978-777-7860
Fax: 978-739-5640

Chrome Photomask Blanks/Standard
Telic
1631 Colorado Ave. Santa Monica, CA 90404
Phone: 310-829-4551
Fax: 310-829-5831
Email: telic2000@aol.com

Thin silicon wafers
Sensor Prep Services, Inc.
704 E. North street, Elburn, IL 60119
Phone:630-365-9645
Fax:630-365-9643

Boron ion implantation
Core Systems
1050 Kifer Road, Sunnyvale, CA 94086
Phone: 408-328-1340
Fax: 408-328-1346

Glass machining
Bullen Ultrasonics, Inc.
950 S. Franklin, Eaton, OH 45320
Phone: 937-456-7521
Fax:937-456-2779
jmoreland@bullen-ultrasonics.com

Metal Deposition
Integrated Sensing Systems(ISSYS)
391 Airport Industrial Drive, Ypsilanti, MI 48198
Phone: 734-547-9896
Fax:734-547-9964
Email: sonbol@mems-issys.com

Glass wafers
Corning – Specialty Light & Materials
Houghton Park C-8
Corning, NY 14831
Phone: 607-974-9000
Fax:607-947-7618

Silicon wafers
Virginia Semiconductor, Inc.
1501 Powhatan Street, Fredericksburg, VA 22401
Phone: 540-373-2900
Fax: 540-371-0371

REFERENCES

1. Ahn, Yongchul, Guckel, Henry, and Zook, J. David (2001). Capacitive microbeam resonator design. Journal of Micromech. Microeng. 11, 70-80.

2. Bartek, M., Forester, J.A., and Woffenbuttel, R.F. (1997). Vacuum sealing of microcavities using metal evaporation. Sensors and Actuators A 61, 364-368.

3. Berthold, A., Jakoby, B., and Vellekoop, M.J. (1998). Wafer-to-wafer fusion bonding of oxidized silicon to silicon at low temperatures. Sensors and Actuators A 68, 410-413.

4. Bienstman, Jan, Tilmans, Harrie A.C., Steyaert, Michiel, and Puers Robert (1995). An oscillator circuit for electrostatically driven silicon-based one-port resonators. Transducers '95, 146-149.

5. Blasquez, Gabriel, Favaro, Patrick (2002). Silicon glass anodic bonding under partial vacuum conditions: problems and solutions. Sensors and Actuators A 101, 156-159.

6. Bouwstra, Siebe, Legtenberg, Rob, Tilmans, Harrie A.C., and Elwenspoek Miko (1990). Resonating microbridge mass flow sensor. Sensors and Actuators A21-A23, 332-335.

7. Burns, D.W., Zook, J.D., Horning, R.D., Herb, W.R., and Guckel H. (1995). Sealed-cavity resonant microbeam pressure sensor. Sensors and Actuators A 48, 179-186.

8. Cartmell, Matthew (1990). Introduction to linear, parametric and nonlinear vibrations. Chapman and Hall.

9. Cheng, Jin, Zhe, Jiang, Wu, and Xingtao (2004). Analytical and finite element model pull-in study of rigid and deformable electrostatic microactuators. Journal of Micromechanics and Microengineering 14, 57-68.

10. Cheng, Y.T., Hsu, Wan-Tai, Najafi, Khalil, Nguyen, Clark T.-C., and Lin, Liwei (2002). Vacuum packaging technology using localized aluminum/silicon-to-glass bonding. Journal of MEMS vol. 11 no. 5, 556-565.

11. Cheng, Y.T., Lin, Liwei, and Najafi, Khalil (2000). Localized silicon fusion and eutectic bonding for MEMS fabrication and packaging. Journal of MEMS vol. 9 no. 1, 3-8.

12. Cheng, Y.T., Lin, Liwei, and Najafi, Khalil (2001). A hermetic glass-silicon package formed using localized aluminum/silicon-glass bonding. Journal of MEMS vol. 10 no. 3, 392-399.

13. Corman, Thierry, Enoksson, Peter, and Stemme, Goran (1998). Low-pressure-encapsulated resonant structures with integrated electrodes for electrostatic excitation and capacitive detection. Sensors and Actuators A 66, 160-166.

14. Corman, Thierry, Enoksson, Peter, and Stemme, Goran (1997). Gas damping of electrostatically excited resonators. Sensors and Actuators A 61, 249-255.

15. Corman, Thierry, Enoksson, Peter, and Stemme, Goran (1997). Low pressure encapsulated resonant structures excited electrostatically. Transducers '97, 101-104.

16. Doeblin, Ernest O. (1994). Measurement systems: application and design. McGraw-Hill, NY.

17. Enoksson, Peter (1997). Novel resonant micromachined silicon devices for fluid applications. Ph.D Dissertation, Royal institute of Technology, Stockholm, Sweden.

18. Enoksson, Peter, Stemme, Goran, and Stemme, Erik (1995). Fluid density sensor based on resonance vibration. Sensors and actuators A 46-47, 327-331.

19. Enoksson, Peter, Stemme, Goran, and Stemme, Erik (1997). A silicon resonant sensor structure for Coriolis mass-flow measurements. Journal of MEMS vol.6 no.2, 119-125.

20. Henry, Manus (2000). Self-validating digital Coriolis mass flow meter. Computing & control engineering journal, 219-227.

21. Housner, George W., Hudson, Donald E. (1959). Applied mechanics: dynamics (2nd ed.). D Van Nostrand Reinhold Company, Inc.

22. Hsu, Tai-Ran (2002). MEMS & Microsystems: design and manufacture. McGraw-Hill, Boston.

23. Kern, W., Puotinen, D. (1970). Cleaning solutions based on hydrogen peroxide for use in silicon semiconductor technology. RCA Review Vol. 31, 187-206.

24. Kovacs, Gregory T.A. (1998). Micromachined transducers - source book. McGraw-Hill.

25. Lee, Byeungleul, Seok, Seonho, and Chun, Kukjin (2003). A study on wafer level vacuum packaging for MEMS devices. Journal of Micromech. Microeng. 13, 663-669.

26. Lee, Duck-Jung, Ju, Byeong-Kwon, Jang, Jin, Lee, Kwang-Bae, and Oh, Myung-Hwan (1999). Effects of a hydrophilic surface in anodic bonding. Journal of Micromech.Microeng. 9, 313-318.

27. Li, Xinghua, Abe, Takashi, Liu, Yongxun, and Esashi, Masayoshi (2002). Fabrication of high-density electrical feed-throughs by deep-reactive-ion etching of pyrex glass. Journal of MEMS vol.11 no.6, 625-630.

28. Niklaus, Frank, Enoksson, Peter, Kalvesten, Edvard, and Stemme, Goran (2001). Low-temperature full wafer adhesive bonding. Journal of Micromech. Microeng. 11, 100-107.

29. Pan, C-T., Yang H., Shen, S-C., Shen, M-C., Chou, M-C., and Chou, H-P. (2002). A low-temperature wafer bonding technique using patternable materials. Journal of Micromech. Microeng. 12, 611-615.

30. Puers, Robert, Lapadatu, Daniel (1996). Electrostatic forces and their effects on capacitive mechanical sensors. Sensors and Actuators A 56, 203-210.

31. Seshia, Ashwin Arunkumar (2002). Integrated micromechanical resonant sensors for inertial measurement systems. Dissertation, University of California, Berkeley.

32. Sparks, D., Smith, R., Schneider, R., Cripe, J., Massoud-Ansari, S., Chimbayo, A., and Najafi N. (2003). A variable temperature, resonant density sensor made using an improved chip-level vacuum package. Sensors and Actuators A 107, 119-124.

33. Sparks, D., Smith, R., Schneider, R., Cripe, J., A., and Najafi N. (2003). A portable MEMS Coriolis mass flow sensor. IEEE sensors conference 2003 No. 8.4, 90-93.

34. Stark, Brian H., Najafi, Khalil(2004). A low-temperature thin-film electroplated metal vacuum package. Journal of MEMS vol. 13 no. 2, 147-157.

35. Senturia, Stephen D. (2000). Microsystem Design. Kluwer academic publishers.

36. Tadigadapa, Srinivas A., and Najafi, Nader (2003). Developments in microelectromechanical system (MEMS): a manufacturing perspective. Journal of Manufacturing Science and Engineering vol. 125, 816-823.

37. Timoshenko, S., Young, D. H., and Weaver, W. Jr. (1974). Vibration problems in engineering. New York:Wiley.

38. Tong, Q.-Y., Gan, Q., Hudson, G., Fountain, G., and Enquist, P. (2003). Low-temperature hydrophobic silicon wafer bonding. Applied physics letters vol. 83 no. 23, 4767-4769.

39. Turner, K.T., Spearing, S.M. (2002). Modeling of direct wafer bonding: effect of wafer bow and etch patterns. Journal of Applied Physics vol. 92 no. 12, 7658-7666.

40. Veijola, Timo, Corman, Thierry, Enoksson, Peter, and Stemme, Goran (1999). Dynamic simulation model for a vibrating fluid density sensor. Sensors and Actuators 76, 213-224.

41. Wei, J., Wang, Z.P., Xie H., and Lan Ng Fern (2002). Role of bonding temperature and voltage in silicon-to-glass anodic bonding. Electronics Packaging Technology Conference 2002, 85-90.

42. Williams, Kirt R., Muller, Richard S. (1996). Etch rates for micromachining processing. Journal of MEMS vol. 5 no. 4, 256-268.

43. Wolf, S., Tauber, R.N. (2000). Silicon processing for the VLSI Era Vol. 1 – Process Technology (2nd Ed.). Lattice press.

44. Wu, Xingtao (2001). Electrostatic micro actuators for mirror and other applications. Ph.D Dissertation, New Jersey Institute of Technology, Newark, NJ.

45. Zook, J.D., Burns, D.W. (1992). Characteristic of polysilicon resonant microbeams. Sensors and Actuators A 35, 51-59.